Physics-Based Modeling for Control and Autonomous Operation of Unmanned Aerial Vehicles

by

Behdad Davoudi

A dissertation submitted in partial fulfillment
of the requirements for the degree of
Doctor of Philosophy
(Aerospace Engineering)
in the University of Michigan
2021

Doctoral Committee:

Professor Karthik Duraisamy, Chair
Professor Ella Atkins
Professor Carlos Cesnik
Professor Kevin Maki

Behdad Davoudi

davoudi@umich.edu

ORCID iD: 0000-0002-9211-0148

This dissertation is in honor of my grandfather Ebrahim Rahmani, the bravest and kindest man I have ever encountered. He taught me to never comprise on what is right and to think independently. He passed away the day I received my admission to the Master's program at the University of Michigan in 2015. I promised him that someday I will dedicate my PhD to him. Here is to his dear living memory.

Acknowledgments

I would like to strongly thank my PhD advisor, Professor Karthik Duraisamy who has unlocked many doors to leading-edge research opportunities and made sure they are well-aligned with my current research interests and future research directions. His clear and clever advice, wisdom and superb insight led me to explore different ideas and pursue them in an open environment while he was making sure progress is being made. It was indeed an honor and a pleasure to work under his supervision at the Computational Aeroscience Laboratory for about five years. I am also very pleased and grateful about the true friendship we formed during this time. His positive influence on my career and personal life is undoubtedly accumulative and will continue for years to come.

I am very grateful to my Doctoral Committee members; Professors Atkins, Cesnik and Maki all whom I was honored to have amazing first-hand experiences and learn valuable lessons during my PhD studies. My Committee members' comments and insights during my pre-defense period are strongly appreciated that helped me to have a clearer framework in the final portion of PhD studies.

Special thanks goes to Professors Peter Gaskell and Ella Atkins of the Robotics Program for their support and providing necessary experimental resources and logistics. My engagement in robotics was fist made possible through a exceptional course Professors Atkins and Gaskell offered in Winter 2019 where I pick up my deep interest to work more with the drones.

My research work was a multi-disciplinary effort, and without help of my PhD student friends in Robotics and Aerospace Engineering would not have been possible. My thanks to Maximilian Krogius who helped me so much in the embedded software programming, and he was always there when I had a question or an idea to discuss.

I appreciate Jiayang Xu, Matthew Romano, Prince Kuevor, Prashin Sharma and especially Akshay Mathur who generously assisted me in motion capture setup and flight testing and spent hours to make sure I have what I need to perform my flight tests – my dissertation would not have been possible without their help. I am also grateful to Professor Ehsan Taheri of Auburn University for his collaboration and advice.

Next and most importantly, I must thank my family, especially my parents who have advocated and invested in my academic path since elementary school, and have made big sacrifices so that I could pursue my academic aspirations in one of the top graduate programs in the world. Their dedication and selflessness have been indeed extraordinary, and I am very blessed and grateful to have had their unconditional love and unending support and contribution.

Finally, I was honored to be selected as the Francois-Xavier Bagnoud Fellow and received the generous FXB fellowship for which I am very grateful to my department. My special thanks goes to our incredible Aerospace Engineering Department, specially our dedicated staff, faculty, graduate students and friends. Over the course of my PhD studies, I have received financial support from the Center for Unmanned Aircraft Systems (NSF Award No.1738714) and NASA under the project "Generalized Trajectory Modeling and Prediction" for Unmanned Aircraft Systems (NNX16AH81A) that I am very grateful to be trusted and suppurated by them.

Preface

My research work stemmed from my passion for innovative, intuitive approaches to tackle complicated physical phenomena. That is, to a high degree of accuracy, complicated problems can be modelled using fundamental approaches. Ludwig Prandtl (1875-1953), the father of novel aerodynamics, is the best example of an innovative thinker who developed such models that later became the mainstay of the design of large sophisticated airplanes. Currently, we have abundant access to computational and experimental resources. These resources can be used to develop efficient and accurate physics-inspired models for design, control and navigation of Autonomous Unmanned Aircraft Systems (UAS).

TABLE OF CONTENTS

LIST OF FIGURES

LIST OF TABLES

LIST OF APPENDICES

LIST OF ABBREVIATIONS

BEM Blade Element Momentum

CFD Computational Fluid Dynamics

DCM Directional Cosine Matrix

ESC Electronic Speed Controllers

HBEM Hybrid Blade Element Momentum

LES Large-eddy Simulation

LFM Low-Fidelity Model

RFL Robotics Fly Lab

RIPF Rotor In-Plane Force

UAS Unmanned Aircraft Systems

UAV Unmanned Aerial Vehicle

VTOL Vertical Take-off and Landing

VWI Vortex-Wing Interaction

ABSTRACT

Unmanned Aircraft Systems (UAS) are widely employed in commercial and military applications, and their utilization is growing at a rapid pace. Effective predictive models for aeromechanics, body dynamics and control are critical in trajectory planning and optimization, autonomous operations, and decision-making. Aeromechanical and wind models that are currently used in the control and guidance of UAS are typically simplistic and often do not represent the essential physics to an adequate degree. Therefore, the performance and versatility of such vehicles may be limited in extreme flight conditions. At the other end of the spectrum, there exist high fidelity models that are computationally expensive, and thus not applicable in path planning, optimization, and onboard flight controllers.

The major goal of this dissertation is to bridge the gap between physics-based models and onboard decision-making. Multi-disciplinary models of appropriate fidelity are developed and integrated into a comprehensive flight simulation software suite. These models are experimentally validated and utilized in trajectory planning, optimization, onboard control and autonomous flight. Studying the impact of models of different fidelity for the environment and the aerodynamics determines the impact of modeling uncertainty on system-level goals.

A vortex-based model for lifting surfaces is developed, using which control surfaces and couplings therein can be efficiently represented. Using this model, the interaction of the propeller wake with a downstream wing is studied, and it is demonstrated these models are effective tools in predicting the propeller-induced

span-wise loading. Such a model is beneficial for trajectory planning and optimization applications to improve flight stability and trajectory tracking.

Next, a novel Hybrid Blade Element Momentum (HBEM) model is developed to predict rotor forces over a wide range of flight conditions. The HBEM model is self-contained and combines blade element theory, momentum theory and a linear inflow model to determine the *unique* inflow that is *consistent with all theories*. The model utilizes the blade geometry and the flight condition as inputs to determine the relationship between the forces/moments and the rotor RPM. A detailed set of wind tunnel experiments is conducted to validate the model across a very wide range of flight regimes. Further, a semi-empirical model for the Rotor In-Plane Force (RIPF) is developed using experimental data. It is noted that these models can be executed in real-time which makes them useful for implementation in flight software.

A custom quadrotor is built and equipped with an ultrasonic wind sensor and RPM sensors. The HBEM and RIPF models are embedded in quadrotor flight software, and it is illustrated these models are fully integrable, and efficient-enough to run on a typical onboard compute module. To evaluate the ability of these models to function in harsh environmental conditions, motion-capture-aided autonomous flight is realized in the presence of strong wind gusts generated by a large industrial fan. A feedforward controller is designed to incorporate physical insight into flight mechanics and to provide estimates of the state. Flight tests are conducted in and out of strong crosswind conditions to further show the impact of computationally efficient models that are capable of being executed onboard in real-time. It is shown that the wind sensing and physics-based models along with the feedforward controller improve trajectory tracking in extreme environmental conditions.

CHAPTER 1

Introduction

New requirements in performance and mission profiles are driving the aerospace community towards novel designs of unmanned aircraft systems (UAS). As an example, Distributed Propulsion has recently been identified as a 'disruptive technology' by NASA, and one that can positively impact evolutionary aircraft designs. Distributed Propulsion can enable new aircraft designs with performance advantages, scaling and efficient Vertical Take-off and Landing (VTOL) characteristics. Recently, significant advances have been made in this regard by NASA in the form of LEAPTech [2] and GL-10 [3] (see Fig.1.1).

Figure 1.1: NASA's GL-10.

Additionally, with recent advancements in Artificial Intelligence (AI) and the advent of light-weight and high-endurance batteries, research in the operation of autonomous UAVs is advancing at a rapid pace. Autonomous aerial systems - conditional on rigorous ver-

ification - can be an efficient, reliable and safe alternate for package delivery (Fig.1.2), ground transportation, military operations and surveillance systems. Over the past decade, Unmanned aerial vehicles UAVs) [4] have been increasingly utilized in a variety of tasks including border patrolling [5], damage inspection [6], mapping [7], precision agriculture [8], etc. With the unprecedented growth in the number of flight vehicles, simulation tools are required for vehicle performance improvement [9, 10, 11], implications of atmospheric winds [12, 13], aerodynamic force modeling [14], rotor failure studies [15], real-time flight simulation [16] and trajectory prediction and validation, especially in the context of certification by analysis [17].

Figure 1.2: Amazon Prime drone.

Drone swarm technology is also trending. As of 2019, drone swarms are part of a 12.1 billion dollar market according to TBRC Report. In addition to military applications, there is growing interest in industry seeking to obtain Federal Aviation Administration (FAA) approval to operate their drones at a commercial scale.

1.1 A Sample Application

A representative trajectory for an autonomous Unmanned Aerial Vehicle (UAV) (i.e., a quadrotor) is shown in Figure 1.3 where the vehicle is assigned, for instance, a package delivery task. It is dispatched from point 'A' (say a service center) to point 'B' (that may represent a delivery designated area) on a nominal trajectory. In this scenario, the presence of obstacles (e.g., buildings, trees, etc) were not shown. The quadrotor is subject to extraneous factors such as wind/gusts that affect its performance and trajectory and may deviate its path from the planned one. In practice, there are various along-the-path constraints that have to be taken into consideration during path-planning, specifically, for very low-altitude flight since the quadrotor has to adopt certain maneuvers to avoid colliding with obstacles.

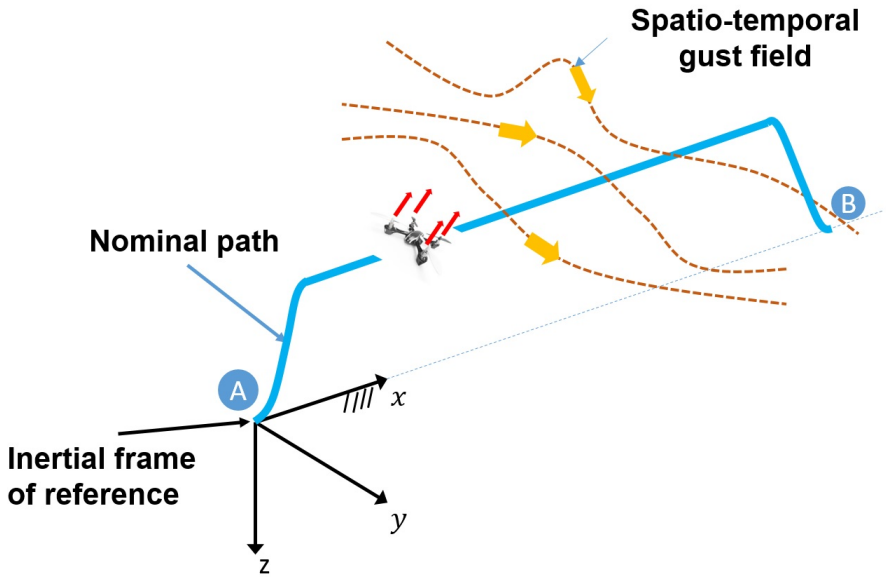

Figure 1.3: A representative trajectory for a quadrotor and the operating environment.

Performance and reliability of an autonomous UAV is reliant on predictive models for aerodynamics, aeroacoustics, environment, body dynamics and control. Such models are essential in executing optimization applications and trajectory planning. Aerodynamic and wind models that are traditionally used by the control and guidance communities are often too simplified to represent essential mechanics, especially when nominal conditions

are not met. In contrast, there are high fidelity models that are sophisticated and accurate, but computationally expensive, and thus not applicable in the path planning, optimization settings and onboard flight software given the limited computational capability and power available. Similarly, in a flight simulation setting where multiple models need to be executed a few hundred times per second, computational efficiency is a limiting factor. Hence, with the lack of efficient, robust physical models of appropriate fidelity, UAVs have merely relied on complex control strategies and camera systems to increase their performance and functionality.

The rest of this chapter is structured as follows: First, challenges in interactional aerodynamics are reviewed. The state-of-the-art vortex and propeller-wing interaction is discussed that is crucial in VTOL applications. Given the importance and impact of the flight simulations in design, optimization and certifying UAS, realistic flight simulations and their necessary physical models are reviewed. The main goal of dissertation is to bridge the gap between physics-based models and onboard decision-making. Physics-based rotor aerodynamic models that are suited to be used in onboard flight software are discussed. Finally, the contributions of this dissertation are demonstrated, and the outline is provided.

1.2 Interactional Aerodynamics

VTOL aircraft typically involve complicated interactions of lifting surfaces with the shed and trailing vortices generated by rotors and/or propellers. Versatility and improved performance of VTOL concepts comes at the expense of increased complexity. For example, the GL-10 flight path [3] involves both hover and cruise operations and the aircraft experiences a complex flight transition phase between hover and cruise flight modes. This requires an efficient optimization strategy for flight trajectory control in conjunction with optimized aerodynamic design for the complex airframe-propulsion interactions. From the viewpoint of simulation-based design of these systems, it is critical to accurately model the evolu-

tion of the rotor wake and its interaction with lifting surfaces. Accurate resolution of the near-wake affects the accuracy of the prediction of the blade airloads, vibratory loads and aeroacoustic signatures.

As another example, consider the complex aerodynamics of the XV-24A LightningStrike VTOL aircraft due to the integration of the propellers into its lifting surfaces. Ref. [18] assessed the relationships between flight conditions and vehicle configurations using Computational Fluid Dynamics (CFD) simulations and reduced database dimensionality by identifying the most influential parameters.

1.2.1 Vortex and Propeller-Wing Interactions

Additionally, the interaction of the trailing vortex system with a lifting surface affects the blade loading and can impact blade stall and loading noise. State-of-the-art RANS-based CFD solvers - with a careful consideration of numerical resolution are capable of accurately modeling the interactional flowfield. However, the high computational costs rule out the use of highly resolved CFD computations at the design stage. In this context, lower-fidelity (for instance, vortex panel) methods present an effective and efficient alternative class of methods to CFD in capturing essential features of the interaction. Another area of need for Low-Fidelity Model (LFM) is in trajectory and mission planning, an exercise in which the aerodynamic model may be executed many times per second.

In many situations, (hovering rotors and propellers, distributed propulsion systems, etc.) vortical interactions with lifting surfaces is dominantly perpendicular in nature. This interaction can have a significant consequence on the blade loading, and on overall performance. A natural choice to mimic this behavior is to use a simplified fixed-wing model which would provide deeper understanding of its flow physics. In literature, only a limited number of experimental efforts exist [19, 20, 21] that study wing-vortex interaction. Komerath et al. [22] in their review paper have emphasized on further fundamental experimental studies to understand rotor wake. Recently, experimental studies by Bhagwat et al. [23] and Ra-

masamy et al. [24] have attempted to understand the fundamental nature of the interaction. Detailed measurements have been performed to study the loading and wake structure of a wing-vortex interaction using a combination of extensive surface pressure, balance loads, and 3-component PIV measurements. These experiments would provide data of adequate quality to improve existing vortex models besides enabling validations of computational simulations. Their recently conducted first phase of measurements provides sufficient data on spanwise loads and wake behavior for a range of wing-vortex interaction conditions.

1.3 Realistic Flight Simulations

As indicated earlier, aeromechanical models are critical in design and optimization. If they are computationally efficient, they can also be used in a flight simulation setting to predict the state of the vehicle and improve performance and versatility. To perform flight simulation in realistic environmental conditions, a set of tools of appropriate fidelity should be integrated. Therefore, a comprehensive approach towards validating and planning trajectories of flying vehicles requires, in general, a framework that takes into account various aspects including 1) appropriate-fidelity aeromechanical and dynamic models of the vehicle to present a realistic view of the actual motion, 2) accurate modeling of the environment, which may include modeling of external factors that alter the trajectory of the vehicle including wind and gust models, 3) development of a flight controller to control vehicle trajectory to within a prescribed accuracy, 4) a guidance (motion-planning) algorithm that provides a nominal "optimal" trajectory, and 5) a navigation model to represent the sensory data and the measurement noise, which will be used to update the location/orientation of the flying vehicle to be used for guidance and by the flight controller.

Depending on the stage and/or nature of the study, various simplifications are invoked to facilitate the task of trajectory prediction and performance analysis [25]. For instance, it is common to consider a three-degree-of-freedom model to only trace the trajectory of

the center of mass of the vehicle while the orientation of the vehicle is considered to be of secondary importance for early analysis [26]. Additional degrees of freedom are usually considered for higher-fidelity models and at later stages of design of systems to gain better understanding of the motion and to obtain realistic flight performance envelopes [27, 28].

1.3.1 Atmospheric Modeling

Simplified atmospheric models are typically used for mission planning and certification of UAVs. In practice, the operating environment of UAVs flying at low altitudes (< 500 m) is not only subject to strong mean velocity gradients (shear), but also involves intermittent unsteady wind gusts that contain a non-trivial fraction of energy compared to the mean flow. Further, the characteristic size of the turbulent eddies, even in a stable boundary layer, is of the order of a few meters [29], which is similar to the size of a UAV. Accounting for such scales becomes critical to the vehicle aeromechanics and thus to more accurate trajectory prediction and validation tasks.

A widely used tool for numerical weather prediction is the Weather Research and Forecasting (WRF) model [30, 31]. WRF is, however, a *mesoscale model* and is typically used over large spatial domains ($O(1000)$ km) and with coarse resolutions ($O(2)$ km). WRF thus cannot be relied upon to represent all eddies and gusts of interest for UAV trajectory prediction and validation purposes, and thus a different, higher resolution approach is required.

1.3.2 Rotary-Wing Aeromechanical Models

A critical element in performance and/or trajectory analysis of flight vehicles is to use accurate dynamical models for the propulsion system. For a VTOL, modelling the lifting surfaces and propellers is crucial. A comprehensive analysis should be performed to characterize aerodynamic interaction for different flight phases. Accurate aeroelasticity [32] and aeroacoustics [33] analyses are also required. For a quad- or multi-copter not only the

individual performance of the propellers, but their mutual interactions become important, and have to be taken into consideration for certain types of maneuvers [34]. In particular, the key requirement for the aeromechanics model is to provide an effective characterization of the response of a UAV to unsteady gust loads [35]. An additional requirement is that the fidelity of the model should be such that it is easily integrable into the trajectory validation and planning modules and the necessary computations can be performed in near-real time.

It is common practice to approximate the actual performance of a propeller (i.e., the thrust or torque) using idealized, simple algebraic models to facilitate numerical analyses [36, 37]. The so-called static models (namely, the thrust and torque of a rotor are expressed in terms of the square of rotor speed) are used extensively for hovering, and slow maneuvers. However, these models do not capture the realistic performance of a propeller, which in general, depends on the inflow velocity. In particular, more accurate models have to be used for flight trajectories that can be utilized in demanding situations such as high speed forward and descent flight phases [38]. In low-altitude flight, these aerodynamic phenomena can influence the vehicle dynamics in the presence of wind and gusts. Towards this end, a propeller thrust model in forward flight was presented in [39] for a blade with linear twist.

On the other hand, the use of higher-fidelity models such as those based on computational fluid dynamics [34, 40] or even vortex-based methods [41] to predict the aeromechanics of flight vehicles is computationally demanding, and thus is not feasible in trajectory optimization or trajectory prediction settings. As a consequence, an additional challenge is to establish a set of computationally efficient and effective models of the aeromechanics and flight dynamics of UAVs. The following section reviews rotor aerodynamic models in more detail.

1.4 Rotor Aerodynamic Models

The flight simulation framework that was earlier introduced in this dissertation, is capable of incorporating different aeromechanical models as a *black box*. Thus, every component of the flight simulation package can be improved independently. A critical element in the flight simulation package is an accurate and efficient predictive model for the rotor forces and moments. Furthermore, in order to be useful in applications such as trajectory planning and autonomous operation, such aerodynamic models must be efficient and executed in near-real-time, and also should be integrable within control and planning modules. In the next few paragraphs, a review on the available aerodynamic rotor models is made, and a novel model will be developed in Chapter 4.

Wind disturbances are a prominent factor in the control of UAVs [42]. The incoming wind can significantly alter the propulsive forces and moments generated by a UAV. Wind-sensitive models are necessary to capture the vehicle response to gusts. High fidelity models such as those based on detailed Computational Fluid Dynamics [43, 44, 45, 46, 47] or vortex-based methods [41] is not amenable for use in design, flight simulation or onboard embedded controller software.

1.4.1 Momentum Theory

Classical momentum theory [48] relates thrust coefficient to the average inflow velocity across the rotor disk. In this theory, the blade shape and airfoil characteristics are not considered. In axial flight - outside of the vortex ring state, the solution to momentum theory is unique and explicit. Momentum theory in forward flight leads to a quadratic equation and its solution is found through an iterative process. In high forward speeds, where advance ratio is much larger than inflow ratio, the solution to momentum theory becomes explicit. While this theory is useful for approximate evaluations in early stage analysis, this theory is not useful for detailed analysis because it ignores rotor blade physical characters tics and

non-axisymmetric nature of aerodynamic environment.

1.4.2 Blade Element Momentum (BEM) Theory

In blade element (BE) theory, rotor blades are decomposed to a finite number of thin airfoils and BE obtains airfoil sectional lift individually and integrate them to obtain the thrust generated by a rotor. Therefore, blade element theory is cognizant of geometric details, but requires the specification of the sectional inflow velocity. In axial flight, momentum and blade element theories can be analytically combined [48] to find an estimate for the inflow velocity at every radial location as a function of the blade aerodynamic and geometric characteristics. This model for the inflow is often referred to as the radial inflow model and has been utilized in UAV simulations (for instance, Ref. [49, 50]). Ref. [51] aimed to model the aerodynamics of a propeller. They used Blade Element Momentum (BEM) with additional corrections and compared their predictions with experimental measurements. However, their investigation was limited to the cases where the propeller shaft was aligned with the free-stream. Blade element momentum (BEM) theory is a versatile tool to analyze the performance of rotating blade applications such as wind and hydrokinetic turbines [52, 53, 54, 55, 56, 57] and rotor and propeller aerodynamics [51, 58]. In ship hydrodynamics, analysis of different propeller BEM-based models and their effect on manoeuvring prediction are discussed in Ref. [59]. Also, by coupling a BEM propeller model with the solution of the RANS equations, manoeuvring coefficients for a ship travelling forward and at a drift angle are obtained in Ref. [60].

1.4.3 Addressing Challenges in Forward Flight

Challenges arise in the representation of the aerodynamics of rotors in forward flight, given the inflow is non-uniform across the rotor disk, and is strongly coupled to the thrust in a complicated manner. While blade element momentum theory [48] and variants can be relied upon for hover and axial climb/descent, reliable analytical models do not exist for

forward flight. Towards this end, this work proposes a new aerodynamic model for the performance of rigid rotors and propellers in forward flight.

In Ref. [61], momentum theory, vortex theory and blade element theory in forward flight are discussed. As mentioned earlier, momentum theory merely relates thrust coefficient to inflow ratio, therefore there are two unknowns and one equation. However, in the helicopter community, the thrust coefficient is often considered known given that thrust is assumed to be equal to the weight of the vehicle in steady flight, and also rotor operates at a fixed RPM. In smaller rotary-wing UAVs, this assumption is generally not applicable as these vehicles are generally over-powered and thrust can be much larger than the weight. Further, the electric motors operate in a wide range of RPM conditions.

Blade element theory in forward flight does not provide a closed-form solution and requires the velocity information for every radial location and azimuth angle to estimate the total generated thrust and moment. Given the flight condition and wind information, the radial and tangential velocities are obtained. However, the velocity perpendicular to the rotor (i.e. inflow ratio) is not known a priori. Different inflow models such as the uniform, linear and Peters-He [62] generalized dynamic wake are employed. The effect of such models on the aeromechanics of a quadrotor in hover and forward flight is studied in Ref. [63]. The inflow velocity distribution across the rotor disk is also experimentally obtained in Ref. [64]. These models are often functions of the uniform inflow velocity that is estimated by the momentum theory. Thus, in simple terms, the BE theory – similar to the momentum theory – offers one equation with two unknowns: thrust and uniform inflow ratio.

Peters and co-workers [65, 62] developed a popular family of dynamic inflow models targeted at state space implementation. More sophisticated models using potential flow models have also been proposed [66, 67], but are computationally expensive and cumbersome to implement in flight simulation settings. **Therefore, an efficient and self-contained solution to obtain the thrust given the rotor blade configuration and flight**

condition in forward flight remains elusive.

In the absence of reliable analytical models, flight simulations have employed data fits or extremely simple models, such as those assuming thrust and torque to be proportional to the square of rotor angular velocity ω [68, 69]. *simplified* model is refereed to this model. While this model can, in fact, be a good predictor for rotors in hover, results indicate that in axial and forward flight, this assumption is very inaccurate.

In addition to high fidelity CFD-based models, intermediate-fidelity vortex particle methods have been used to determine rotor loading in forward flight. For instance, Ref. [70] employed a viscous vortex particle method to determine the evolution of the rotor wake and obtained blade loads using a reduced order model in fast forward flight. Ref. [71] utilized the capability of the viscous vortex particle method (VPM) and modelled multirotor aerodynamic interactions and introduced the VPM-based rotor model. While these vortex particle methods are power tools for conceptual design and optimization, they cannot be executed in real time with the limited computational power and resource available onboard.

Ref. [72] proposes an approach to reduce the reliance on empiricism by determining the inflow velocity by equating the elemental thrusts from blade element theory and BEM theory in forward flight. While this technique is elegant, the inflow velocity is assumed to be only a function of the radius, and not of the azimuth. The impact of this assumption is hard to evaluate, as detailed validations are not presented. In Ref. [1], an inflow model is developed using BEM in forward flight, where the inflow is explicitly solved for at every radial location and azimuth angle. While experimental validations are not presented for the aerodynamic model in forward flight, this work - in a similar spirit to the present HBEM model - combines blade element and momentum theories and is analyzed further in the appendix.

In the present work, extensive experimental data is obtained to validate the proposed models. Forces perpendicular and tangent to the rotor are calculated. Thrust, that is defined

as the perpendicular force to the rotor plane, is physically modeled by HBEM model for different inflow conditions and rotor angle of attack. A data-driven model for the force tangent to rotor plane force is introduced - called RIPF - that can be used in onboard flight software.

An appealing feature of the HBEM model is that it is based on a self-contained and consistent combination of momentum and blade element theories with the assumption of a linear inflow model. These models are integrated with a backstepping control module [73] and a 6 DoF flight simulation routine [74] and used in trajectory planning in uncertain environments in Chapters 3 and 4. To evaluate the capabilities of the above models, a custom quadrotor is built using a platform described in Ref. [75] platform, and the models are deployed onboard. It is noted the developed models require wind data to provide accurate estimations of the forces exerted on the quadrotor. Therefore, a wind sensor is implemented onboard of the quadrotor to measure the wind speed and direction in real-time. A new passive controller strategy is implemented to incorporate and utilize the models and sensors data. Flight tests are conducted to better understand benefits of the proposed models. Autonomous flight testes are conducted in extreme-wind condition as well as a steady, no-wind condition.

1.5 Contributions

The scope of this research work is multi-disciplinary with the goal of connecting physics-inspired models with onboard controllers and decision making algorithms. The key contributions of this dissertation can be condensed and categorized to four sections:

1. Aerodynamic modeling for Fixed and Rotary-wing aerial vehicles
2. Experimental test campaign to validate aerodynamic models
3. Comprehensive flight simulation framework for Rotary-wing UAVs.

4. Flight testing for autonomous navigation using feedforward controller and wind sensing.

The following are specific contributions:

- Constructed vortex-based models for a full propeller-driven aircraft. These models are applied in Propeller-Wing Interaction and Vortex-Wing Interaction (VWI) and validated/verified against experimental tests and high-fidelity simulations.
- Developed the Hybrid Blade Element Momentum (HBEM) model, which consistently combines Blade Element and Momentum theories with a linear inflow model, and can be executed in near-real time. This model is usable in preliminary design as well in flight simulation packages and onboard flight software.
- Conducted a comprehensive set of wind tunnel experiments to measure rotor performance for different rotor angles of attack and wind speeds, and validated the HBEM model.
- Developed a semi-empirical model that estimates the rotor-in-plane force (RIPF).
- Established the relationship between throttle values and corresponding RPM condition in forward flight.
- Constructed a reduced-order representation of the wind field data and illustrated the impact of order reduction on the resultant trajectory as well as using a popular commercial wind model (i.e., the Dryden model).
- Performed flight simulations in more realistic atmospheric conditions by integrating different control, aeromechanical, and environmental models into a comprehensive flight simulation framework which is open sourced.
- Integrated an ultrasonic wind sensor successfully with onboard hardware. Used the wind sensor data for the purpose of improving flight stability and resilience.

- Proposed a new feedforward controller to increase controllability and resilience by estimating a closed-form solution for the state parameters in a quasi-steady fashion by using onboard sensors and HBEM and RIPF models.

- Generated and compiled efficient codes for HBEM and RIPF models that are compatible with the BeagleBone Blue processor (ARM® Cortex-A8 processor) using specific coding algorithms and optimized libraries.

- Showed that a compatible integration of the models, sensors and fast onboard computations is possible and performed autonomous flight tests using an indoor motion capture system.

- Autonomous navigation for the quadrotor was successfully demonstrated in a harsh and unsteady environmental condition created by a strong 3 ft-diameter axial fan.

- Demonstrated that the feedforward controller, that uses physics-inspired models enabled by wind sensing, marginally improves trajectory tracking in harsh environmental conditions.

1.6 Organization of The Dissertation

The rest of the thesis is organized as follows: Interactional aeromechanics, vortex-wing and propeller-wing phenomena are studied in detail using high and low fidelity approaches in Chapter 1. A comprehensive framework for flight simulation of rotary-wing vehicles is presented in Chapter 3. Chapter 4 details the HBEM model formulation and experimental validation along with a data-driven model for Rotor in-plane force. In Chapter 5, experimental quadrotor sensor design and control is discussed, and the developed models are embedded onboard of the quadrotor. Flight tests in and out of extreme wind conditions are conducted, and results are provided in Chapter 6. A summary of the dissertation and conclusions are presented in Chapter 7.

CHAPTER 2

Interactional Aerodynamics

Interactional aerodynamics is a very common phenomenon in fixed and rotary wing UAVs. High-fidelity models can be used to study and characterize the aerodynamic interactions. However, such models may not be efficient to be used even in formal design optimization, and certainly not appropriate to be used in flight simulation modules nor in onboard flight software.

In this chapter, the interaction of trailing vortices with lifting surfaces is investigated using two levels of modeling fidelity. An overset mesh-based Reynolds-Averaged Navier–Stokes solver is considered as the high-fidelity computational model (HFM). A lower-fidelity model (LFM) is developed by combining a vortex panel method with a propeller aerodynamic model and slipstream theory. The high-fidelity model is first validated against available experimental data obtained from the interaction of a trailing vortex generated by an upstream wing with a downstream wing.

The ability of both models to represent the development of the vortex wake and integrated loads is assessed for a number of parametric configurations, including a case in which the vortex core directly impinges on the wing surface. Following this, isolated propeller and wing-mounted propeller configurations are studied.

In all of these cases, the high-fidelity model is effective in predicting the details of the flow and integrated airloads. The low-fidelity model, although less accurate, is shown to accurately predict interactional air loads and performance at orders of magnitude less cost

than the high-fidelity model, justifying its role as a viable tool in design and trajectory-planning applications. The contents of this chapter are heavily drawn from Ref. [76].

2.1 Methodology

2.1.1 High-Fidelity Model: Overset RANS Solver

The CFD solver used in the present work is the overset structured mesh solver OVERTURNS [77, 78, 79, 80] (OVERset Transonic Unsteady Rotor Navier-Stokes). The compressible Reynolds Averaged Navier–Stokes equations are solved with a Spalart-Allmaras model [81] for closure. Time integration is performed using second order backward difference method using Lower-Upper Symmetric Gauss Seidel (LUSGS). Newton sub-iterations are used to remove factorization errors and recover time accuracy for unsteady computations. The inviscid fluxes are calculated using a third order accurate upwind scheme that uses Roe's flux differencing [82], while the viscous fluxes are computed using second order central differencing. The solver uses an overset mesh system for efficient mesh resolution. In this arrangement, the body-fitted blade meshes are embedded inside a Cartesian off-body mesh to capture the entire wing-wake aerodynamics. The solver uses a novel Implicit Hole-Cutting (IHC) technique[83], which has been efficiently used in several computational studies on complex rotary wing flows [84, 85, 79, 80]

2.1.2 Low-Fidelity Model: Vortex Panels and Propeller Performance/Wake

The low-fidelity model uses vortex panels to analyze forces exerted on a lifting surface and models for propeller loads and wake.

2.1.2.1 Lifting Surfaces

The lifting surface is partitioned into vortex panels [86] (of circulation strength Γ_i) in the stream- and spanwise directions and bound vortices are placed at the quarter-chord location of each panel. The wake is considered as an extension of the trailing edge (TE) panel with the same vorticity magnitude and is semi-infinite. To determine the strength of the bound vortices, the influence of the induced velocity from every panel (including the self-induced effects), the wake and any other source of induced velocity at the control points is considered. A linear system is formed by enforcing flow tangency at the control points, and the vorticity Γ (a column vector) on the wing panels is obtained as follows;

$$\Gamma = A^{-1}b \tag{2.1}$$

where A is the aerodynamic influence coefficient matrix and b is a column vector incorporating the velocity perpendicular to the panels [1]. From potential flow theory, the pressure differential for each panel is obtained using:

$$\Delta P_{ij} = \rho\{\vec{v}_{ij} \cdot \tau_i \frac{\Gamma_{i,j} - \Gamma_{i-1,j}}{\Delta c_{ij}} + \vec{v}_{ij} \cdot \tau_j \frac{\Gamma_{i,j} - \Gamma_{i,j-1}}{\Delta b_{ij}}\} \tag{2.2}$$

where, $\vec{v} = [U(t) + u_w, V(t) + v_w, W(t) + w_w]$, and U, V and W are flow velocities in the three Cartesian coordinate, x-, y- and z-directions. The indices i and j are in stream- and spanwise directions respectively. Here, Δc_{ij} and Δb_{ij} are the stream- and spanwise lengths of a panel at i,j locations and u_w, v_w and w_w are the induced velocity by the wake on the panel. Finally, τ_i and τ_j are the tangential vectors to the panel in i and j directions, respectively. It is noted that for the panels at the leading edge, $\Gamma_{i,j}$ is substituted for $\Gamma_{i,j} - \Gamma_{i-1,j}$. Further, for the panels at the tip, $\Gamma_{i,j} - \Gamma_{i,j-1}$ is assumed to be zero. Validations and comparisons of the model with CFD data and experiment are presented in later sections.

[1] $-U \sin\alpha$, where U is the free stream velocity and α is the wing angle of attack.

2.1.2.2 Propeller Aerodynamic Model

To efficiently represent the the propeller blade, an adaptation of extended blade element theory, [48] is pursued. The sectional lift coefficient, C_l, is determined by estimating the 2D lift curve slope, C_{l_α}, (see Appendix A.3 for more information) and the inflow angle as:

$$C_l = C_{l_\alpha}(\Theta + \alpha_{L=0} - \Phi), \tag{2.3}$$

where the inflow angle is obtained as $\Phi(r) = \lambda(r)/r$ and Θ is the blade twist angle, and $\alpha_{L=0}$ is the absolute value of the zero-lift angle of attack, r represents the rotor radius.

The process of determining the inflow coefficient λ requires an iterative method that also takes into account the lift loss at the root and tip of the blade. This involves the solution of the following set of equations:

$$\lambda(r, J) = \sqrt{(\frac{\sigma C_{l_\alpha}}{16F} - \frac{J}{2})^2 + \frac{\sigma C_{l_\alpha}}{8F}\theta r} - (\frac{\sigma C_{l_\alpha}}{16F} - \frac{J}{2}) \tag{2.4}$$

$$F = \frac{4}{\pi^2}\cos^{-1}(\exp(-f_{root}))\cos^{-1}(\exp(-f_{tip})), \tag{2.5}$$

where J is the advance ratio, σ is the blade solidity, $f_{root} = \frac{N_b}{2}\frac{r}{(1-r)\phi}$ and $f_{tip} = \frac{N_b}{2}\frac{(1-r)}{r\phi}$. Function F is referred to as Prandtl's loss function.

To represent the axial and swirl velocity behind the propeller, a slip-stream theory model is adapted from Ref. [87] and Ref. [88]. This model requires the vorticity magnitude on the blade, and it is a common practice to obtain it using experiment or pre-defined empirical functions. However, this work uses the extended blade element theory to calculate the lift and convert it to vorticity using Kutta-Joukowski theorem as follows:

$$\Gamma(r) = \frac{1}{2}cC_l\sqrt{(\Omega r)^2 + U_\infty^2}. \tag{2.6}$$

Given the vorticity, one can estimate axial and swirl velocities of a propeller in a free stream velocity, U_∞, as:

$$V_{swirl}(r) = c_s \frac{N_b \Gamma(r)}{2\pi r} \tag{2.7}$$

$$V_{axial}(x,r) = U_\infty + c_a \frac{N_b n \Gamma(r)}{4\pi U_\infty} \left(1 + \frac{x}{\sqrt{r^2+x^2}}\right), \tag{2.8}$$

where x is the distance from the propeller plane, N_b is the number of blades and n is the propeller rotation rate in revolutions per second. It is noted that, at $x = \infty$, the axial velocity attains twice the value of that at the propeller plane, which is in agreement with the conventional momentum theory. To account for viscous diffusive effects and presence of nacelle, the values c_s and c_a were calibrated with respect to the experimental data to the values $c_s = 0.9$ and $c_a = 0.65$.

2.1.2.3 Propeller Slipstream Model

The propeller slipstream contracts downstream of the propeller plane. Based on the work by Veldhuis [89], the slipstream radius $R_s(x)$ can be found as:

$$\frac{R_s(x)}{R} = \sqrt{\frac{1+a}{1+a\left(1+\frac{x}{\sqrt{r^2+x^2}}\right)}} \tag{2.9}$$

where a is the dimensionless axial velocity factor, given as: $a = \dfrac{c_a N_b n}{4\pi U_\infty^2} \dfrac{1}{R} \displaystyle\int_{0.2}^{R} \Gamma(r) r dr$, which assumes $\Gamma(r) = 0$ for $r = [0, 0.2R]$, i.e. inside the nacelle.

Using the velocity information in the propeller wake, the interaction between the propeller and a fixed wing can be obtained by combining the propeller model and the vortex panel method discussed earlier. A comparison between the predicted interaction effects using the high and low fidelity models will be presented in later sections.

2.2 Vortex-Wing Interaction

2.2.1 Fixed Wing-Vortex Interaction Test Configuration

The chosen configurations correspond to experiments [23] conducted in the 7 by 10-ft wind tunnel at Ames Research Center for a range of tunnel speeds up to about V_∞ = 242 ft/s (q_∞ = 70 psf or $M_\infty = 0.21695$). Measurements were performed on a pressure-instrumented NACA0015 12-inch chord wing. The perpendicular vortex wake was generated by a NACA0015 18-inch chord wing (VG). Both wings are rectangular, straight and untwisted. The maximum chord Reynolds numbers are 1.5×10^6 and 2.2×10^6 for the wing and the VG, respectively. The VG was placed vertically in front of the wing at several locations varying in stream wise, spanwise and vertical positions with respect to the wing. Pressure measurements were obtained for each of these wings with/without VG configurations at several span wise stations on the wing to study the effects of vortex wake on the wing loading.

One of the main goals of the experiment was to measure the wing-vortex wake system and its effect on the wing loading. Therefore, velocity field measurements behind the wing-vortex generator were made using stereoscopic particle image velocimetry (PIV). The velocity field measurements were obtained on a plane normal to the tunnel flow over 3.5 ft $\times$2 ft.

2.2.2 High-Fidelity Model Details

The near-body wing and vortex generator (VG) flow fields are modeled using C–O type body confirming meshes. Wing mesh has $267 \times 185 \times 101$ points (in the chordwise, spanwise and normal directions, respectively) and VG mesh has $267 \times 145 \times 101$ points. The wing surface spacing in the normal direction corresponds to $y^+ \approx 1$ and the mesh outer boundary is at a distance of two chords away from the blade surface. The wing-wake system is built (as shown in Fig. 2.1) by embedding both the blade meshes in a Cartesian

background (wind tunnel) mesh consisting of $240 \times 201 \times 201$ points. .

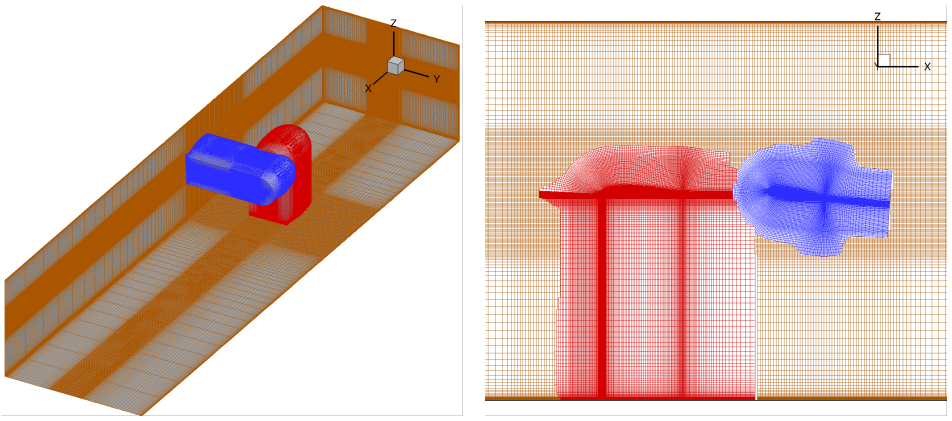

(a) Computational domain (b) Hole cut mesh system

Figure 2.1: Overset mesh system of wing-vortex interaction.

There are a few details in the experiment that require careful adjustments, so that the simulation accurately captures the physics of the problem. The following considerations were made to achieve reasonable comparison with the experimental data.

1. The velocity inlet magnitude was modified to accommodate the blockage effects of the objects in the wind tunnel. The airload computation includes the experimental apparatus blockage factor, $\beta = (1.0 + \epsilon)^2, \epsilon = 3.2\%$ in freestream dynamic pressure, i.e. $q_\infty = q_\infty^{CFD}/\beta$. Specifically, the CFD airload values are corrected with respect to the effective q_∞ instead of q_∞^{CFD}.

2. The side walls in the background mesh were treated as viscous walls.

2.2.3 Low-Fidelity Model Details

In contrast to the high-fidelity model - in which the flow corresponding to the vortex generator is resolved - the low-fidelity model uses an imposed velocity field. A Lamb-Oseen vortex was used to model the VG tip vortex that generates the following velocity field:

$$V_\theta(r, \theta) = \frac{\Gamma_{VG}}{2\pi r}\left(1 - \exp\left[-\frac{r^2}{r_c^2}\right]\right) \tag{2.10}$$

Following Ref. [90], a core radius of 1.5" for VG tip vortex was used. The vorticity magnitude Γ_{VG} is, according to Betz's roll-up theory [91], the maximum vorticity at the root of the VG that can be obtained by running the panel code for the VG alone. Having obtained the velocity field generated by tip vortex of the VG, one can find the induced velocity on the wing, and thus obtain the resultant lift distribution.

2.2.4 Isolated Wing Configuration

An isolated wing is considered first, and airload predictions are compared against the experimental data. The wing angle of attack (α_w) was set to 7 degrees in this case. As observed in Figure 2.2, experimental airloads are well-predicted by CFD. As observed in Fig. 2.2(a), both the inviscid and viscous treatment of the wind tunnel wall yield accurate predictions of the outboard normal force, but the predictions deviate near the wall. This is an artifact of discrepancies between the boundary conditions in the simulations and the treatment of the wind tunnel wall in the experiment. In the experiment, wall slots were used to enable translation of mounted wing along the streamwise direction. In discussing with the experimentalists, further uncertainties are anticipated as the wing force measurements are found to be sensitive to the size of the introduced wall fence to avoid leakage of flow into the wall slot. Figure 2.2(b) shows the effect of varying fence diameters on normal force coefficients. Figure 2.3 further shows the presence of the strong vortex wake for this case, with Figure 2.3(b) detailing the vortex structures in the wake. Appendix A.1 presents further vortex evolution details. This computation serves as a basic validation of the simulation set up.

2.2.5 Wing-Vortex Interaction

This section investigates the vortex wake interaction with the wing and consequently its effect on the wing loading. Several vortex strength values were considered. Further, several relative positions of VG with respect to wing are considered to provide insights onto

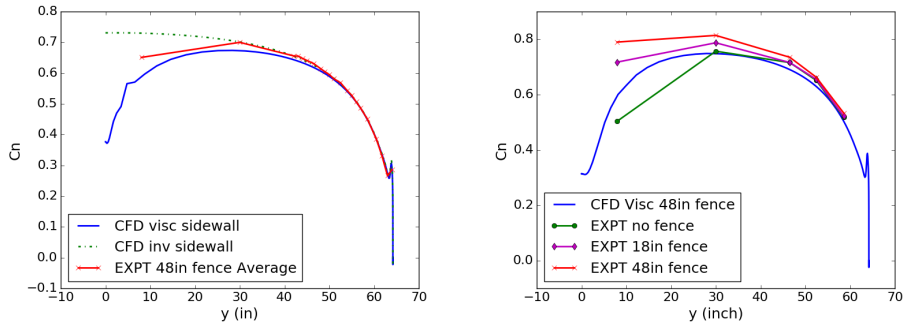

(a) Viscous vs inviscid $\alpha_w = 7°$ (b) Fence effect $\alpha_w = 8°$

Figure 2.2: Wing airloads and wall fence effect.

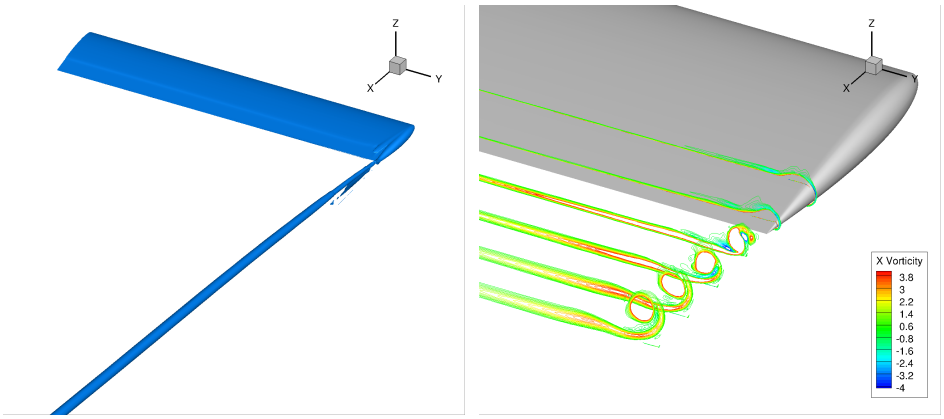

(a) Q-criterion (b) Vorticity contours

Figure 2.3: Solution for wing only case; $\alpha_{\mathbf{w}} = \mathbf{7}°$.

interaction of VG vortex with wing tip vortex and its effect on the wing loading.

Direct Hit Case

For this case, the wing angle of attack was held at 7 degrees, and VG angle of attack (α_{vg}) was set to 4 degrees. The VG tip height was placed such that it aligned with the wing for a direct wing vortex interaction, i.e. $\Delta Z = 0$ inch, Z being the vertical separation distance between VG tip and wing quarter chord. To ensure accurate resolution of the vortex, a vortex tracking grid (VTG) is used as shown in Figure 2.4(a). The VTG introduces 210 thousand cells with $41 \times 41 \times 125$ along spanwise, vertical and streamwise directions, respectively. The VTG mesh resolution ensures that there are approximately 15 mesh points

in the vortex core diameter ($r_c \sim 0.15c$)– see Figure 2.4(b). As noted in the prior work of the authors [77, 92], this mesh resolution can resolve a vortex core with sufficient accuracy.

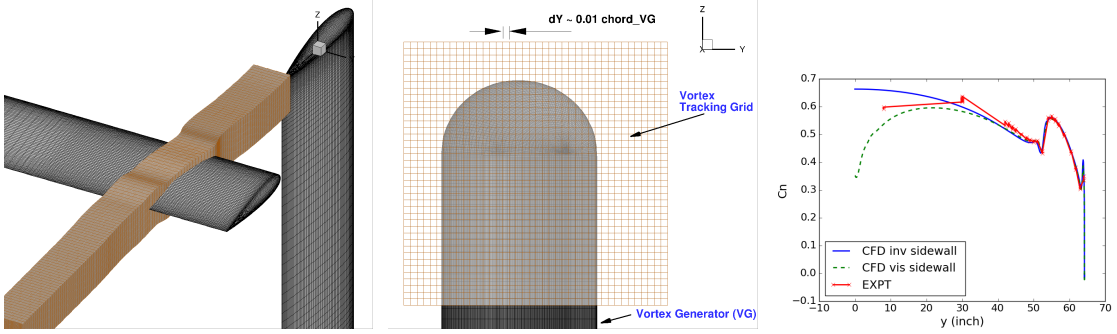

(a) Vortex Tracking Grid (b) Vortex Tracking Grid Resolution (c) Airloads

Figure 2.4: Mesh and airloads with $\mathbf{y_{vg}} = \mathbf{52.5}$in. (4.375c); $\alpha_{\mathbf{w}} = \mathbf{7}^\circ$, $\alpha_{\mathbf{vg}} = \mathbf{4}^\circ$, $\mathbf{\Delta Z} = \mathbf{0}$in.

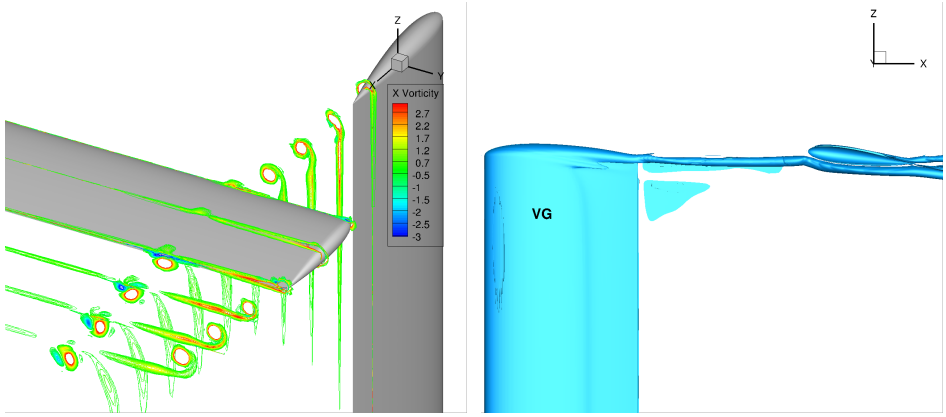

(a) Vorticity contours (b) Q-criterion

Figure 2.5: Solution with $\mathbf{y_{vg}} = \mathbf{52.5}$in. (4.375c); $\alpha_{\mathbf{w}} = \mathbf{7}^\circ$, $\alpha_{\mathbf{vg}} = \mathbf{4}^\circ$, $\mathbf{\Delta Z} = \mathbf{0}$in.

Figure 2.4(c) shows normal loads for the wing with $\alpha_w = 7^\circ$, $\alpha_{vg} = 4^\circ$, VG at $y_{vg} = 52.5$ inch span and $\Delta Z = 0.0$inch. The load on the wing is well-predicted, both in terms of the peak amplitude and shape. Discrepancies in the in-board section are partially attributable to uncertainties in the side wall boundary condition. Vorticity magnitudes in the streamwise direction for multiple planes in the downstream of the VG are plotted in Figure 2.5(a). As noted, the evolution of the VG tip vortex was well captured. Further Figure 2.5(b) show the side view of the vortex wake evolution, respectively. The Q-criterion

shows the deflection of the vortex along the lower surface of the wing during the wake interaction.

Another VG position, at 58.5 inch represents the nominal direct hit interaction. The solutions are shown in Figure 2.6. Figure 2.6(a) verifies that the predicted CFD normal loads compare well with the experimental values. The secondary incremental normal load is positioned slightly inboard from the wing tip. This is a consequence of the spanwise in-board movement of the wing tip vortex wake due to its interaction with the incoming VG vortex wake. In fact, this coupled wake interaction results in a vortex roll up which eventually leads to their merger (Figure 2.6(b)). The vorticity magnitude in the streamwise direction on multiple planes downstream of the VG are plotted in 2.6(c). The roll-up observed in the Figure is qualitatively similar to what is observed in the experiments [23], i. e. the streamwise relative positioning of the trailed vortex wakes follow similar trend to what is observed in the experiment. Further details of the vortex evolution are presented in Appendix A.1.

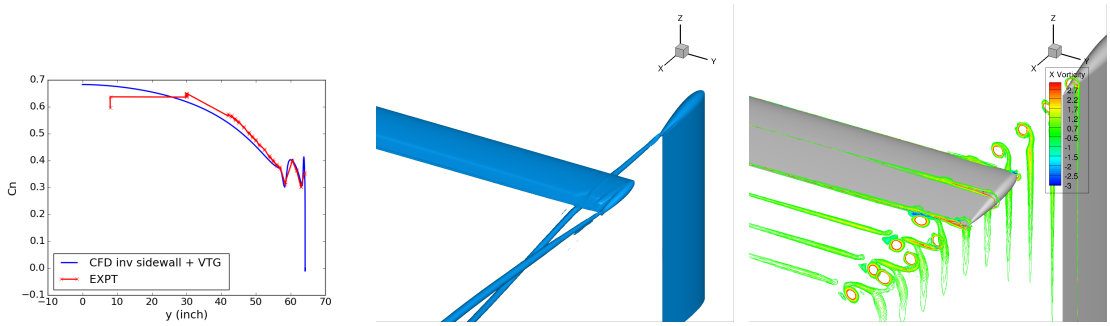

(a) Airloads (b) Q-criterion (c) Vorticity contours

Figure 2.6: Solution with $\mathbf{y_{vg}} = \mathbf{58.5}$in. (4.875c); $\alpha_{\mathbf{w}} = \mathbf{7}^{\circ}$, $\alpha_{\mathbf{vg}} = \mathbf{4}^{\circ}$, $\mathbf{\Delta Z} = \mathbf{0}$in.

Figure 2.7 demonstrates the effect of vortex wake interaction on wing loading. While the incremental values are consistently similar for all the spanwise vortex locations, the values reach larger peaks near the wing tip for the vortex locations that are more outboard. The load peaks near the tip, however, are the largest for the vortex location which is at the most outboard location. Here, the incremental chord normal force coefficient ΔCn

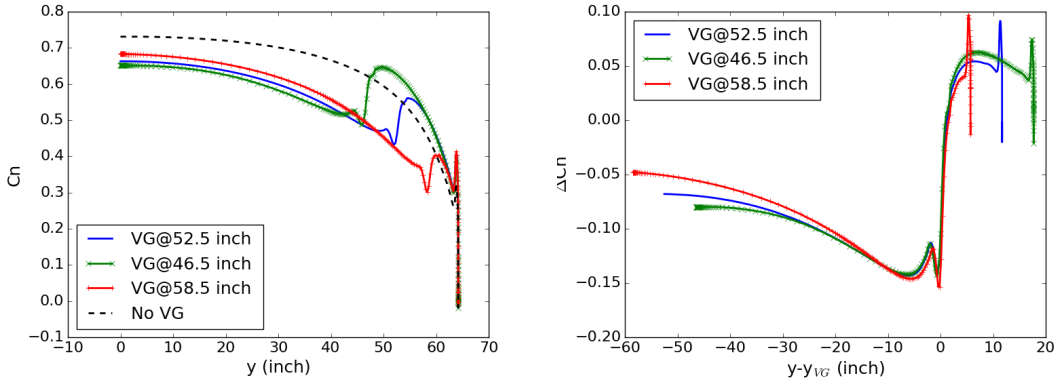

(a) Cn (b) ΔCn

Figure 2.7: Airloads for $\alpha_{\mathbf{w}} = \mathbf{7}^{\circ}$, $\alpha_{\mathbf{vg}} = \mathbf{4}^{\circ}$, multiple $\mathbf{y_{vg}}$ locations, $\mathbf{\Delta Z} = \mathbf{0}$in.

refers to the increment in wing normal load due to the presence of the VG, i.e. $\Delta Cn = Cn_{\text{with VG}} - Cn_{\text{ no VG}}$. The presence of secondary peaks in the incremental airloads near the tip for all the cases is similar to that observed in Figure 2.6.

Figure 2.8 shows the solution from a stronger vortex wake interaction with wing. The VG is set at $\alpha_{vg} = 8^{\circ}$ and placed at 46.5 inch at spanwise station. As noted in Figure 2.8(c), the direct interaction of vortex with wing results in complex vortex pair structures. The predicted airloads compare well with the experimental values in terms of peak amplitude and shape near around the vortex axis. However, some discrepancies are noticeable inboard of the interaction.

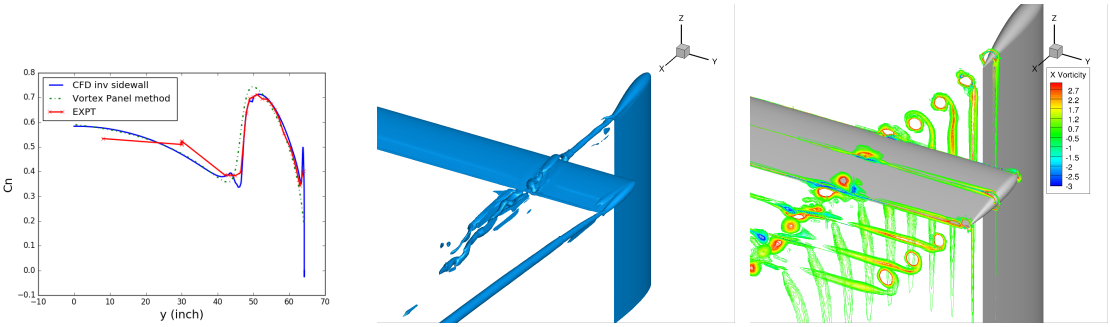

(a) Airloads (b) Q-criterion (c) Vorticity contours

Figure 2.8: Solution with $\mathbf{y_{vg}} = \mathbf{46.5}$in. (3.875c); $\alpha_{\mathbf{w}} = \mathbf{7}^{\circ}$, $\alpha_{\mathbf{vg}} = \mathbf{8}^{\circ}$, $\mathbf{\Delta Z} = \mathbf{0.0}$in.

With increasing vertical separation of the vortex wake with respect to the wing, the

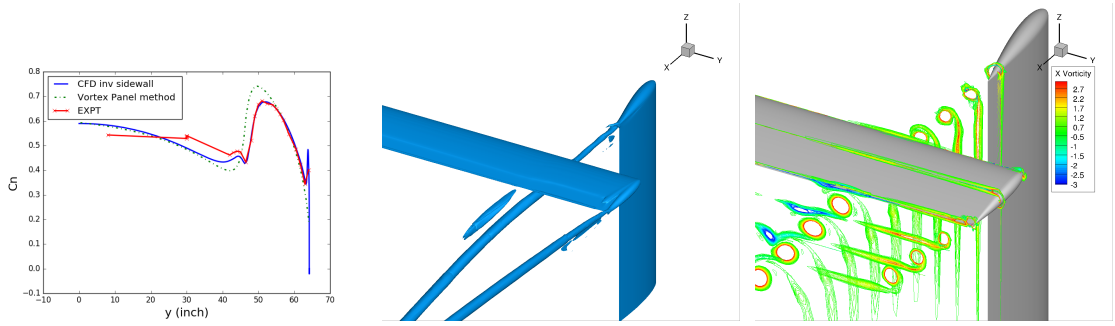

(a) Airloads (b) Q-criterion (c) Vorticity contours

Figure 2.9: Solution with $\mathbf{y_{vg}} = \mathbf{46.5}$in. (3.875c); $\alpha_{\mathbf{w}} = \mathbf{7}°$, $\alpha_{\mathbf{vg}} = \mathbf{8}°$, $\mathbf{\Delta Z} = \mathbf{-2.0}$in.

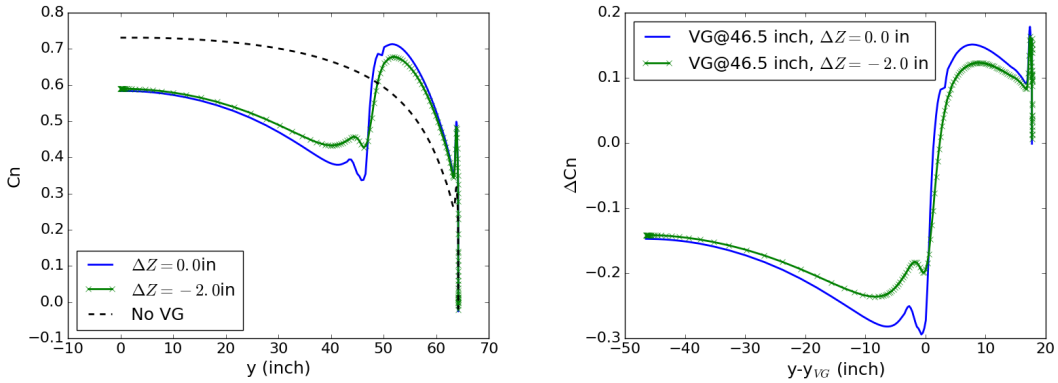

(a) Cn (b) ΔCn

Figure 2.10: Airloads for $\alpha_{\mathbf{w}} = \mathbf{7}°$, $\alpha_{\mathbf{vg}} = \mathbf{8}°$, VG at several vertical locations and $\mathbf{\Delta Z} = \mathbf{0.0}$in.

vortex interaction is less complex as shown in Figure 2.9. However, secondary vortices are still introduced in VG vortex wake after interaction with the wing. The effect of vertical separation of VG vortex with wing is summarized in Figure 2.10. The Figure shows that larger separation results in weaker lift increments with respect to the isolated wing. Also, the normal load spike present near the vortex gradually becomes less severe than the direct hit case.

2.2.5.1 Low-fidelity Model Validation

Figure 2.11 shows that the low-fidelity model is highly effective in capturing the airloads for the isolated wing. Figures 2.12 show consistently good predictions of airloads by the panel

method throughout the wing span, although there exist slight over-predictions near the vortex location. A similar trend is noticeable for the VG vertical sweep cases in Figures 2.8(a) and 2.9(a) in this case, with VG at larger $\alpha_{vg} = 8°$. The lift values are over-predicted again near the vortex, and the spanwise lift perturbation appears to be more gradual than that predicted by experiment and CFD. Overall, the low-fidelity model captures the essential aerodynamic loads very well. The over-prediction of the magnitude of the vortex-induced lift predictions is attributable to the fact that the vortex distortion is not modeled.

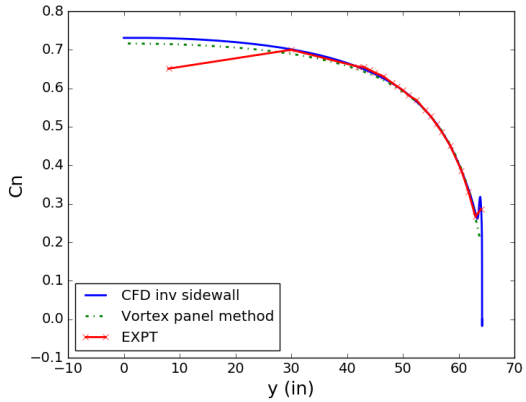

Figure 2.11: Validation of vortex panel method for wing only case; $\alpha_{\mathbf{w}} = \mathbf{7}°$.

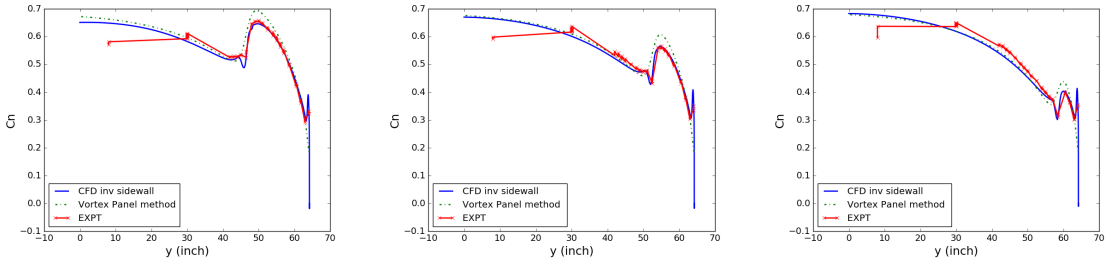

(a) VG at 46.5in (b) VG at 52.5in (c) VG at 58.5in

Figure 2.12: Validation of vortex panel method; $\alpha_{\mathbf{w}} = \mathbf{7}°$, $\alpha_{\mathbf{vg}} = \mathbf{4}°$, $\Delta Z = 0$in.

2.2.6 Surface Pressure Validation

Figure 2.13 compare the predicted surface pressure by the CFD with the experimental values for the VG placed at 46.5 spanwise station at a nominal direct hit vertical position with

$\alpha_{vg} = 4°$ and $\alpha_w = 7°$. The measurements are well-predicted by CFD. It should be mentioned here that the CFD pressure prediction incorporates a pressure coefficient correction factor of $\Delta C_p \sim -0.25$ owing to the free stream pressure correction due to blockage effect. The Figure also demonstrates the airload increments due to the vortex. The upwash due to the vortex at its outboard stations results in larger sectional normal forces. Similarly, the downwash at the inboard stations of the vortex results in smaller values of sectional normal forces. The computational predictions correlate well with the experiment.

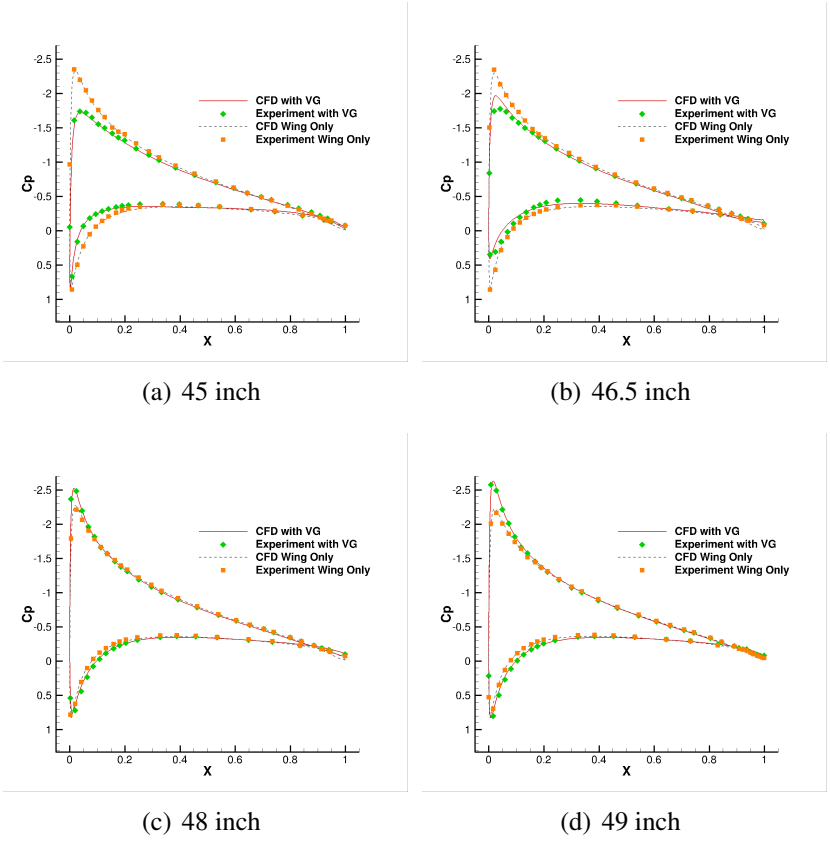

(a) 45 inch (b) 46.5 inch

(c) 48 inch (d) 49 inch

Figure 2.13: Surface pressure predictions for $\mathbf{y_{vg} = 46.5}$in. (3.875c);$\alpha_{\mathbf{w}} = \mathbf{7}°$, $\alpha_{\mathbf{vg}} = \mathbf{4}°$, $\mathbf{\Delta Z = 0}$in.

Similar sectional pressure plots are presented for the stronger vortex strength, i.e. $\alpha_{vg} = 8°$, but VG corresponding to a direct hit and at the same spanwise station of 46.5 inch and $\alpha_w = 7°$. The increments in normal load is more pronounced as expected. This is evident when pressure predictions at the 49 in span sections for weaker and stronger vortex cases

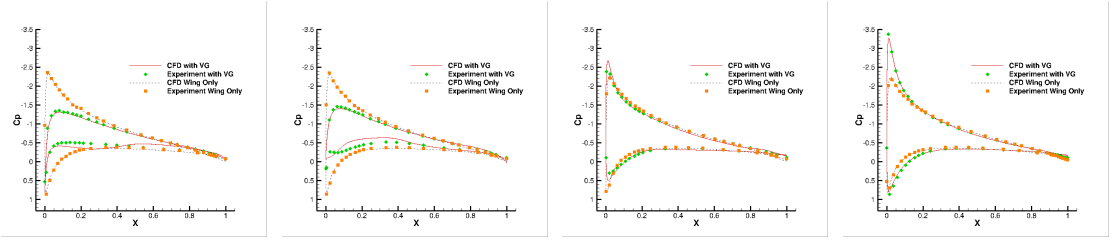

(a) 45 inch (b) 46.5 inch (c) 48 inch (d) 49 inch

Figure 2.14: Surface pressure predictions for $\mathbf{y_{vg}} = \mathbf{46.5}$in. (3.875); $\alpha_{\mathbf{w}} = \mathbf{7}^\circ$, $\alpha_{\mathbf{vg}} = \mathbf{8}^\circ$, $\mathbf{\Delta Z} = \mathbf{0}$in.

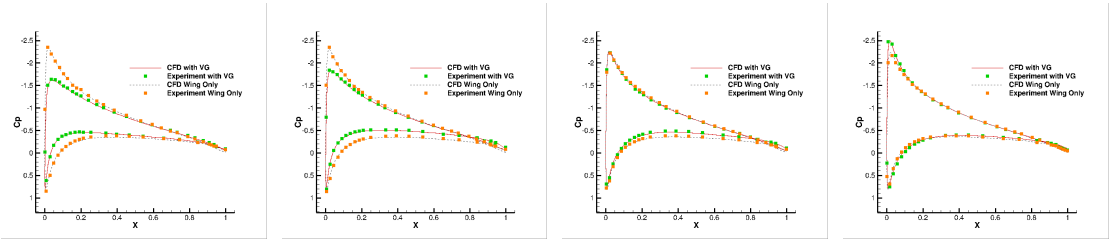

(a) 45 inch (b) 46.5 inch (c) 48 inch (d) 49 inch

Figure 2.15: Surface pressure predictions for $\mathbf{y_{vg}} = \mathbf{46.5}$in. (3.875c); $\alpha_{\mathbf{w}} = \mathbf{7}^\circ$, $\alpha_{\mathbf{vg}} = \mathbf{8}^\circ$, $\mathbf{\Delta Z} = \mathbf{-2}$in.

are compared to the experiment (figures 2.13(d) and 2.14(d)). However, once the vortex is moved vertically 2 inches below the wing ($\alpha_w = 7^\circ$), the incremental normal load changes are weaker, as noted in Figure 2.15, especially Figure 2.15(d). The sectional pressure plots follow the same general trend as the other two cases, i.e. positive increment on normal load outboard of the vortex and decrement on normal load inboard of vortex.

2.3 Propeller Wake-Wing Interaction

This section considers a more complex interaction case of propeller wake with a wing, a typical flow situation encountered in turboprops and distributed propulsion systems. This particular case is more interesting because of the presence of large axial and swirl velocities due to the strong propeller tip vortices. interaction on the wing has strong influence on its airloads.

The test case considered was experimentally investigated by Samuelsson [93, 94]. This

Table 2.1: Propeller conditions.

J (M_{tip})	0.7 (0.655)
C_T	0.23
U_∞ (m/s) (M_∞)	50 (0.15)
Reynolds number (prop tip)	1.96×10^6
Reynolds number (wing)	1.70×10^6

work considers two specific configurations from the experimental studies; one is the isolated propeller and the second configuration considers the propeller with wing in its wake. There have been several computational studies in the past, including recent inviscid Euler computations by Thom and Duraisamy [95, 43]. The present work pursues more detailed RANS computations. The experimental flow conditions are summarized in Table 2.1.

Low-fidelity model details: The sectional lift coefficient slope ($C_{l\alpha}$) and zero lift angles of attack ($\alpha_{L=0}$) are obtained using 2D CFD simulations. The $Cl\alpha$ values vary approximately between 5.15 to 5.4, and zero-lift angle of attack ($\alpha_{L=0}$) values vary approximately between negative 2.5 to 6.0 degrees. Further details are provided in the Appendix A.3.

2.3.1 Isolated Propeller Study

This section investigates the time-averaged wake features in an isolated propeller. The propeller geometry, representative of a typical medium sized turboprop commuter propeller, is composed mainly of NACA 6 series airfoil section with varying thickness and twist along the span. The propeller radius is 0.64m. The detailed geometry description can be found in Refs. [93, 94, 95].

The mesh system of the propeller blade with nacelle geometry is as shown in Figure 2.16. The blade mesh is discretized with a C-O mesh system, with spanwise mesh sections collapsing near the propeller tip to resolve the tip section flow and vortex. Figure 2.16(a) shows how blade mesh is blended onto the nacelle geometry at its root. Its grid size is $149 \times 181 \times 56$ along the chordwise, spanwise and wall normal direction, respectively. The nacelle mesh, which captures the blade wake flow features, is composed of

$175 \times 154 \times 400$ points along the azimuthal, nacelle wall normal and streamwise/nacelle-axis directions, respectively. This wake mesh resolution ensures approximately eight mesh points in the vortex core which has been found to be sufficiently accurate in capturing the vortex core [77, 95, 43] – see Appendix A.2. Taking advantage of the periodicity of the flow field for a four-bladed propeller, only one quadrant of the rotor system is considered. Figures 2.16(b) and 2.16(c) show that the propeller wake region is well-resolved in the nacelle mesh. The outer boundary is approximately 10 propeller radii from the nacelle, and about 20 propeller radii downstream. The computation is performed in the rotor inertial reference frame while the nacelle rotates along the propeller.

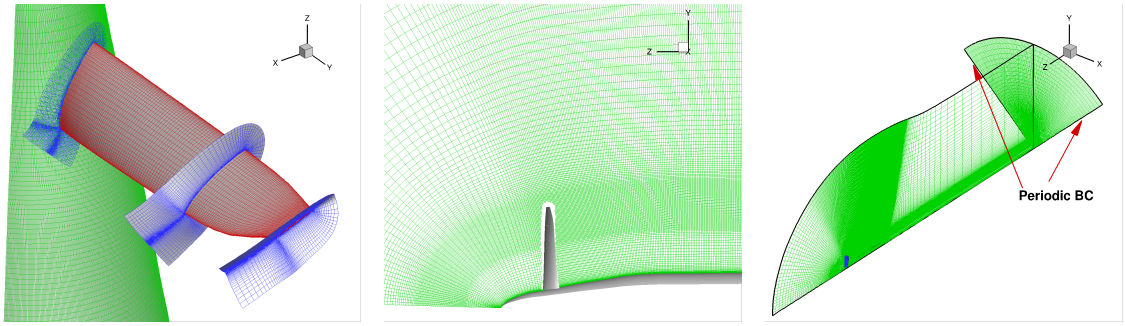

(a) Blended Blade mesh (b) Hole cut nacelle mesh (c) Full computational domain

Figure 2.16: Overset mesh system of isolated propeller configuration.

The converged propeller performance predictions $[C_T, C_P] = [0.236, 0.240]$ compare well with the experimental values of $[0.236, 0.230]$. Figure 2.17(a) reveals the quadruple helix structure with very slight contraction in its diameter as the vortices convect downstream of the nacelle. Q-criterion isosurface reveal evolution of trailed vortex structures in Figure 2.17(b). Figure 2.18 compares the sectional lift coefficient between the models. Although there is a slight over-prediction of lift using the vortex panel method, qualitatively the lift trend is well captured. The nature of the lift curve predicted from both the models are qualitatively typical of what is expected from a rotary wing or propeller, i.e. monotonically increasing ClM^2 outboard, before a sharp fall to zero values near the tip.

Axial velocity predictions from the high-fidelity model (CFD) at various planes down-

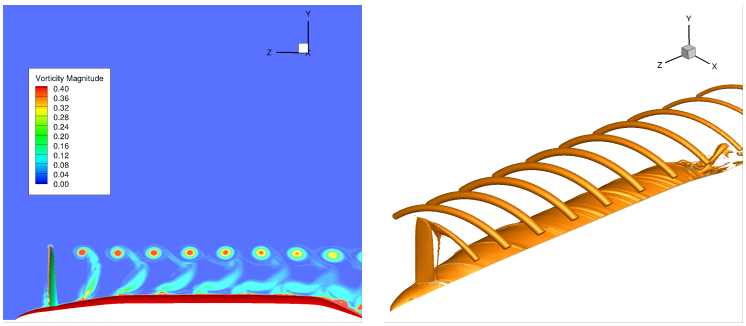

(a) Propeller wake (b) Q-criterion isosurface

Figure 2.17: Wake solutions of the isolated propeller configuration.

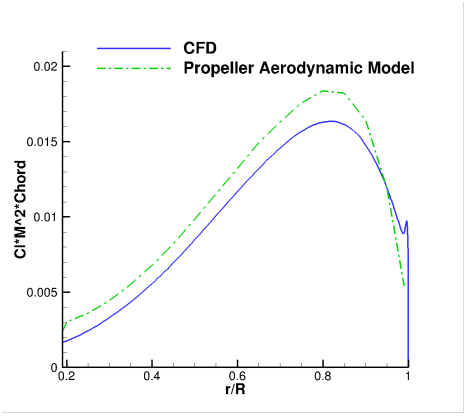

Figure 2.18: Sectional lift distribution on propeller.

stream of propeller are compared with experimental values in Figure 2.19. It is observed that the propeller induces axial velocities larger than 1.7 times the free stream velocity (Figs. 2.19(c) and 2.19(d)). It is observed that the axial velocity values are under-predicted at planes closer to the propeller (Fig. 2.19(a)), but the discrepancies reduce at planes farther away from propeller. This could be due to the difference in geometry used for computation compared to the experimental geometry. The Figures also show the axial velocity predictions by the propeller aerodynamic model. While consistent under-prediction is noticeable in all the vertical planes, the predictions are better in planes farther downstream of the propeller.

Figures 2.20 compare the swirl angles [2] at the aforementioned planes downstream of

[2]Swirl angle is positive in the rotation direction of the propeller (positive z-axis)

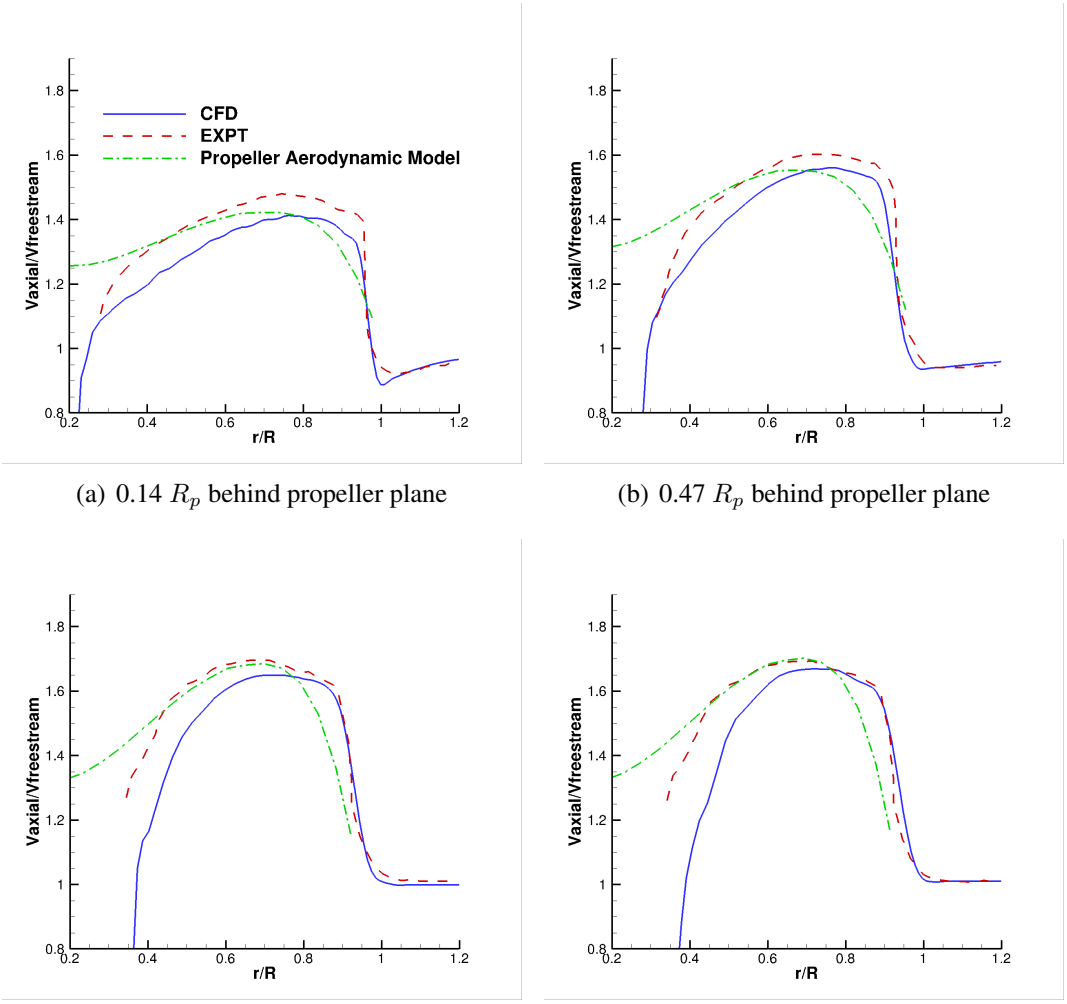

(a) 0.14 R_p behind propeller plane

(b) 0.47 R_p behind propeller plane

(c) 1.72 R_p behind propeller plane

(d) 3.0 R_p behind propeller plane

Figure 2.19: Axial velocity at several planes downstream of propeller.

the propeller. Swirl angle is the angle subtended by the tangential velocity with the axial velocity at rotor spanwise station. While the predicted swirl angles compare reasonably well with experimental values at most of the stations, the predictions at farther downstream planes are better. Swirl angle values as large as 20° (Fig. 2.20(a)) are observed near the root which gradually decay to zero values towards the tip as expected. The maximum swirl angle gradually reduces at planes farther away downstream of the propeller. In the Figures, the predictions by the propeller aerodynamic model are also included. In contrast to the axial velocity predictions, the swirl angle values are slightly over-predicted closest to the propeller, but slightly under-predicted farther downstream of the propeller. Overall, these

swirl angles are better-predicted at planes farther downstream of the propeller plane.

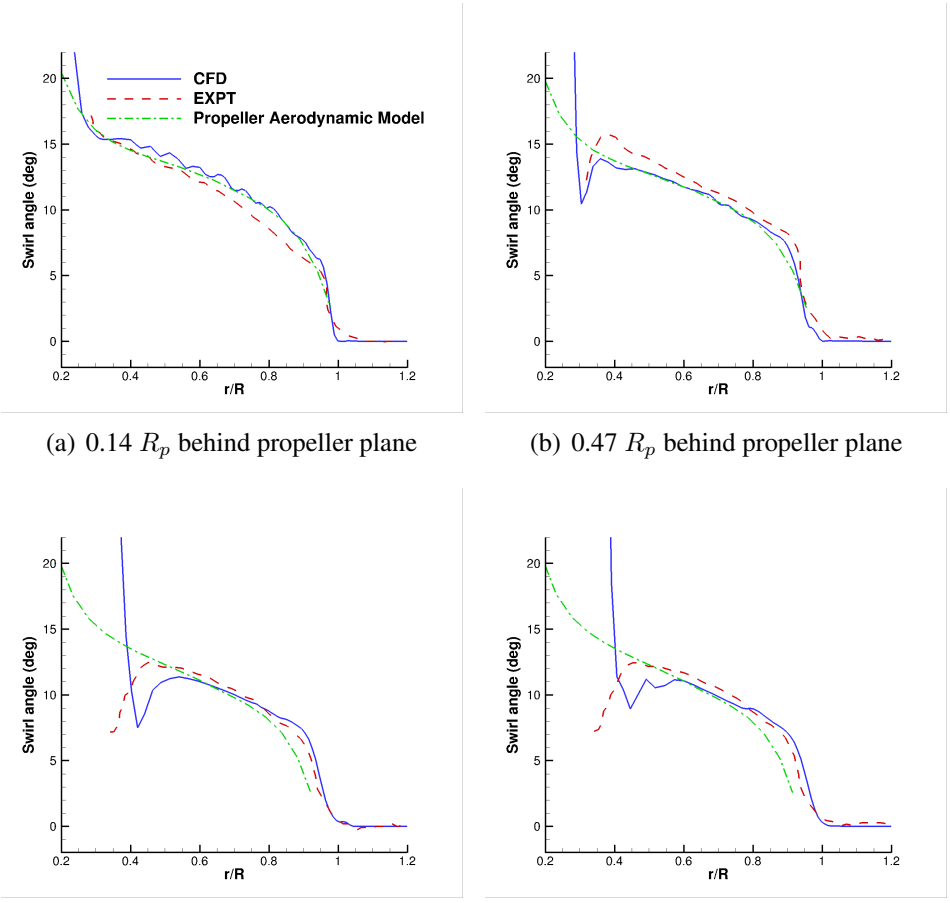

(a) 0.14 R_p behind propeller plane

(b) 0.47 R_p behind propeller plane

(c) 1.72 R_p behind propeller plane

(d) 3.0 R_p behind propeller plane

Figure 2.20: Swirl angle at several planes downstream of propeller.

2.3.2 Propeller Wake-Wing Interaction

The propeller wake interaction with the nacelle-mounted wing is considered in this section. The wing is mounted downstream of the propeller (0.174m below the nacelle leading edge). It has a constant NACA$63_{(010)}A012$ airfoil section and spans 2.0m (a semi-span of 1.0m and aspect ratio of 2.0) in total. The details of the geometry can be found in [93].

The computational domain for the propeller-wing configuration is summarized in Figure 2.21. Because of the presence of the wing, all four rotor blades are considered, instead of just a quadrant as in the isolated rotor case. In addition, the nacelle mesh system is split

into two domains (Fig. 2.21(b)): a) an upper domain oversetting the propeller blade mesh system, which rotates along with the propeller and b) the lower domain that remains static and resolves the vortex wake trailed from the upper nacelle mesh. The information transfer across the two nacelle domains is achieved by incorporating a sliding boundary condition at the interface.

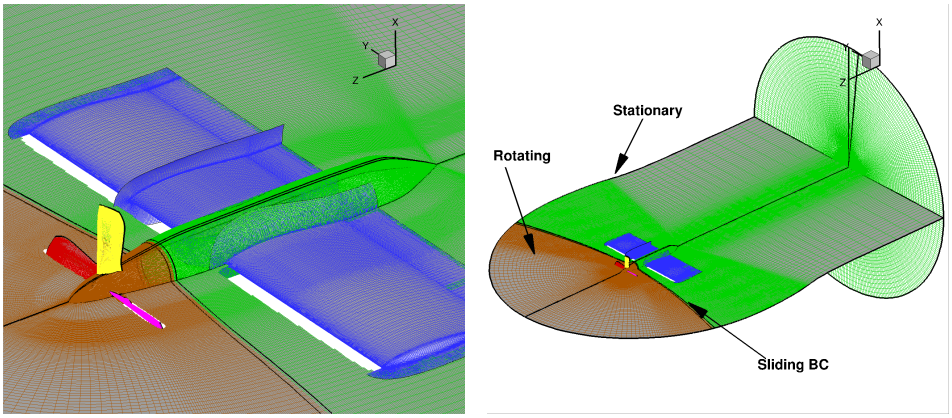

(a) Blended Wing mesh and hole cut (b) Full computational domain

Figure 2.21: Overset mesh system of the propeller-wing configuration.

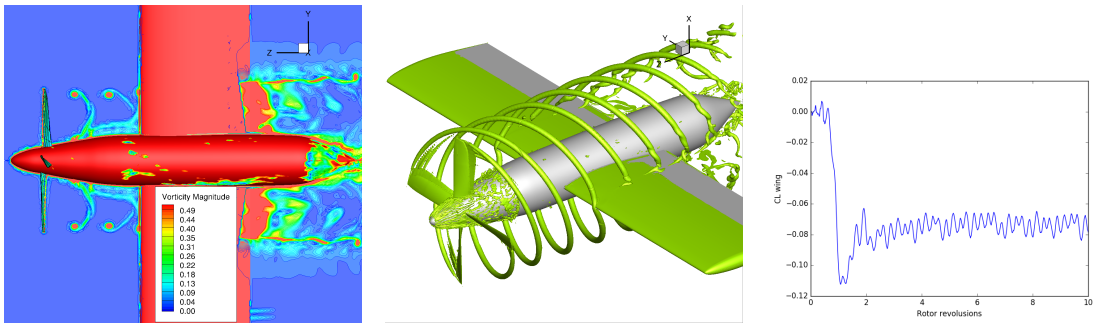

(a) Propeller wake (b) Q-criterion isosurface (c) Wing lift history

Figure 2.22: Propeller-wing configuration and thrust predictions.

Complex flow features of the propeller vortex wake interaction with the wing are revealed in Figures 2.22. Although the diameter of the helical vortex system contracts slightly downstream of propeller, it tends to grow downstream of the wing after the complex interaction. The vortex wake is found to disintegrate and grow weaker downstream of the wing after the interaction. Figure 2.22(c) further show the $4/rev$ wing lift history, as ex-

pected from a 4-bladed propeller wake aerodynamics. The lift history over ten revolutions also confirms that the solution converges to a limit cycle. Figure 2.23 validates the pre-

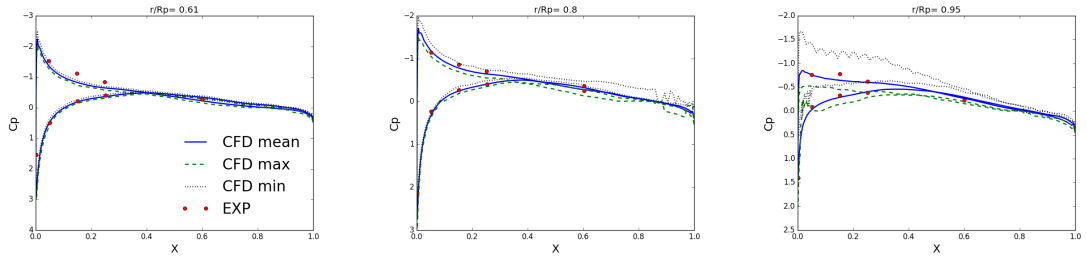

(a) r/Rp=0.61 (b) r/Rp=0.80 (c) r/Rp=0.95

Figure 2.23: Wing pressure distribution at several spanwise stations.

dicted pressures at several spanwise stations of the wing. The plots also show the pressure fluctuations over one rotor revolution and as expected the fluctuations are the largest near $r/Rp = 0.95$ where the propeller trailed vortex wake directly interacts with the wing.

The low-fidelity predictions of lift distribution on the wing are further compared with the values predicted by the high-fidelity model for both the isolated wing as well as the wing immersed in the propeller wake. A free stream angle of $\alpha_w = 5°$ for the wing is considered. The interaction of the wing with the propeller stream influences the axial and swirl velocities. Consequently, the expressions for c_s and c_a in the swirl and axial velocity equations, Eqns. (2.7) and (2.8), respectively, are modified to $c'_s = 0.5c_s$ and $c'_a = 0.5c_a$. The swirl velocity is appended to the right hand side of Eq. (2.1):

$$\Gamma = A^{-1}b \pm V_{swirl} \tag{2.11}$$

where the $\pm$ signs is determined based on the rotational direction of the propeller. Finally, the pressure differential equation, Eq. (2.2), is now updated with the updated velocity vector:

$$\vec{v} = [U(t) + u_w + V_{axial}\cos\alpha, V(t) + v_w + V_{swirl}, W(t) + w_w - V_{axial}\sin\alpha] \tag{2.12}$$

It should be noted that $V_{swirl}(i,j)$ and $V_{axial}(i,j)$ are non-zero only in the propeller slip stream tube, and therefore their effects are applied only on those panels that lie within the tube while mapping $V_{swirl}(r)$ and $V_{axial}(x,r)$ to $V_{swirl}(i,j)$ and $V_{axial}(i,j)$, respectively. The low-fidelity model uses 15 and 60 panels in stream- and spanwise directions, respectively. The lift distribution of the wing-propeller interaction predicted by both the low- and high-fidelity models is shown in Figure 2.24. It is evident that the wing-alone as well as

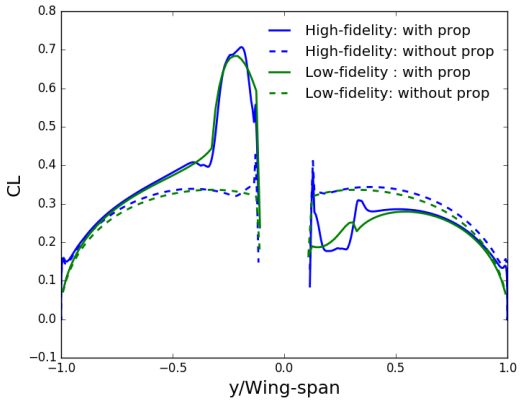

Figure 2.24: Lift distribution of isolated wing and wing in propeller wake for $\alpha_w = 5°$.

the wing-propeller interaction results obtained by both low- and high-fidelity models are in very good agreement, thus providing a further validation for the low-fidelity model. It is observed that the high-fidelity lift values show a slight dip in the vicinity of the nacelle, but that is not modelled by the low-fidelity model.

CHAPTER 3

A Framework for Flight Simulation of Rotary-Wing Aerial Vehicles

In trajectory planning and control design for rotary-wing UAVs, highly simplified models are typically used to represent the vehicle aerodynamic, dynamics and the operating environment. The goal of this chapter is to perform real-time, but realistic, flight simulations and trajectory planning for a quadrotor in low-altitude (< 500 m) atmospheric conditions.

The aerodynamic model for rotor performance is similar to the aeromechanical model presented in the previous chapter, Section 2.1.2.2. Large-eddy Simulation (LES) of the atmospheric boundary layer is used to accurately represent the operating environment of unmanned air vehicles. A reduced-order version of the atmospheric boundary-layer data as well as the popular Dryden model are used to assess the impact of accuracy of the wind-field model on the predicted vehicle performance and trajectory.

The wind model, aerodynamics, and control modules are integrated into a six-degree-of-freedom flight simulation environment with a fully nonlinear flight controller. Simulations are performed for two representative flight paths, namely, straight and circular paths. Results for different wind models are compared and the impact of simplifying assumptions in representing rotor aerodynamics is discussed. The simulation framework and codes are open sourced for use by the community. The materials in this chapter are heavily drawn from Ref. [74].

3.1 Modeling Atmospheric Gust Effects

3.1.1 Atmospheric Boundary Layer Simulation Using LES

The popular approach to represent atmospheric gusts in aviation applications such as trajectory estimation relies on stochastic formulations [96, 97] and its variants [98] all of which incorporate knowledge of the canonical spectral energy function [99]. While computationally efficient, such methods have two major limitations: (i) use of parameterized equilibrium phenomenology that is often inaccurate, and (ii) not explicitly accounting for the structure of the spectral energy tensor. In reality, the atmospheric boundary layer (ABL) turbulence is characterized by strong and highly coherent eddying structure that contributes to the uncertainty associated with the predicted trajectory. Such limitations in wind forecasting for air traffic management (ATM) is well known as discussed in [100]. In a more recent study, Galway *et al.* [101] show that eddy-resolving Computational Fluid Dynamics (CFD) wind fields can cause significant trajectory effects to unmanned rotorcrafts. In this study, we build on this direction and adopt scientifically accurate, high fidelity Large Eddy Simulations (LES) of the ABL that capture energy containing turbulence eddying structures at scales that are dynamically important for unmanned aerial flight.

The canonical ABL used to generate the wind model data for this study is modeled as a rough flat wall boundary layer with surface heating from solar radiation, forced by a geostrophic wind in the horizontal plane and solved in the rotational frame of reference fixed to the earth's surface. The lower troposphere sets the upper height limit for ABL, and is represented with a capping inversion and the mesoscale effects through a forcing geostrophic wind vector. The planetary boundary layer is different from engineering turbulent boundary layers in three major ways: 1) Coriolis Effect: The rotation of the earth causes the surface to move relative to the fluid in the ABL, which results in angular displacement of the mean wind vector that changes with height, 2) Buoyancy-driven turbulence: The diurnal heating of the surface generates buoyancy-driven temperature fluc-

tuations that interact with the near-surface turbulent streaks to produce turbulent motions, and 3) Capping Inversion: A layer with strong thermal gradients that caps the microscale turbulence from interacting with the mesoscale weather eddies.

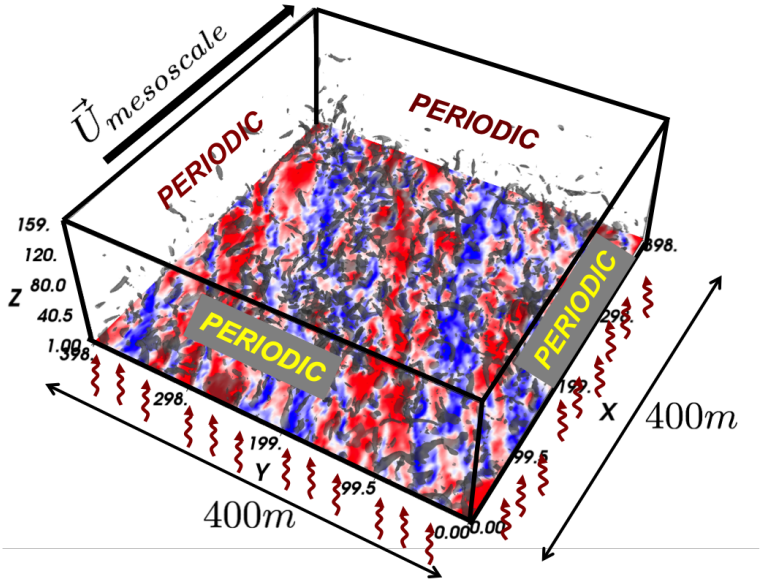

Figure 3.1: Schematic showing the Coriolis effect in a 3D visualization of ABL turbulence for a neutral ABL with $-z_i/L = 0$ using LES.

In Figure 3.1, the mesoscale wind drives the ABL along the x-direction while the rotation of the earth's surface orients the surface layer turbulence to nearly 30 degrees relative to the imposed wind vector (along the streaks). The isosurfaces (grey) show vorticity magnitude at a value of $0.45\ s^{-1}$ and the isocontours show the horizontal fluctuating velocity. The blue regions denote low speed streaks while the red regions represent high speed streaks.

3.1.1.1 LES Methodology and Simulation Design

The Reynolds number of the daytime atmospheric boundary layer is extremely large. Hence, only the most energetic atmospheric turbulence motions are resolved. The eddies in the surface layer are highly inhomogeneous in the vertical (z), but are clearly homogeneous in the horizontal direction. LES attempts to resolve to the order of the grid scale, the energy

containing eddy structures.

Using a grid filter, one can split the fluctuating instantaneous velocity and potential temperature into a resolved and sub-filter scale (SFS) components. The canonical, quasi-stationary equilibrium ABL is driven from above by the horizontal mesoscale 'geostrophic wind' velocity vector, u_{g}, and the Coriolis force is converted into a mean horizontal pressure gradient oriented perpendicular to u_{g}. In the LES of ABL, the molecular viscous forces are neglected and the surface roughness elements of scale z_0 are not resolved by the first grid cell ($z_0 \ll \Delta z$). Buoyancy forces are accurately predicted using the Boussinesq approximation. The momentum equation for resolved velocity contains a sub-filter scale (SFS) stress tensor that is modeled using an eddy viscosity formulation with the velocity scale being generated through a 1-equation formulation for the SFS turbulent kinetic energy [102, 103]. The LES equations are shown below in Eqs. (3.1)-(3.3). A detailed discussion of the numerical methods is available in [104, 105, 106]. In Eq. (3.1), $\tilde{u}$ represents the filtered velocity, τ^{SFS} the subfilter scale stresses, p^* the modified pressure and $\tilde{\theta}$ the filtered potential temperature.

$$\nabla \cdot \tilde{u} = 0, \tag{3.1}$$

$$\frac{\partial \tilde{u}}{\partial t} + \nabla \cdot (\tilde{u}\tilde{u}) = -\nabla p^* - \nabla \cdot \tau_u^{\mathrm{SFS}} + \frac{g}{\theta_0}\left(\tilde{\theta} - \theta_0\right) + f \times (u_{\mathrm{g}} - \tilde{u}), \tag{3.2}$$

$$\frac{\partial \tilde{\theta}}{\partial t} + \nabla \cdot \left(\tilde{\theta}\tilde{u}\right) = -\nabla \cdot \tau_\theta^{\mathrm{SFS}}. \tag{3.3}$$

While the effects of buoyancy are highly pronounced in ABL turbulence, and significantly impact its structure [105, 106], we chose a more benign neutral stratification for this study. The domain size is restricted to 400 m $\times$ 400 m $\times$ 600 m, which is sufficiently large to capture both the atmospheric scales as well as those relevant to small fixed wind unmanned vehicles. The cartesian LES grid has a resolution of 200 m $\times$ 200 m $\times$ 300 m for a uniform spacing of 2 m in each spatial direction. To realistically mimic the interface between the mesoscale and microscale atmospheric turbulence, a capping inversion was specified at a

height of 280 m. The surface heat flux is set to zero for this neutral ABL simulation and a Coriolis parameter of $f = 0.0001$ s^{-1} is chosen to represent continental United States. The bottom surface is modeled as uniformly rough with a characteristic roughness scale of 16 cm that is typical of grasslands. The dynamical system described in Eqs. (3.1)-(3.3) is forced by an imposed mean pressure gradient, $\nabla \bar{P}$ usually specified in terms of a geostrophic wind as $\nabla \bar{P} = -f \times u_{\mathrm{g}}$. For this model, u_{g} magnitude is set to 8 m/s which corresponds to a moderately windy day. The equation system is solved using the pseudo-spectral method in the horizontal with periodic boundary conditions and second-order finite difference in the vertical. The time marching is accomplished using a third-order Runge-Kutta method. The computational set-up is exactly as shown in Figure. 3.1. Further details about the computational methods and models can be obtained from [105, 106, 104].

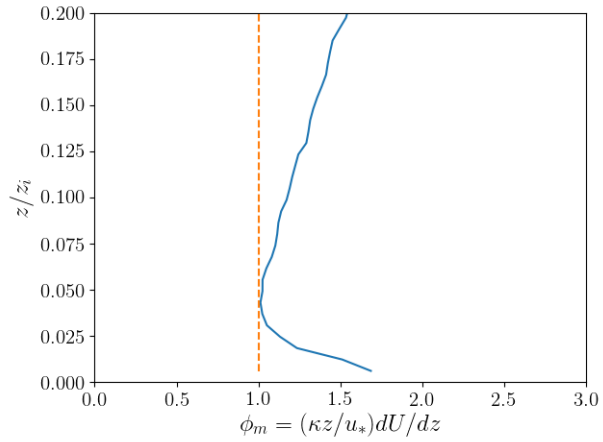

Figure 3.2: Comparison of the non-dimensional mean velocity gradients in the surface layer for neutral ABL with $\kappa = 0.4$.

3.1.1.2 Validation of Results

Large eddy simulation (LES) is well established as a high fidelity bench tool for modeling near surface atmospheric flows. The fidelity of the modeling framework has been validated for equilibrium conditions using experimental data [107] and well known phenomenology [104]. In this study, we adopt a similar strategy and assess the non-dimensional near-wall scaling from simulation data with respect to the law of the wall, and Monin-Obukhov

(M-O) similarity theory arguments for neutral stratification. Particularly, we compute the non-dimensional mean gradient $\Phi_{\mathrm{M}} = \frac{\kappa Z}{u_\tau} d\langle\tilde{u}\rangle/dz$ which should be closer to unity in the inertial logarithmic region of the ABL. In the above, the non-dimensionalization is performed using the appropriate choice of near-surface parameters for length (distance from the wall, z) and velocity (friction velocity, u_τ). For a constant value of the mesoscale wind and surface heat flux, the turbulent flow field evolves into a fully developed equilibrium boundary layer. After verifying the existence of statistical stationarity, converged statistics were estimated. Fig. 3.2 shows the near-wall variation of Φ_{M} as a function of normalized distance from the surface, (z/z_{i}), where z_{i} is the height of the ABL. We observe that Φ_{M} is nearly unity with small deviations arising from a combination of inaccuracies including numerical errors and near-wall modeling [108]. The LES quality is considered acceptable as long as these deviations are small.

3.1.2 Reduced-order Wind Representations

After obtaining wind data from the LES described earlier, a reduced-order representation of the atmospheric boundary layer (ABL) data can be constructed to assess the importance of the details of the wind field, and to reduce the memory requirements, proper orthogonal decomposition [109] is utilized. Given a matrix A of size $m \times n$, the singular value decomposition is given by:

$$A_{\mathrm{m\times n}} = \hat{U}_{\mathrm{m\times n}} \Sigma_{\mathrm{m\times m}} V^*_{\mathrm{n\times n}},$$

where $\hat{U}, \Sigma$ and V are matrices of the left singular basis vectors, singular values and unitary right singular vectors, respectively. For every component of velocity, the data is stacked into a rectangular matrix. That is, each column represents time instances, and each row has the velocity in the three dimensions stacked as a column vector of length $Nx \times Ny \times Nz$.

The fraction of energy corresponding to each singular value, $\frac{\sigma^2(i)}{\sum \sigma^2(i)}$, is shown in Figure 3.3.

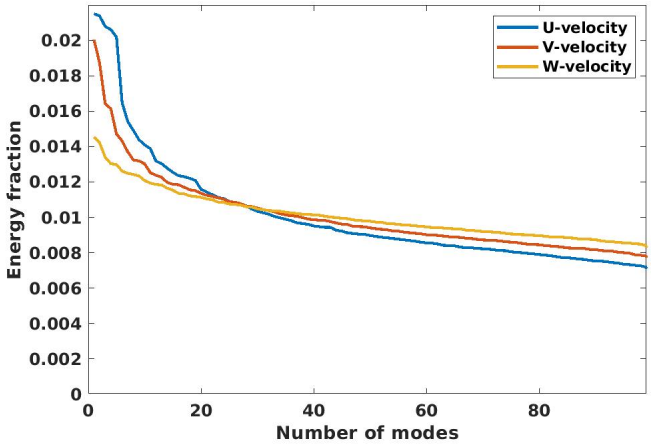

Figure 3.3: Energy contained in each singular mode.

A reduced-order representation can be constructed by utilizing projections on a truncated number of modes $N < 100$. For the wind data, we have chosen N to be 10 modes, and have reconstructed the new wind fields as will be presented in the Results section.

3.1.3 A Benchmark Wind Model: Dryden Turbulence Model

Having LES wind data, one can determine mean wind velocities by temporally and spatially averaging the data. Once the mean wind is known (via simulation or experimental measurements), there are empirical models that estimate the velocity fluctuations such as the Dryden model [97], which is a well-known benchmark wind model. The Dryden wind turbulence model uses an empirical spectral representation to add velocity fluctuations to the mean velocity. In this work, a continuous representation of the Dryden velocity spectra with positive vertical and negative lateral angular rates spectra is used. This representation is based on Military Handbook MIL-HDBK-1797B [110]. The inputs to the Dryden model are altitude, vehicle velocity (in the inertial reference frame) and direction cosine matrix, and the output is the gust velocity in the body frame. The mean wind velocity is then added to the fluctuations to represent the full wind.

The current model provides the mean wind velocity using the U.S. Naval Research Lab-

oratory HWM^{TM} routine. The typical inputs to this model are altitude, longitude, geopotential altitude, and the specific time of interest. The model predictions vary for different locations in the world and time of the year and are of a very low fidelity compared to the ABL simulation. Thus, we have used the ABL data (Section 3.1) to input the wind magnitude and direction for comparison purposes.

Data from sample atmospheric simulations is used to determine the magnitude of the wind velocity and the wind direction that are input to the aforementioned built-in MATLAB functions. Specifically, the mean wind speed and direction at 6 m are inputs to Dryden Wind Turbulence Model. Those values are approximately 3.40 m/s and 240° , respectively. It is noted that the wind direction is measured from the North in a clock-wise positive setting.

3.2 Aerodynamic Model

In this work, each rotor of a quadrotor is modeled individually using fundamental potential flow theory, while taking into account tools from helicopter rotor aerodynamic modeling. Blade element momentum theory was used in this work as the rotor inflow ratio varies radially across the blade span. Also, the vehicle inflow dynamics at each time instant is treated as quasi-steady. As a prototypical example, Mishra *et al.* [76] utilized an adaptation of blade element momentum theory from [48] and validated their steady thrust predictions with CFD simulations. In fixed-wing aircraft, the flight condition is essentially similar to vertical flight of rotary-wing aircraft. It is noted that the model used in this study still involves a high degree of simplification in forward flight. More advanced rotor aerodynamic models, that consider in-plane inflow to the rotor disk (neglected in the current model), have the potential to improve the accuracy of the predictions. Such models may be replaced as an independent block without any further modifications required in the flight simulation package.

Blade element momentum theory uses and combines the two fundamental aerodynamic theories [48], namely momentum and blade element theories are used. Momentum theory relates the thrust coefficient (C_{T}) to inflow velocity ratio where rotor is treated as a disk through which a flux of airflow passes. Hence, it does not process any information about the blade shape. On the other hand, the blade element theory uses blade geometric and aerodynamic characteristics such as twist, chord length distribution. Blade element theory can be used to determine the thrust coefficient using strip theory to integrate lift over the blade span. The formulation of the aerodynamic model is adopted from Section 2.1.2.2 with some minor changes. The sectional lift for higher effective angles of attack ($\alpha_{\text{eff}} = (\Theta + \alpha_{L=0} - \Phi)$) can be represented by a post-stall model [111]. That is, Eq. (2.3) can be replaced by Eq. (3.4):

$$\begin{aligned} C_{\mathrm{l}} =& (1-\sigma) C_{l_\alpha} \alpha_{\text{eff}} + \sigma [2 \operatorname{sign}(\alpha_{\text{eff}} - \alpha_{L=0}) \sin^2(\alpha_{\text{eff}} - \alpha_{L=0}) \cos(\alpha_{\text{eff}} - \alpha_{L=0})], \\ \sigma =& \frac{1 + e^{-M(\alpha_{\text{eff}} - \alpha_{L=0} - \alpha_0)} + e^{M(\alpha_{\text{eff}} - \alpha_{L=0} + \alpha_0)}}{[1 + e^{-M(\alpha_{\text{eff}} - \alpha_{\mathrm{L=0}} - \alpha_0)}][1 + e^{-M(\alpha_{\text{eff}} - \alpha_{\mathrm{L=0}} + \alpha_0)}]}. \end{aligned} \tag{3.4}$$

σ in Eq. (3.4) is the blending function , $\pm\alpha_0 = \pm 20.6^\circ$ are the cutoffs and $M = 50$ is the transition rate.

In blade element momentum theory [48], the rotor inflow ratio can be determined as a function of the flight condition parameters and geometric characteristics of the rotor by equating the thrust obtained from momentum and blade element theories. Eq. (2.4) can be rewritten as:

$$\lambda(r) = \sqrt{\left(\frac{\sigma C_{l_\alpha}}{16F} - \frac{\lambda_c}{2}\right)^2 + \frac{\sigma C_{l_\alpha}}{8F}\Theta r} - \left(\frac{\sigma C_{l_\alpha}}{16F} - \frac{\lambda_c}{2}\right), \tag{3.5}$$

where λ_{c} is the climb ratio. Let $V_{\mathrm{rel}_{B_z}}$ denote the total inlet velocity, and let V_{tip} denote the blade tip velocity. In this study, λ_{c} is obtained as

$$\lambda_c = \frac{V_{\mathrm{rel}_{B_z}}}{V_{\text{tip}}}. \tag{3.6}$$

Note that $V_{\text{rel}_{B_z}}$ denotes the projection of the relative wind velocity along the positive z direction of the body frame (i.e., positive inlet flow) and the positive sense of z is defined downward (see Fig. 3.5). Also, a positive λ_c implies climb for which the relative velocity in body frame is positive. This model can be used in forward flight, although it may not be accurate given that it was designed for vertical flight. An accurate forward flight model will later be developed in Chapter. 4.

The total thrust of a rotor is obtained by integrating the sectional lift from hub ($R_{\text{min}} = 0.1R$ for the blade used in this study) to tip as follows:

$$T = N_b \int_{R_{\text{min}}}^{R} \frac{1}{2} \rho C_l [(r\omega)^2 + (\lambda V_{\text{tip}})^2] c(r)\, dr, \tag{3.7}$$

where $c(r)$ is the chord distribution from hub to tip. This model for a single rotor is compared to the experimental data of Ref. [112] in Fig. 3.4. The results correspond to a rotor with a radius of 7.62 cm, an average chord of 1.10 cm, and the twist distribution varying approximately from 25 to 5 degrees from root to tip. It is noted that $C_{l_\alpha} = 1.7059\pi$, and absolute value of the zero-lift angle of attack, $\alpha_{L=0} = 4$.

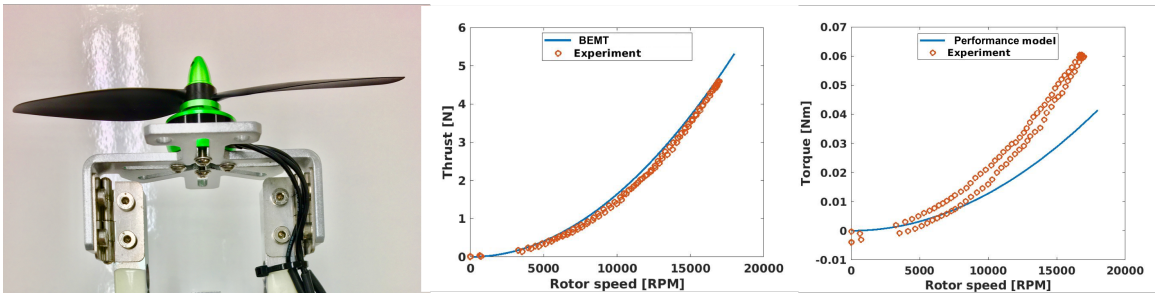

Figure 3.4: Comparison between experimental data and the radial inflow model (BEMT) for hovering flight.

As noted in Fig. 3.4, the thrust values predicted by the radial inflow model are in good agreement with the experimental data while the torque values are underestimated. Torque values predicted by the performance model (that will be discussed next) only represent the resisting torque due to aerodynamics, however, additional frictional resistance in the shaft

of the propeller may have manifested itself in the experimental torque data.

3.2.1 Torque and Power Performance Model

For a standard quadrotor (with a '+' rotor configuration shown in Fig. 3.5), the roll and pitch moments (τ_{x} and τ_{y}) are produced using differential thrust among the four rotors:

$$\tau_{\mathrm{x}} = l(T_4 - T_2), \qquad \tau_{\mathrm{y}} = l(T_1 - T_3), \tag{3.8}$$

where l is the distance between the rotor and center of mass (c.m). By modulating the RPM of each rotor, it is possible to modify thrust and generate the required torque. The yaw moment, τ_z is obtained by adding the reactive yaw moment of each rotor. The reactive moment for each rotor is a function of multiple aerodynamic contributors that will be discussed in detail next.

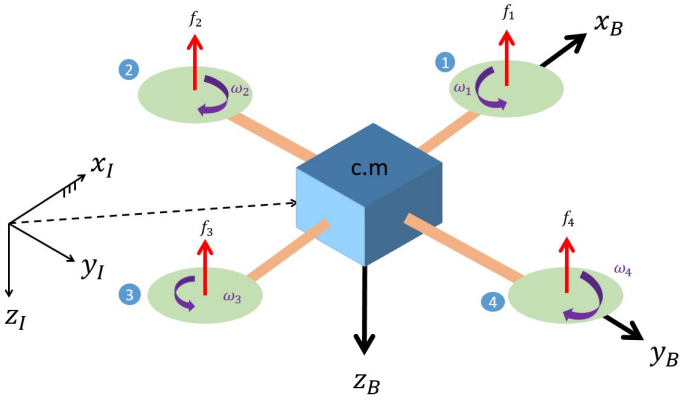

Figure 3.5: Definition of the body and the inertial frames of reference; positive sense of rotation and the respective positive directions of forces and torques are also presented.

In forward flight, for a single rotor, the power required to overcome the resisting moment can be categorized as follows (in coefficient form, non-dimensionalized by $\rho\pi R^5\omega^2$) :

- Induced power: Power that is used to overcome lift-induced drag, $C_{\mathrm{P,ind}} = \frac{1.15C_{\mathrm{T}}^2}{2\sqrt{\lambda^2+\mu^2}}$ in which the advance ratio is defined as $\mu = \sqrt{V_{\mathrm{rel}_{\mathrm{B}x}}^2 + V_{\mathrm{rel}_{\mathrm{B}y}}^2}/V_{\mathrm{tip}}$.

- Blade profile power: Power required to overcome the viscous drag of each blade, $C_{\text{P,0}} = \frac{\sigma C_{\text{d0}}}{8}(1 + 4.6\mu^2)$ where C_{d0} is the profile drag coefficient ($C_{d0} = 0.008$).

- Parasite power: Power required to overcome the drag exerted on the body of the vehicle due to the incoming free stream, $C_{\text{P,p}} = \frac{1}{2}\frac{f}{A}\mu^3$. It is noted that for a rotor of a quadrotor, a $1/4$ factor should be multiplied to $C_{\text{P,p}}$. f is the equivalent flat plate area that models the body of the vehicle, f/A can be approximated to be 1.

- Climb or descent power: the power required/produced in climbing/descending flight, $C_{\text{P,c}} = C_{\text{W}}\lambda_{\text{c}}$.

Therefore, the total power required is:

$$C_{\text{P}} = \frac{1.15C_{\text{T}}^2}{2\sqrt{\lambda_0^2 + \mu^2}} + \frac{\sigma C_{\text{d0}}}{8}(1 + 4.6\mu^2) + \frac{1}{8}\frac{f}{A}\mu^3 + C_{\text{W}}\lambda_{\text{c}}. \tag{3.9}$$

The power and torque coefficients are the same ($C_{\text{P}} = C_{\text{Q}}$). Thus, given Eq. (3.9), one can express the yaw torque due to the i-th rotor as $Q_i = C_{\text{P}}\rho\pi R^5\omega_i^2$. Thus, the total reactive torque can be written as

$$\tau_{\text{z}} = \sum_{i=1}^{4} Q_i(sign(\omega)). \tag{3.10}$$

The term $sign(\omega)$ is required to make sure that the torque value associated with each rotor is taken into account with its correct sign where counter-clock wise rotation direction provides a positive reaction torque (For instance, see rotor number 1 in Fig. 3.5). For yaw control, it is possible to mount the rotors with a small cant angle to improve the yaw authority of the platform with negligible reduction in vertical thrust. This is a desired configuration, in particular, when high-RPM, low-torque motors are used.

3.2.2 Lumped Drag Model

The total drag on a quadrotor involves combinations of different aerodynamic effects some of the contributions to which were discussed above in the context of the required torque/power

to turn the four rotors at the desired speed given a flight condition. It is noted that one physical phenomenon can lead to both additional required power and drag force on the quadrotor. The prominent contributors to the drag of a quadrotor are induced drag, blade profile drag and translational drag due to the swirl of the induced velocity in forward flight. Parasite drag is typically small relative to the other contributors.

These parameters were studied in [113], and a lumped drag model for a quadrotor was introduced in Eq. (3.11) that related the drag red(defined in the body frame) to thrust value and relative velocity seen by the quadrotor:

$$\mathbf{D} = - \begin{bmatrix} \bar{c}_d & 0 & 0 \\ 0 & \bar{c}_d & 0 \\ 0 & 0 & 0 \end{bmatrix} T \, \mathbf{V}_{\text{rel}_\text{B}}, \tag{3.11}$$

where $\bar{c}_d$ is the lumped drag coefficient that was inferred from measured onboard accelerometer data for a typical quadrotor; $\bar{c} = 0.04 \pm 0.0035$. In this study, $\bar{c} = 0.04$ is used. Drag in the inertial frame is in the direction of the incoming velocity, whereas Eq. (3.11) represents rotor in-plane force that has no component in the z direction of body frame coordinate system. This model will be revisited and replaced in Section 4.4.

In general, several interactions exist between the rotor blades and the wake, and between the rotor and airframe. Diaz and Yoon [34] performed high-fidelity CFD simulations and suggested that the airframe can reduce rotor-rotor interaction, and hence increase the total thrust. With the requirement for the models to be near real-time, the aerodynamics of each rotor is treated individually and rotor-rotor interaction effects are not considered in this study.

3.3 Vehicle Dynamic Model and Control Hierarchy

3.3.1 Dynamic Modeling

The schematic of the vehicle and frames of references are given in Figure 3.5. The body frame, $B = \{x_{\mathrm{B}}, y_{\mathrm{B}}, z_{\mathrm{B}}\}$ is needed to describe the orientation of the vehicle with respect to the inertial frame, whereas the inertial frame, $I = \{x_{\mathrm{I}}, y_{\mathrm{I}}, z_{\mathrm{I}}\}$ is used to locate the position of the center of mass of the vehicle. The modulation of the voltage to the electrical motor of each rotor modifies the angular velocity of each propeller, ω_{i}, $(i = 1, \cdots, 4)$, which in turn governs both the rotational and translational dynamics due to the generated forces, f_{i}, $(i = 1, \ldots, 4)$. The angular velocities are paired (*i.e.*, the first and the third rotors rotate in a counter-clockwise manner, whereas the second and the fourth rotors rotate in a clock-wise manner) such that the net torque around the body z axis due to the rotation of propellers is zero during hovering flight.

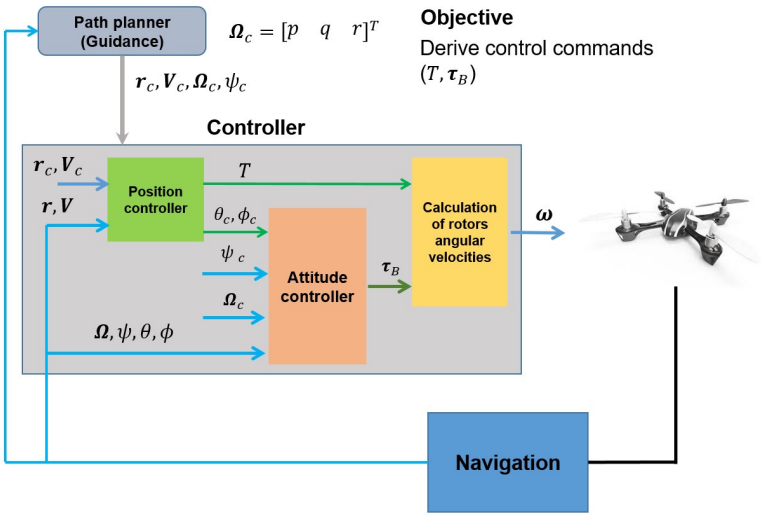

Figure 3.6: Outer/inner control loop scheme for position and attitude control of a quadrotor.

Equations of motion can be derived using the Newton-Euler method that uses the transport theorem [114]. The overall control of the vehicle is achieved through the combination of position control and attitude control. Figure 3.6 depicts a typical outer/inner control loop strategy along with the interconnection of the main components of an algorithm for control

purposes. Let $\mathbf{r} \in \mathbb{R}^3$ and $\mathbf{v} \in \mathbb{R}^3$ denote the position and velocity vectors of the center of mass of the quadrotor, respectively, in the inertial coordinate system, and let $[\phi, \theta, \psi]^T$ denote the orientation angles in a standard (roll-pitch-yaw) 3-2-1 Euler rotation sequence. Let $\Omega = [p, q, r]^T$ denote the components of the angular velocity vector of the body frame relative to the inertial frame when expressed in the body frame - the so-called body rates. Our goal is to derive control commands, namely, thrust control T and control torque τ_{B} to follow a nominal trajectory.

The nominal trajectory is usually generated in an off-line fashion through a path-planner (or guidance algorithm) [28]. The "Navigation" block represents any navigation algorithm. The outputs of the "Path-planner" block are the desired time histories of the states of the system that have to be tracked. In Figure 3.6, the position, velocity, body rates and the heading angle are shown to be the outputs of the guidance block (subscript 'c' is used to specify these values as commanded values that have to be tracked). These values are fed to the "Controller" block. At this stage, the position controller is used to track commanded values of position and velocity, i.e, $\mathbf{r}_{\mathrm{c}}$ and $\mathbf{v}_{\mathrm{c}}$. This task is achieved through a second-order differential error-tracking equation as

$$\ddot{\mathbf{r}}_{\mathrm{e}} + \mathbf{K}_{\mathrm{d}}\dot{\mathbf{r}}_{\mathrm{e}} + \mathbf{K}_{\mathrm{p}}\mathbf{r}_{\mathrm{e}} = \mathbf{0}, \tag{3.12}$$

where $\mathbf{r}_{\mathrm{e}} = \mathbf{r}_{\mathrm{c}} - \mathbf{r}$ denotes the position error and $\mathbf{K}_d$ and $\mathbf{K}_{\mathrm{p}}$ are positive definite gain matrices to ensure acceptable time characteristics of a second-order response. A virtual control vector, $\mathbf{U}$, is now defied as

$$\mathbf{U} = \ddot{\mathbf{r}} = \ddot{\mathbf{r}}_{\mathrm{c}} + \mathbf{K}_{\mathrm{d}}\left(\mathbf{v}_{\mathrm{c}} - \mathbf{v}\right) + \mathbf{K}_{\mathrm{p}}\left(\mathbf{r}_{\mathrm{c}} - \mathbf{r}\right). \tag{3.13}$$

Following Reference [73], this virtual control input can be used along with the translational and rotational equations of motions to compute the desired thrust T, roll angle ϕ_{c}, and pitch angle θ_{c}.Thus, if these three variables are tracked to a good degree of accuracy, one

has essentially realized the position and velocity vectors that are commanded by the path-planning algorithm. The two angles, θ_c and ϕ_c along with the commanded yaw altitude, ψ_c and the commanded body rates Ω_c (computed through a tracking differentiator [73]) constitute the input data to the inner loop (attitude controller).

The goal of the attitude controller is to track the intermediate commanded values (i.e., those that are the outputs of the position controller) and those values that are commanded by the path-planning block. The output of the attitude controller is, therefore, the control torque vector, τ_B, which will result in accurate tracking of Euler angles and body rates. Eventually, the thrust and torque vector are used to compute rotor angular velocity vector $\omega = [\omega_1, \omega_2, \omega_3, \omega_4]^T$. The details of the algorithms can be found in Ref. [73].

3.4 Aerodynamic Models and Coupling to Flight Dynamics

In this section, the coupling of two aerodynamic models, one of which is based on Section III, to the vehicle dynamics is described. Note that the resulting model is intended for fast (real-time or near real-time) trajectory prediction and validation applications.

3.4.1 Simplistic Performance Model

In this approach (also known as the static model), the thrust and torque of the i-th rotor ($i = 1, \ldots, 4$) are modeled as quadratic functions of the rotor RPM for hovering fixed-pitch rotors:

$$Q_i = k\,\omega_i^2, \qquad T_i = b\,\omega_i^2, \tag{3.14}$$

where k and b are referred to as the *effective* torque and thrust coefficients which can be determined experimentally, or using CFD analysis for a given rotor using simple quadratic

curve fitting [69]. Using experimental data shown in Fig. 3.4, these coefficients are estimated to be equal to $b = 1.5652 \times 10^{-8}$ N/RPM^2 and $k = 2.0862 \times 10^{-10}$ Nm/RPM^2.

Given these relations, one can form the following linear system of equations to relate the rotor rotation rate to the required net thrust and torque. Considering Eq. (4.13), and the fact that the sum of the thrust of rotors is the net thrust, one can derive the following relation for the total thrust magnitude and torque inputs:

$$\begin{bmatrix} T \\ \tau_{\mathrm{x}} \\ \tau_{\mathrm{y}} \\ \tau_{\mathrm{z}} \end{bmatrix} = \begin{bmatrix} b & b & b & b \\ 0 & -bl & 0 & bl \\ -bl & 0 & bl & 0 \\ -k & k & -k & k \end{bmatrix} \begin{bmatrix} \omega_1^2 \\ \omega_2^2 \\ \omega_3^2 \\ \omega_4^2 \end{bmatrix}. \tag{3.15}$$

Therefore, by solving Eq. (3.15), one can determine the rotation rate of each rotor. However, it is noted that this model is insensitive to wind conditions as well as the vehicle dynamics.

3.4.2 Radial Inflow Model

The radial inflow model as described in Sec. 3.2 is strictly valid for axial flight. In this work, the incoming wind velocity is projected to the axis of rotor and the thrust is estimated using blade element momentum theory. The benefit of this model - in comparison to the above simplistic model - is its sensitivity to the wind condition and vehicle dynamics. The inputs to this model are the required thrust, and the velocity relative to the body of the quadrotor.

Implementing this model along with the torque model introduces additional complications. First, an inverse problem should be solved, because the desired thrust is now given as an input, and RPM must be computed. At every time instant, this is performed via a simple optimization routine. Second, the yaw torque (τ_{z}) is no longer a function of the RPM, and in fact, is a complex function as described in Eq. (3.10). Thus, the set of equations to solve

for ω_{i} are:

$$T = \sum_{i=1}^{4} T_i(\omega_{\text{i}}), \tag{3.16}$$

$$\tau_{\text{x}} = l(T_4(\omega_4) - T_2(\omega_2)), \tag{3.17}$$

$$\tau_{\text{y}} = l(T_1(\omega_1) - T_3(\omega_3)), \tag{3.18}$$

$$\tau_{\text{z}} = \sum_{i=1}^{4} Q_i(\omega_{\text{i}})(-1)^{i+1}. \tag{3.19}$$

It is clear that, since ω_i are implicit in all of the equations, an analytical solution cannot be found. Note that we need to solve for ω_i ($i = 1, \cdots, 4$) at every time instant along the trajectory, which is a non-linear root-finding problem. One way to provide an approximate solution to these set of equations for every time step is as follows:

- At a given time instant and a given flight condition, for every thrust T_i, solve the inverse problem to find ω_{i} and the resultant Q_{i}.
- For each rotor, use the relations $T_{\text{i}} = b_{\text{i}}\,\omega_{\text{i}}^2$ and $Q_{\text{i}} = k_{\text{i}}\,\omega_{\text{i}}^2$ to estimate the local values of b_i and k_i for that specific rotor and flight condition.
- Use Eq. (3.15), where the coefficient matrix is given by:

$$\begin{bmatrix} b_1 & b_2 & b_3 & b_4 \\ 0 & -b_2 l & 0 & b_4 l \\ -b_1 l & 0 & 0 & b_4 l \\ -k_1 & k_2 & -k_3 & k_4 \end{bmatrix},$$

  to find the final RPMs.
- Calculate the net thrust and torque using newly found RPMs and feed them back into the dynamic model.

It has to be noted that the radial inflow model serves as a template for general aerodynamic module that can be replaced by higher-fidelity models (such as a computational fluid dynamics model).

3.5 Results and Discussion

A quadrotor with the following physical and geometric characteristics is considered: mass, $m = 0.69$ kg, arm length, $l = 0.225$ m, X-moment of inertia, $I_x = 0.0469$ kg m^2, Y-moment of inertia, $I_y = 0.0358$ kg m^2, Z-moment of inertia, $I_z = 0.0673$ kg m^2, rotor moment of inertia, $I_r = 3.357 \times 10^{-5}$ kg m^2.

The aerodynamic models for the quadrotor, and the wind models (Section II) were integrated with the control module in the Simulink environment of MATLAB. We have performed flight simulations for two representative nominal trajectories: 1) an ascent-straight-descent trajectory, 2) a circular trajectory.

3.5.1 Ascent-straight-descent path

Let Δt_i denote the time interval of the i-th segment of a multi-segment trajectory. Figure 3.7 shows the schematic of an idealized rectangular path that consists of five segments: 1) taking off vertically to an altitude of 40 m (where the initial and final vertical velocities are zero) over a time interval of $\Delta t_1 = 10$ seconds, 2) accelerating from zero forward velocity to a cruise constant speed of 15 m/s over a time interval of $\Delta t_2 = 12$ seconds, 3) continuing with the cruise speed for $\Delta t_3 = 30$ seconds, 4) decelerating from a forward velocity of 15 m/s to zero over a time interval of $\Delta t_4 = 15$ seconds, and 5) descending over a time interval of $\Delta t_5 = 10$ seconds. As it follows the trajectory, the quadrotor is subject to the wind field described in Section 3.1. For all segments (except for the cruise segment #3), a cubic polynomial is used to enforce the boundary conditions on x, y and z position and velocity coordinates [115]. For instance, there are four boundary conditions on the translational

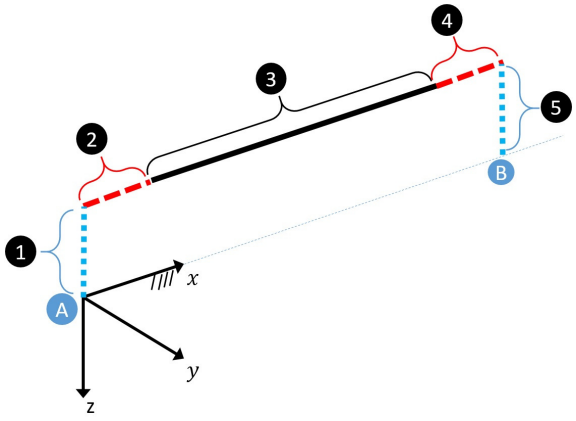

Figure 3.7: Schematic of the ascent-straight-descent nominal trajectory.

velocity of the first segment (*i.e.*, x_i, x_f, $\dot{x}_i$, and $\dot{x}_f$) where subscripts 'i', and 'f' denote the initial and final times of the segment. It is possible to fit a cubic polynomial using the prescribed boundary conditions and solve for the coefficients of the cubic polynomial in terms of the boundary conditions. Velocity and acceleration data of the nominal trajectory are known by taking the first and second time derivatives of the position coordinate. It is noted that the planned trajectory information consists of the planned position, velocities and acceleration, as well as the heading (yaw) angle ($\psi(t) = 0$) all of which are used in the attitude controller block in Fig.3.6. The results for different flight parameters are next presented using a full-wind representation and radial inflow model.

The results demonstrate that the planned trajectory and the vehicle attitude and position are controlled successfully. The time histories of the quadrotor position and velocity coordinates as well as its attitude are shown in Figures 4.32-3.10. All of the resultant flight parameters (shown in color red dashed line) are compared with their planned ones (shown in black sold line). The resultant position versus planned position is shown in Fig. 4.32.

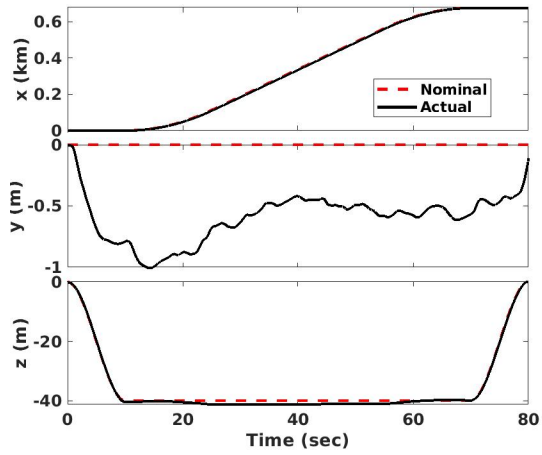

Figure 3.8: Time histories of the inertial coordinates of the trajectory of the quadrotor compared to the nominal trajectory.

As noted, the quadrotor has tracked the planned trajectory with acceptable accuracy. The off-the-track, y position coordinate appears to have the largest deviation due to the side wind effects. The positive x direction of the considered inertial frame points to the east (that is geographic north is in the direction of $(-y)$). In the considered wind model, the wind blows from south west (i.e., from $-x$ to $+x$ and $+y$ to $-y$), and that would push the quadrotor to its left side $(-y)$ and to forward $(+x)$. The planned and resultant velocities in the inertial body frame are shown in Fig. 3.10, which reveals the fluctuations due to turbulent gusts.

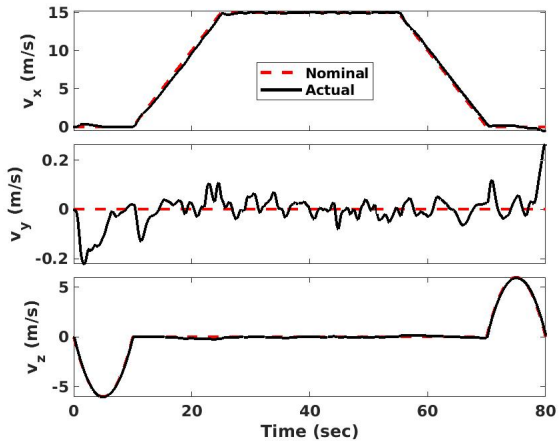

Figure 3.9: Time histories of the inertial velocity component of the trajectory of the quadrotor vs. the nominal velocity.

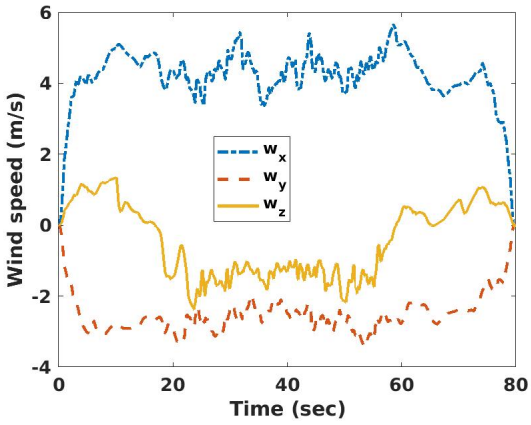

Figure 3.10: Components of the wind velocity along the actual trajectory expressed in the inertial frame.

The wind velocity at the vehicle CG is shown in Fig. 3.10, illustrating a desirable forward wind and an undesirable side wind experienced by the vehicle.

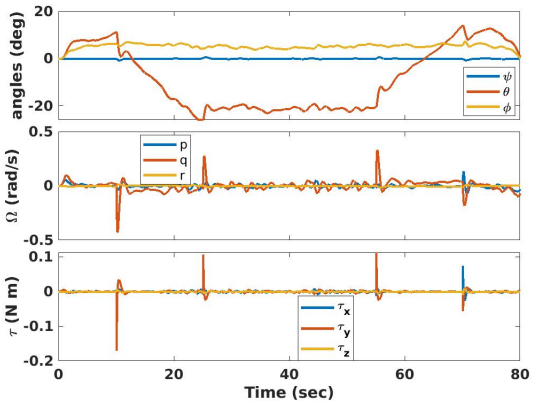

Figure 3.11: Time histories of the Euler angles, body rates and control torques during flight.

The required rotor RPMs to track the planned path are obtained using the radial inflow model and shown in Fig. 3.12.

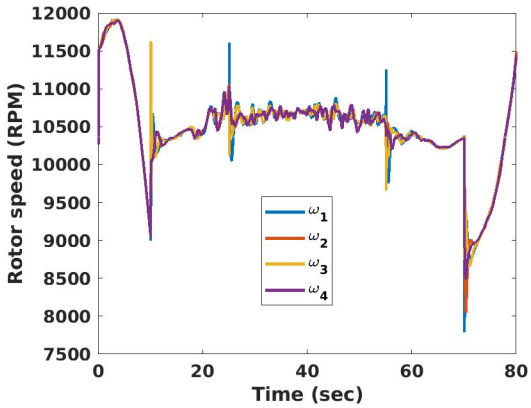

Figure 3.12: Time histories of the rotors' RPM along the trajectory.

The effect of the wind on the resultant trajectory and vehicle dynamics are shown in Figures 3.13 and 3.14. It is noted that without a wind field, the planned path was tracked with almost no deviations. It is also evident that wind effects on the RPM inputs are more prominent in the cruise section compared to the vertical take-off and landing segments.

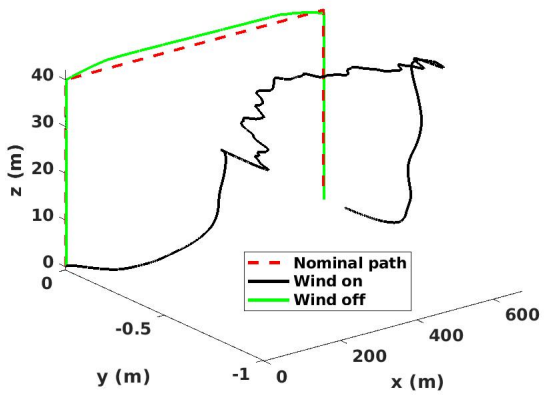

Figure 3.13: Flown trajectories with and without consideration of wind (each axis is scaled differently for clarity).

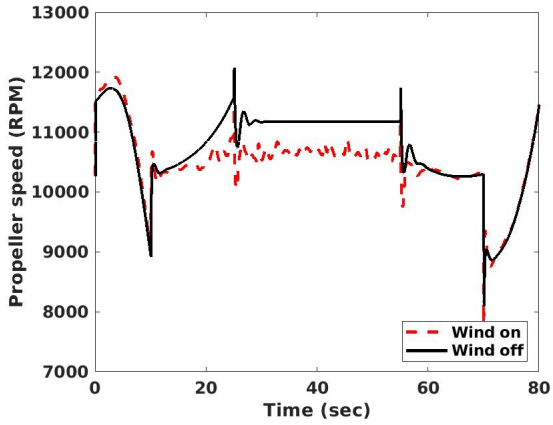

Figure 3.14: Comparison of the rotor #1 RPM with and without consideration of wind.

The difference between the simplified and radial inflow models in terms of the predicted rotor speeds is compared in Fig. 4.36. Note that the resultant RPM of only rotor #1 (leading rotor, see Fig. 3.5) in a no wind condition is presented for clarity in depicting the discrepancy. The predicted RPMs from both models are very similar in axial flight for the hover case as shown in Fig. 3.4 ($t < 10$ s and $t > 70$ s). There is, however, a large discrepancy in the cruise section of the trajectory, ($10 < t < 70$ s) where the velocity relative to the body of the quadrotor increases the inflow λ (see Eq. (3.5)). Therefore, the lift coefficient (Eq. (4.5)) decreases, because Φ increases. Hence, the rotor speed has to increase to maintain the required thrust.

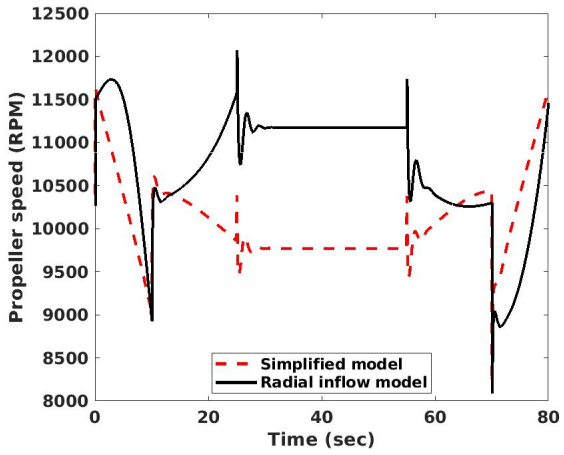

Figure 3.15: Rotor RPM prediction with different models.

The torque and power performance model, introduced in Section 3.2.A, can be used to provide an estimate of the total required power during flight. Considering Eq. (3.9), one can simply write the total power as:

$$P = \sum_{i=1}^{4} C_{\mathrm{P}_i} \rho \pi R^5 \omega_i^3. \tag{3.20}$$

For the simplified model, the power estimate is simply $\sum_{i=1}^{4} k\omega_i^3$ where the value of k is obtained from the torque data of Fig. 3.4. The time history of the power estimated by both models is shown in Fig. 3.16.

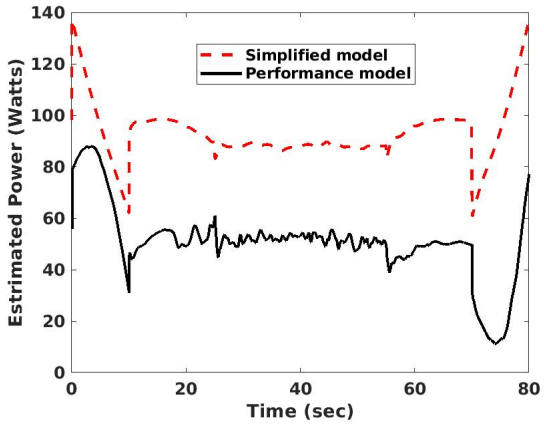

Figure 3.16: Time histories of the required power estimates using different models.

The simplified model yields larger power values and this is mainly due to the offset seen between the torque predictions of performance model and experimental data in Fig. 3.4. It is also apparent that take-off ($t < 10$ s) requires more power than landing ($t > 70$ s). The radial inflow model represents this effect, while the simplified model is unable to do this.

To assess the importance of the wind model, the wind field is reconstructed using different number of modes, and flight simulations are performed to illustrate the impact on the results. A comparison between the resultant trajectories of the full wind, reduced-order versions of the wind field, and the Dryden Wind Turbulence model is shown in Fig. 3.17.

In these simulations, the radial inflow model was used as the aerodynamic model to compare the impact of the different wind models. While the controller attempts to keep the quadrotor on the nominal path regardless of the wind model used, it is clear that the Dryden model - as a consequence of the fact that the fluctuations are not spatio-temporally correlated - results in a lesser deviation from the nominal trajectory.

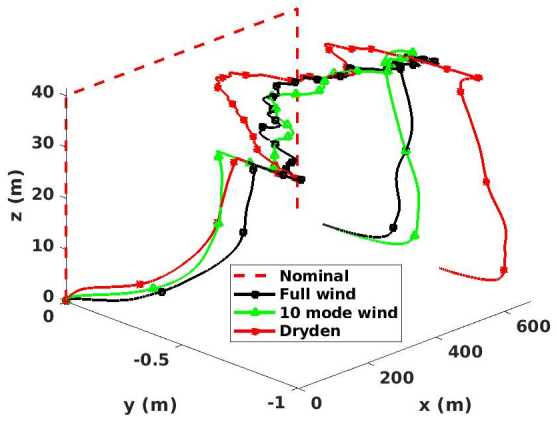

Figure 3.17: Effect of different versions of wind model on the resultant trajectory.

The incoming velocities in the three directions seen by the quadrotor for different wind models are shown as a function of time in Fig. 3.18.

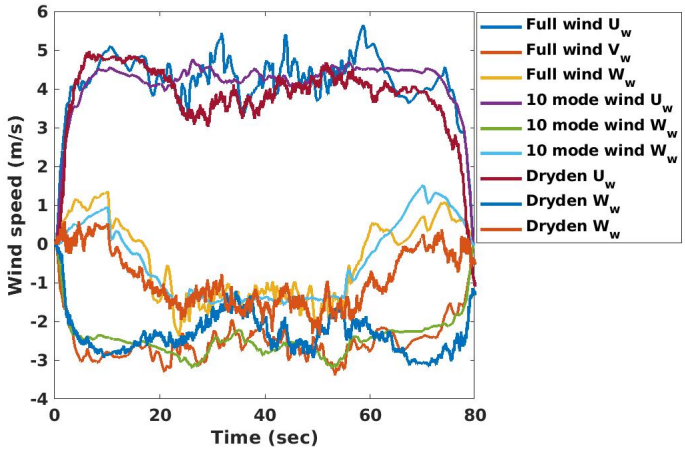

Figure 3.18: Wind velocity components in the inertial frame.

3.5.2 Circular Path

Flying in a circular path further accentuates the importance of the flight controller and wind model. In this case, the quadrotor has to follow a path with continuous acceleration. The presence of wind has both favourable and unfavourable effects during portions of the trajectory, as discussed herein. A schematic of the circular path and the wind condition is shown in Fig.3.19.

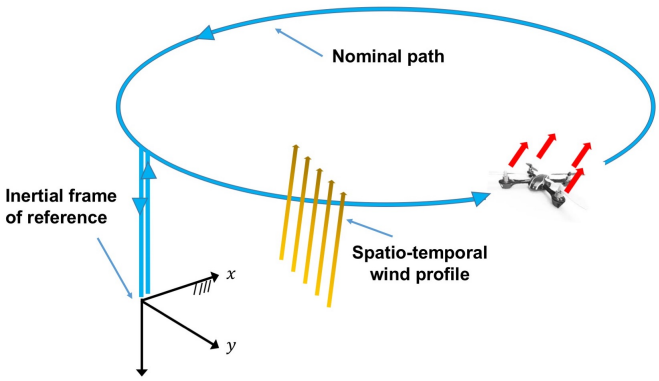

Figure 3.19: Schematic of the circular path.

Similar to the straight path, the trajectory for the circular path consists of five segments: 1) taking off to an altitude of 60 m, 2) accelerating for 10 seconds to a nominal speed while being in the circular path with radius of 80 m, 3) following the circular path with a nominal speed, 4) decelerating for 10 seconds to stop at the point where the circular path was initially started, and 5) landing.

A comparison between the planned and obtained location and velocity in the three directions is shown in Figs. 3.20 and 3.21. The results are indicative of the fact the vehicle has been able to track the planned path well and maintain the quadrotor on the nominal path.

The wind velocity at the center of mass of the quadrotor is shown in Fig. 3.22. The values are slightly larger compared to the straight path (see Fig. 3.10) given that the circular path has a higher altitude.

For this path, the commanded heading angle (ψ_c) was set to zero which means the

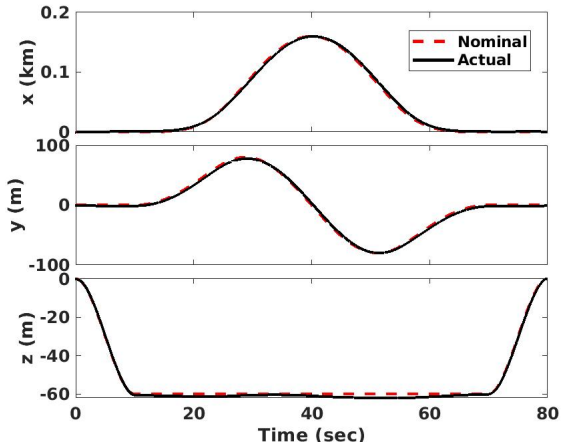

Figure 3.20: Time histories of the position coordinates of the center of mass of the quadrotor for circular path.

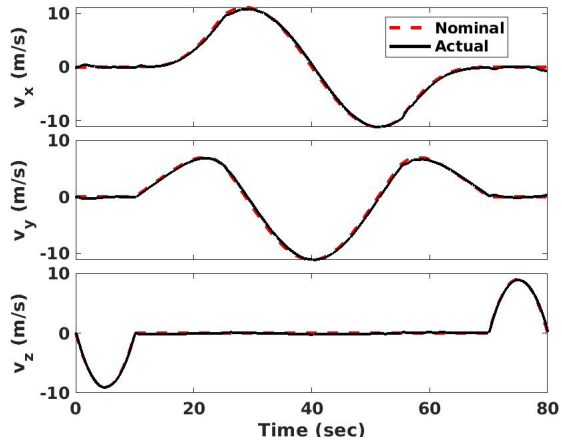

Figure 3.21: Time histories of velocity coordinates of the center of mass of the quadrotor for circular path.

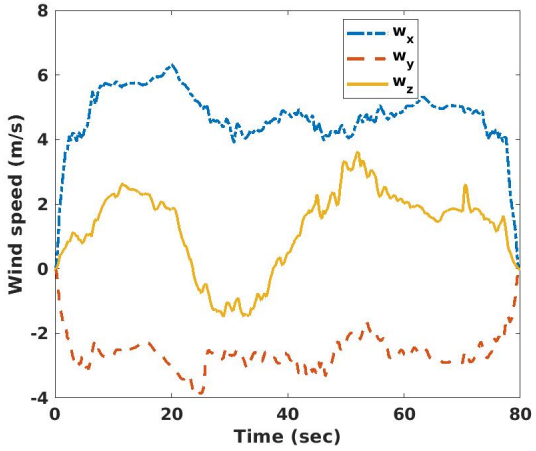

Figure 3.22: The wind velocity at the center of mass of the quadrotor.

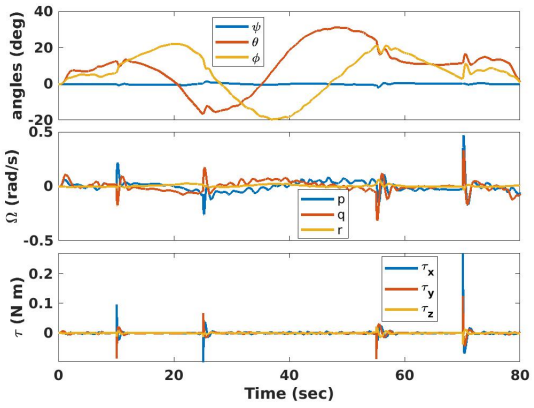

Figure 3.23: Euler angles (roll, pitch and yaw), body rates, and torques applied to the quadrotor during circular path.

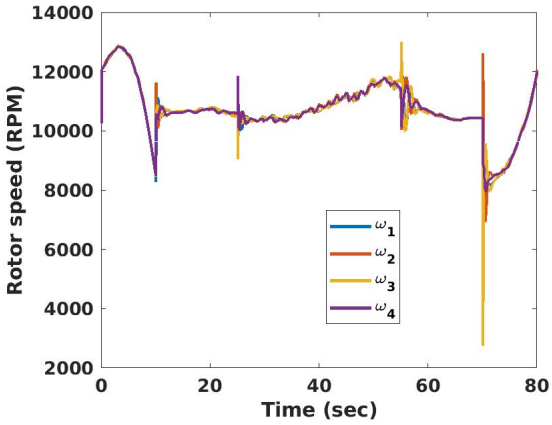

Figure 3.24: Rotor speeds to maintain the quadrotor on the circular path.

quadrotor does not turn around its Z-axis, and the circular path was tracked by controlling only roll and pitch angles. The Euler angles, and their rated and resultant torques are depicted in Fig. 3.23.

As noted from Fig. 3.23, for the take-off phase ($t < 10$ s), the quadrotor has to roll (right rotor (#3) down), and pitch up (front rotor (#1) up) to negate the incoming wind from the south west, and then continue the entire path with a nose up position to negate the effect of the wind. The corresponding four rotor speeds shown in Fig. 3.24 were obtained as the controller commands computed to maintain the planned circular trajectory.

The actual versus the planned trajectories are demonstrated for the circular path in Fig. 3.25. As expected, the actual trajectory is shifted toward positive x and negative y

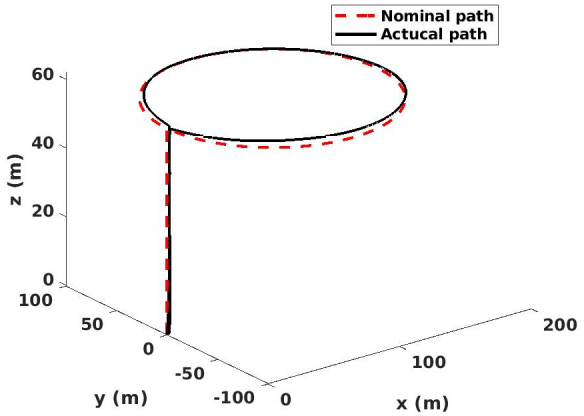

Figure 3.25: The actual versus the planned trajectories for the circular path.

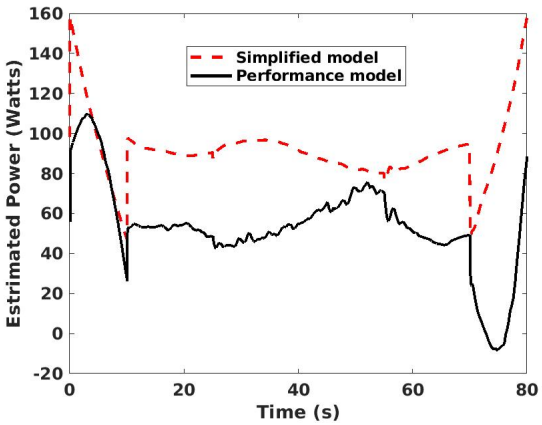

Figure 3.26: Estimated required power through different models for circular path.

due to the wind condition. A maximum deviation of 2 meters between the two paths is noted. The estimates of the required power obtained from the simplified and radial inflow models are shown in Fig. 3.26.

When the quadrotor is on the circular trajectory ($10 < t < 70$ s), the simplified model shows a higher sensitivity to the favorable and adverse wind conditions. In the first half circle ($10 < t < 40$ s), the wind is overall favorable. In the second half circle ($40 < t < 70$ s), the wind causes unfavorable drag as well as more induced inflow to the rotors that leads to higher RPMs (see Fig. 3.24), and subsequently, higher power as depicted in Fig. 3.26.

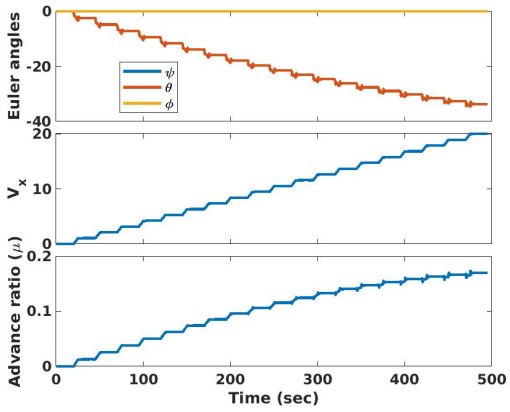

Figure 3.27: Euler angles and cruise speed for optimal cruise speed determination.

3.5.3 Optimal Cruise Speed

The relationship between power and cruise speed is non-monotone and non-linear. The power model (see Eq. (3.9)) can be further analyzed to determine the optimal cruise speed and compared with the power required in hover. A new trajectory was defined, in which the quadrotor starts from hover, and the forward speed is adjusted incrementally on a straight path. Within each increment, it accelerates for 5 seconds to add 1 m/s to its speed during the acceleration phase, and stays on that specific cruise speed for 20 seconds. This increment is performed 20 times, and the vehicle will eventually reach a forward speed of 20 m/s in a total time of 500 seconds. The Euler angles and forward velocity in the inertial reference frame, and advance ratio are shown in Fig. 3.27.

It is noted that the advance ratio, μ, is relatively small for the entire flight. At the highest forward speed of 20 m/s, the advance ratio is $\mu = 0.17$. The pitch angle increases in magnitude during the acceleration phase and maintains the same level during the constant cruise speed part of each increment. The speed of the quadrotor as a function of the leading rotor #1 (see Fig. 3.5) rotational speed is shown in Fig. 3.28.

As noted from Fig. 3.28, the power curve with the performance model (see Eq. (3.9)) has a local minimum around $V_{\text{x}} = 7.2$ m/s (indicated with the green dashed line). It is also noted that the simplified model that only uses the rotor speed to estimate the power

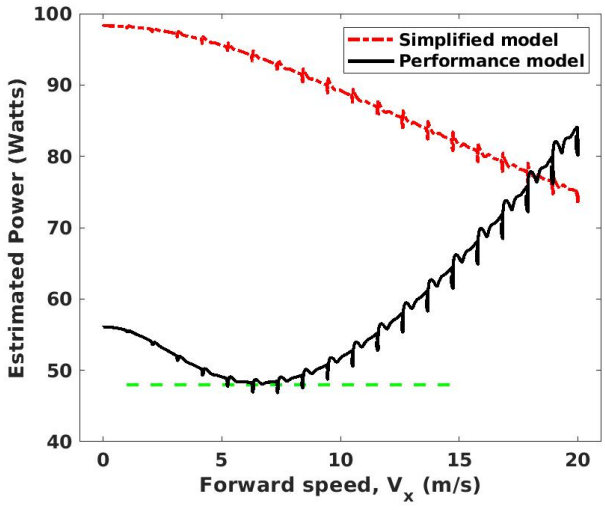

Figure 3.28: Estimated required power versus cruise speed for simplified and radial inflow models.

($P = k\sum_{i=1}^{4}\omega_i^3$) estimates less power consumption for higher speeds. This is due to the fact that at higher speeds, the drag (see Eq. (3.11)) provides an upward component when the pitch angle is negative ($\theta < 0$), thus augmenting thrust. Therefore, the thrust required by the rotor (to sustain the altitude) decreases and based on the simplified model, the required RPM should also decrease. The estimated RPM values of rotor #1 versus forward speed from both models are shown in Fig. 3.29.

As expected, the two models show opposite trends. Based on Figs. 3.28 and 3.29, higher RPM does not necessarily indicate higher required power, as the flight condition has a significant impact on the total power.

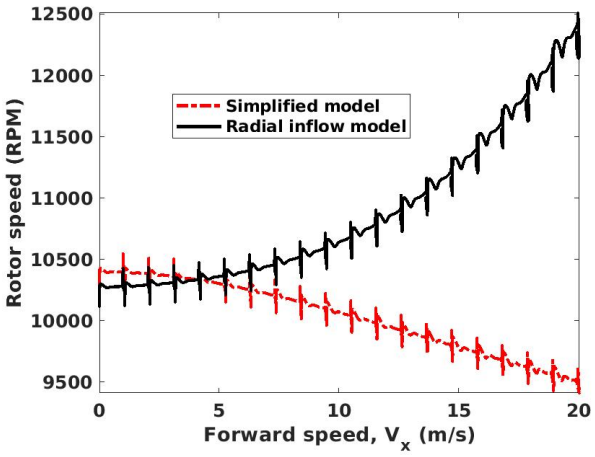

Figure 3.29: Estimated rotor #1 speed as a function of cruise speed.

CHAPTER 4

Hybrid Blade Element Momentum (HBEM) Model for Forward Flight : Formulation and Experimental Validation

Rotary wing unmanned aerial vehicles are being relied upon for increasingly versatile missions that involve a wide range of flight regimes. Efficient predictive models that are reliable across diverse flight regimes have remained elusive, but are especially critical for applications such as trajectory planning and autonomous operations. This chapter presents a new aerodynamic model to predict the forces and moments generated by a rotor in vertical and forward flight. The model is self-contained and consistently combines Blade Element and Momentum theories with a linear inflow model, and can be executed in near-real time.

The HBEM model utilizes the blade geometry and the flight condition as inputs and can determine the relationship between the forces/moments and rotor RPM condition. A detailed set of wind tunnel experiments were conducted to validate the proposed model across a very wide range of flight regimes. Following the validation, the model is integrated in a 6 DoF flight dynamics and control module, and flight simulation for a ascent-cruise-descend path is performed. The source codes for the proposed aerodynamic model and flight simulation module are open sourced for use by the community.

Another force that is applied to the rotor in forward flight is rotor in-plane force (RIPF). The RIPF was quantified in the wind tunnel experiments, and using an optimization tech-

nique a symbolic data-driven model (RIPF model) was constructed. The RIPF model predict the in-plane force that also has a contribution to the overall drag of the quadrotor.

4.1 HBEM Model Formulation

For rotors in hover and axial flight, momentum theory assumes the rotor to be an actuator disk embedded within a stream tube of the flow. By enforcing mass and momentum conservation, a simple relationship is derived between the thrust and the uniform inflow velocity. In case of propellers, errors associated with momentum theory was evaluated in [116]. To take into account the blade geometry, blade element momentum theory considers conservation equations over annular sections of the stream tube to derive an analytical expression for thrust given the inflow distribution across the rotor disk . In forward flight, the definition of a stream tube is less straightforward. Further, the coupling between momentum and blade element theories becomes complicated, as the inflow is non-uniform across the rotor azimuth, and the incoming velocity to each blade section is different for every radial location (r) and azimuth angle (Ψ).

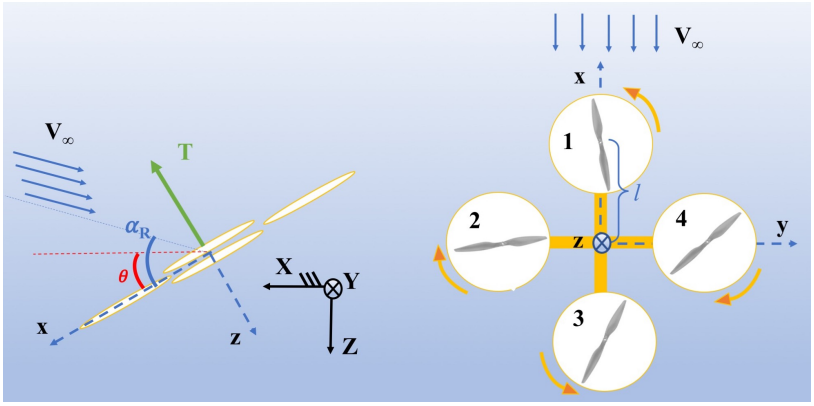

Figure 4.1: Schematic of a quad-copter (4 rotors shown): top (on the right side) and side (on the left side) views. Rotor angles of attack α_R versus Euler pitch angle θ are shown in the side view.

Rotor performance analysis using momentum theory was first developed by Glauert [117, 118] for forward flight. Consider a stream tube passing through a rotor in forward

flight. By employing conservation of mass and momentum in the direction perpendicular to rotor disk and by the application of conservation of energy, thrust can be related to the incoming velocity (V_∞), rotor angle of attack (α_R) and inflow velocity across the rotor disk (see Fig. 4.1). The net velocity across the rotor disk in forward flight is a contribution by the incoming velocity and rotor suction. The former does not exist in hover. In a general non-dimensionalized form, the relationship between the uniform inflow ratio and the thrust coefficient C_T is:

$$\lambda_0 = \lambda_\mathrm{c} + \frac{C_\mathrm{T}}{2\sqrt{\mu^2 + \lambda_0^2}}, \tag{4.1}$$

where λ_c is the climb ratio perpendicular to rotor plane, and is completely specified by the flight condition. Also, advance ratio μ parallel to rotor plane can be defined as:

$$\begin{aligned} \mu &= \frac{\sqrt{V_{\mathrm{rel}_{\mathrm{B}_x}}^2 + V_{\mathrm{rel}_{\mathrm{B}_y}}^2}}{V_\mathrm{tip}}, \\ \lambda_\mathrm{c} &= \frac{V_{\mathrm{rel}_{\mathrm{B}_z}}}{V_\mathrm{tip}}, \end{aligned} \tag{4.2}$$

where, $V_{\mathrm{rel}_{\mathrm{B}_x}}$,$V_{\mathrm{rel}_{\mathrm{B}_y}}$ and $V_{\mathrm{rel}_{\mathrm{B}_z}}$ are the velocities in the x,y, and z directions of the aerial vehicle represented in the body frame (see Fig. 4.1), and λ_0 is the uniform inflow ratio which is the total velocity passing through the disk non-dimensionalized by the rotor tip velocity (V_tip). A Newton-Raphson iterative method can be used [48] to determine λ_0 (when λ_c and C_T are known). The initial guess for λ_0 is often $\lambda_\mathrm{h} = \sqrt{C_\mathrm{T}/2}$ which is the inflow ratio in hover.

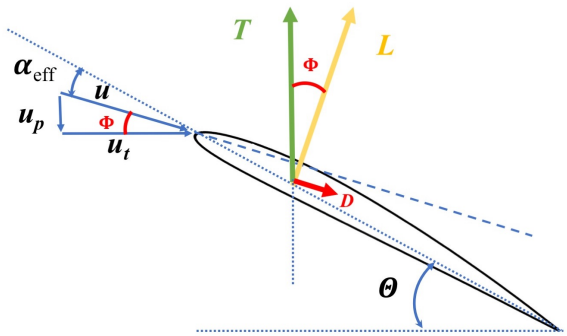

Figure 4.2: Flow geometry associated with each airfoil section.

In blade element theory, individual airfoil sections are considered as shown in Fig. 4.2. The radial, tangential and perpendicular velocities – which are functions of radial location (r) and azimuth angle (Ψ) – can be non-dimensionalized by the blade tip velocity and are given by:

$$\begin{aligned} u_{\mathrm{r}} &= \mu \cos(\Psi), \\ u_{\mathrm{t}} &= r + \mu \sin(\Psi), \\ u_{\mathrm{p}} &= \lambda + \mu\beta \cos(\Psi) + r\dot{\beta}/\omega, \end{aligned} \tag{4.3}$$

where β is the flapping angle and can be neglected for rigid rotors. The radial velocity is often neglected in analytical approaches, as its contribution does not affect the aerodynamic properties, as long as flow separation is not present. The resultant *effective* velocity incident on a blade can then be evaluated as $u = \sqrt{u_{\mathrm{p}}^2 + u_{\mathrm{t}}^2}$.

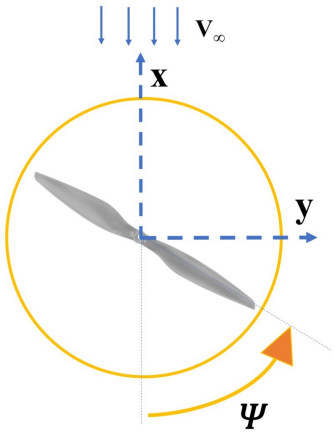

Figure 4.3: Definition of azimuth angle Ψ and coordinate system for an individual rotor.

The outstanding question is how to determine the inflow ratio (λ) distribution across the disk in terms of the radius and azimuth. The impact of different inflow models including uniform, linear and Peters-He [62] generalized dynamic wake model inflow models on the aeromechanics of a quadrotor in hover and forward flight was studied in Ref. [63]. Experiments have been performed to determine the inflow velocity distribution across the rotor disk [64]. It has been demonstrated that the time-averaged distribution can be approximated using a linear approximation from front-to-aft and side-to-side.

In this work, a linear model first suggested by Ref. [119] is adopted:

$$\lambda = \lambda_0(1 + k_x r\cos\Psi + k_y r\sin\Psi). \tag{4.4}$$

Multiple attempts have been undertaken to quantify k_x and k_y [120, 121, 122, 123, 124]. For instance, $k_x = 4/3(1-\cos(\chi)-1.8\mu^2)/\sin(\chi)$ and $k_y = -2\mu$ suggested by [121]. In this work, $k_x = (15\pi/23)\tan(\chi/2)$ and $k_y = 0$, obtained in Ref. [124], is used. The wake skew angle is given by $\chi = \tan^{-1}(\mu/\lambda_0)$.

It is noted that λ_0 is the uniform inflow ratio obtained by momentum theory in forward flight (see Eq. (4.1)). This is the link that connects both theories. If λ_0 were known, the sectional lift coefficient could be calculated using Eq. (4.5),

$$C_{\mathrm{l}} = C_{\mathrm{l}_\alpha} \alpha_{\mathrm{eff}}, \tag{4.5}$$

where the effective angle of attack is $\alpha_{\mathrm{eff}} = (\Theta + \alpha_{L=0} - \Phi)$. The inflow angle $\Phi = \tan^{-1}(u_{\mathrm{p}}/u_{\mathrm{t}})$ as shown in Fig. 4.2. The blade twist angle is denoted by Θ , and $\alpha_{L=0}$ is the absolute value of the zero-lift angle of attack. It is noted that $\lambda = \lambda(r, \Psi)$. To represent the sectional lift when the effective angle of attack is high, the post-stall model presented in Eq. 3.4 can be used.

The next step is to determine the total thrust by integrating the lift distribution and projecting it on the rotor axis using the following expression:

$$T = \frac{RN_{\mathrm{b}}}{2\pi} \int_{r_{\mathrm{min}}}^{1} \int_{0}^{2\pi} \frac{1}{2} \rho (u V_{\mathrm{tip}})^2 c(r) \left[C_{\mathrm{l}} \cos(\Phi) - C_{\mathrm{d}} \sin(\Phi) \right] \, d\Psi dr. \tag{4.6}$$

Note that "$C_{\mathrm{d}} \sin(\Phi)$" term in Eq. (4.6) can be neglected relative to "$C_{\mathrm{l}} \cos(\Phi)$". r_{min} is the minimum normalized radius where the blade generates aerodynamic forces. For the propeller used in this work, $r_{\mathrm{min}} = 0.2$. The thrust coefficient is:

$$C_{\mathrm{T}} = \frac{N_{\mathrm{b}}}{4R\pi^2} \int_{r_{\mathrm{min}}}^{1} \int_{0}^{2\pi} C_{\mathrm{l}} \, u^2 c(r) \cos(\Phi) \, d\Psi dr, \tag{4.7}$$

where $c(r)$, N_{b}, ρ are chord length at radial location r, number of blades and air density respectively. Also, C_{l} is computed using Eq. (3.4).

Thus far, two distinct theories have been examined for forward flight, between which the uniform inflow ratio (λ_0) is common. Momentum theory assumes the thrust coefficient as an input and blade element theory calculates the thrust coefficient as an output. On careful examination of both theories, it is apparent that the thrust coefficients as a function of the inflow ratio have opposite trends. In momentum theory, a larger thrust coefficient results in a larger inflow ratio; however, in the blade element theory, a larger inflow ratio leads to a smaller effective angle of attack (i.e., larger inflow angle), and consequently a

lower thrust coefficient.

This discrepancy is a result of the fact that the thrust coefficient and inflow ratio cannot be changed independently. Thus, we seek a candidate set of $\{\lambda_0, C_\mathrm{T}\}$ that satisfies both theories. To illustrate this, the relationship between thrust and inflow ratio is shown for both theories in Fig. 4.4 by assuming some typical values for climb and advance ratios ($\lambda_\mathrm{c} = 0.1$ and $\mu = 0.2$).

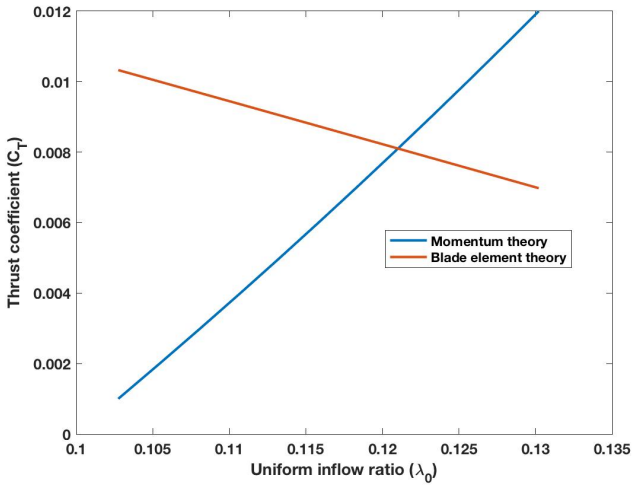

Figure 4.4: Comparison between momentum and blade element theories for $\lambda_\mathrm{c} = 0.1$ and $\mu = 0.2$.

Given the existence of a target point for which both theories agree, one can use the target thrust and determine the angular velocity ($\omega = V_\mathrm{tip}/R$). However, it is noted that the values for advance ratio μ and climb ratio λ_c will also change with the newly obtained angular velocity with respect to their initial values. An algorithm to find the angular velocity is shown in Algorithm 1:

Algorithm 1 Algorithm to determine angular velocity in forward flight given thrust.

Input: thrust T, V_{rel_B};
Output: angular velocity ω
Steps:

1. An initial guess for angular velocity (ω)
2. Calculate advance and climb ratio (μ and λ_c) given flight condition
3. Find uniform inflow ratio λ_0 from momentum theory
4. Use λ_0 to compute thrust coefficient from momentum theory ($C_{\text{T}_\text{Momentum}}$)
5. Use λ_0 to compute thrust coefficient from blade element theory (C_{T_BET})
6. Define $|C_{\text{T}_\text{Momentum}} - C_{\text{T}_\text{BET}}|$ as an objective function to minimize
7. update/change the angular velocity ω, go to "Step 2" until convergence

There are also situations in which one has to determine the thrust provided by a rotor operating at a known angular velocity and flight condition (μ, λ_c). This is shown in Algorithm 2.

Algorithm 2 Algorithm to determine thrust in forward flight given angular velocity.

Input: angular velocity ω, V_{rel_B};
Output: thrust T
Steps:

1. An initial guess for thrust (T) is made
2. Calculate thrust coefficient ($C_{\text{T}_\text{Momentum}}$)
3. Calculate the exact advance and climb ratio (μ and λ_c) given flight condition
4. Find uniform inflow ratio λ_0 from momentum theory
5. Use λ_0 to compute thrust coefficient from blade element theory (C_{T_BET})
6. Define $|C_{\text{T}_\text{Momentum}} - C_{\text{T}_\text{BET}}|$ as an objective function to minimize
7. Update/change the thrust T, go to "Step 2" until convergence

Once the optimization problem is solved, moments can be calculated for a fixed pitch

rotor. A schematic of the rotor and coordinate system in the body frame is shown in Fig. 4.3. The imbalance of loads between the advancing and retreating sides will cause a negative rolling moment (moment vector points towards -x direction). The roll (x-direction) and pitch (y-direction) moments are given by:

$$
\begin{aligned}
C_{\mathrm{r}} &= \frac{N_{\mathrm{b}}}{4R^2\pi^2}\int_{r_{\mathrm{min}}}^{1}\int_{0}^{2\pi} -yC_{\mathrm{l}}u^2c(r)\cos(\Phi)\,d\Psi dr, \\
C_{\mathrm{p}} &= \frac{N_{\mathrm{b}}}{4R^2\pi^2}\int_{r_{\mathrm{min}}}^{1}\int_{0}^{2\pi} xC_{\mathrm{l}}u^2c(r)\cos(\Phi)\,d\Psi dr,
\end{aligned}
\tag{4.8}
$$

where $x(r,\Psi) = -rR\cos(\Psi)$ and $y(r,\Psi) = rR\sin(\Psi)$. It is noted that "r" is normalized, and we need to multiply "x" and "y" by the blade radius R.

As an example, the contour plot of the lift coefficient across the disk is shown in Fig. 4.5 for a sample flight configuration. The lift coefficient (Eq. (4.5)) distribution across the rotor plane leads to positive pitch and negative roll moments. Also, a reverse flow region in the vicinity of the hub on the "$-y$" side of rotor is observed where negative lift is generated. It is noted that differential thrust distributions will be different from the lift coefficient distribution (Eq. (4.6)).

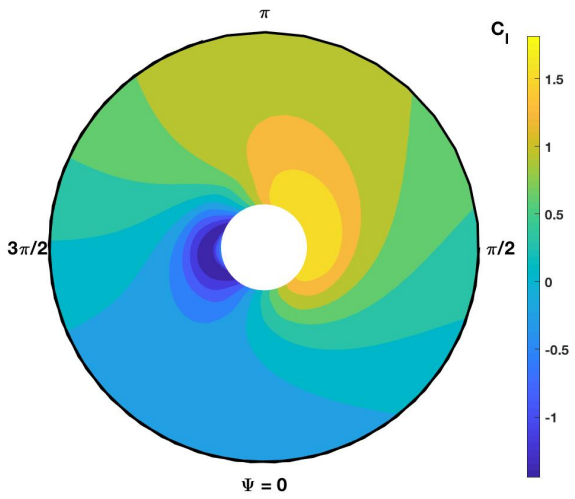

Figure 4.5: Lift coefficient (C_{l}) across the rotor plane for $V_\infty = 15$ m/s and $\alpha_{\mathrm{R}} = 40^\circ$ ($\mu = 0.15$).

To recap, a few comments are made on the novelty of HBEM model. The HBEM model is developed by combining well-established theories; namely momentum and blade element theories in forward flight. It uses a linear inflow model across the rotor disc. The solution to the HBEM model is unique and occurs where the two aforementioned theories agree. The solution is obtained through a low-cost optimization solver and the model can be executed well above 200 times per second in a typical compute module board (see Section 5.1). The HBEM model is self-contained and self-consistent and only uses blade geometry and flight condition as inputs, and this makes it a powerful aeromechanical tool to estimate thrust and moments given an RPM condition, or similarly it can find the required RPM condition given a desired thrust value.

It is noted that the HBEM model has some limitations: This model is derived based on steady state assumptions, and it can only be executed as a quasi-steady model. Therefore, in conditions where the relative incoming wind changes rapidly or when the rotor diameter and chord are large (aerodynamic response to the inflow changes has a larger delay), the HBEM model will not be accurate. In this case, a dynamic inflow model (e.g. [125]) will be more appropriate. The HBEM model is developed for fixed-pitch rotors, and thus it cannot represent variable-pitch rotors. Also, further analysis and experiments are needed to validate the rotor moments estimated by the HBEM model.

4.2 Experimental Setup and Analysis

A detailed set of experiments were conducted to measure the aerodynamic forces generated by a propeller over a wide range of vertical and forward flight conditions. Similar experiments were conducted in Ref. [126] to determine the relation between thrust and α_{R}. A propeller (*APC 8×4.5MR*) [1] with a diameter of 8 in is selected for detailed investigations. The chord and twist angle distributions for this propeller as a function of span are shown in

[1] `https://www.apcprop.com/`

Fig.4.6.

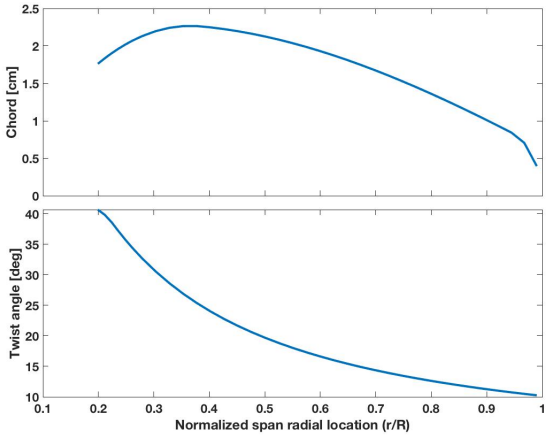

Figure 4.6: Chord and twist distributions as a function of span for "APC 8x4.5MR".

The cross section airfoil of the blade is slightly cambered and is not symmetric. We are interested in the 2D aerodynamic properties of the airfoil. The highest Reynolds number ($Re = Vc/\nu$) is less than 10^5 for the entire blade span and azimuth angle range. $1.8\ \pi$ was chosen as the lift curve slope (C_{l_α}) and 2° as the zero-lift angle of attack ($\alpha_{L=0}$). The parameters, transition rate cut-off angle, used in Eq.(3.4) were selected as $M = 50$ and $\alpha_0 = 20^\circ$ [72].

As shown in Fig. 4.7, an optic RPM sensor is mounted near the body of the brushless motor. Two pieces of reflecting tape were attached to the body of the motor. The RPM optic sensor sends a voltage every time a reflecting tape passes by. Therefore, the number revolutions (N) can be tracked per unit time (t) (from the recorded signal). This information can be converted to angular velocity as $\omega = dN/dt$.

For every experiment, data was acquired for a span of 10 seconds at a rate of approximately 200 Hz. A BeagleBone Blue board [127] was used in the setup, and embedded software is used to send the PWM signal command to the speed controller and eventually to the motor.

The propeller setup is mounted in a 2×2 ft wind tunnel at the University of Michigan, and the experimental setup is shown in Fig.4.7. Force measurements are obtained using

three force transducers mounted on a force balance located outside the wind tunnel. The forces on the propeller are transferred through a rod to the first force balance outside the tunnel. Force transducer $\#1$ was mounted in the stream-wise direction, and the other two ($\#2$ and $\#3$) are in the span-wise directions. A schematic of aerodynamic forces, and the force balance configuration is shown in Fig.4.8.

The force balances were properly calibrated by applying known weights and measuring voltage outputs from the force transducers. The calibration gains and offsets (12 unknowns total) were obtained using multi-variate linear regression.

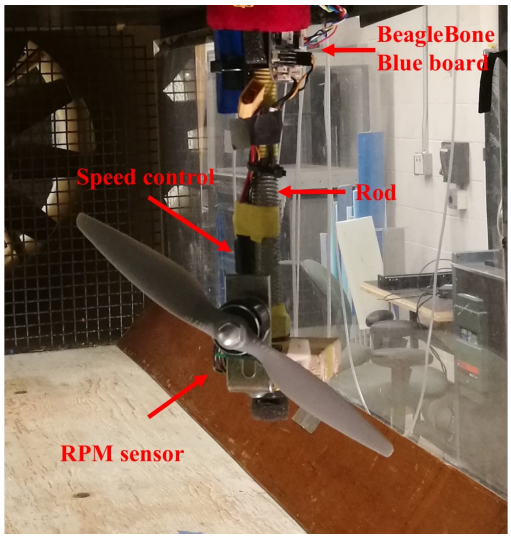

Figure 4.7: Experimental setup showing rotor at angle of attack of $\alpha_R = 40^o$.

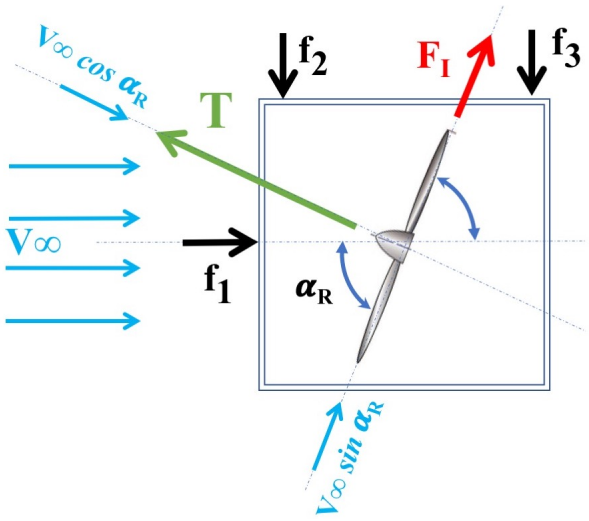

Figure 4.8: Components of the wind velocity and forces.

Force equilibrium in the propeller body frame coordinate yields:

$$\begin{aligned} \sum F_{\mathrm{x}} &= T \sin \alpha_{\mathrm{R}} - f_1 - F_{\mathrm{I}} \cos \alpha_{\mathrm{R}} = 0, \\ \sum F_{\mathrm{y}} &= T \cos \alpha_{\mathrm{R}} + F_{\mathrm{I}} \sin \alpha_{\mathrm{R}} - f_2 - f_3 = 0. \end{aligned} \tag{4.9}$$

Therefore, thrust and in-plane force (F_{I}) can be extracted from the measured forces (f_{i}):

$$\begin{aligned} T &= f_1 \sin \alpha_{\mathrm{R}} + (f_2 + f_3) \cos \alpha_{\mathrm{R}}, \\ F_{\mathrm{I}} &= (f_2 + f_3) \sin \alpha_{\mathrm{R}} - f_1 \cos \alpha_{\mathrm{R}}. \end{aligned} \tag{4.10}$$

It is noted that, when the rotor angle of attack is $\alpha_{\mathrm{R}} = 90^\circ$, i.e. in axial flight, the in-plane force (F_{I}) is zero and thrust is simply obtained as $T = f_1$. Other important parameters such as advance ratio and climb ratio can be similarly defined as: $\mu = V_\infty \cos \alpha_{\mathrm{R}} / V_{\mathrm{tip}}$ and $\lambda_{\mathrm{c}} = V_\infty \sin \alpha_{\mathrm{R}} / V_{\mathrm{tip}}$ for the wind tunnel test.

To validate the proposed model in forward flight, four sets of data were acquired for four distinct wind tunnel speeds, $V_\infty = 0, 5, 10$ and $15 m/s$. In every set of data (except

$V_\infty = 0$ m/s), the rotor angle of attack was varied from $\alpha_\mathrm{R} = 0^\circ$ to $\alpha_\mathrm{R} = 90^\circ$, see Fig. 4.8. For every rotor angle of attack, the rotation speed was altered by sending a range of throttle command inputs from minimum to maximum: $[0, 0.2, 0.3, 0.4, 0.5, 0.6, 0.7, 0.8, 0.9]$. It is noted that the maximum RPM is bounded by the capability of the electromotor used in the experiment.

4.2.1 Experimental Errors

Experiments were first conducted with no propeller mounted on the motor to determine the forces due to the experimental setup. Careful calibration was carried out before and after each run, to take into account any voltage drifts in the force transducers. For every rotor angle of attack (α_R), a zero-throttle motor input case was obtained as the reference. The rotor angle of attack is varied from 90° (propeller axis in the stream-wise direction) to 0° (propeller axis in the span-wise direction).

4.2.1.1 Ground Effect

When the propeller angle of attack is low, the side wall of the wind tunnel can block the flow down-stream of the propeller. This "ground effect" will add to the thrust [128, 129] compared to the same operating condition away from the ground. Therefore, it is speculated that for isolated rotors, the thrust will be smaller than the measured values from these experiments, at lower rotor angles. The thrust due to ground effect, denoted by T_g can be roughly estimated [130] as

$$\frac{T_\mathrm{g}}{T_\infty} = \frac{1}{1 - \frac{1}{16}(\frac{R}{Z})^2 \left\{ \frac{1}{1+(\frac{\mu}{\lambda_0 - \lambda_\mathrm{c}})^2} \right\}}, \tag{4.11}$$

where Z is the ground clearance, and T_∞ is the thrust away from ground. It is noted that R/Z ratio is approximately $1/3$ in the wind tunnel experiment. Therefore, the thrust increase due to ground effect is estimated at 2% at maximum.

4.2.1.2 Impact of Flow disturbances

A rotor in forward flight encounters a variety of flow conditions including reverse flow on the retreating blade (Fig. 4.5) and turbulence. At high forward speeds, these flow disturbances lead to vibration. Additionally, the flow around the experimental setup (see Fig. 4.7) causes unsteadiness in force measurements. For $\alpha_{\mathrm{R}} = 0°, 30°, 60°$ and $80°$, the Root Mean Squared (RMS) of the thrust fluctuations are shown as error bars for every thrust value (as a function of advance ratio) for different free-stream speeds in Fig. 4.9- 4.11.

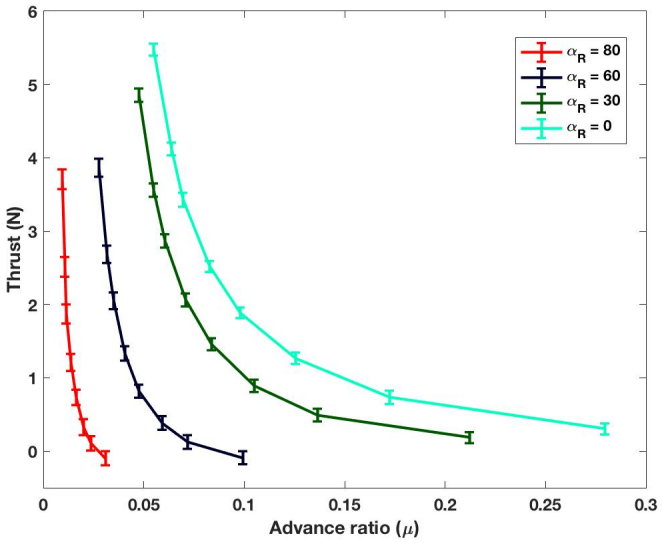

Figure 4.9: Uncertainty in thrust for $V_\infty = 5$ m/s.

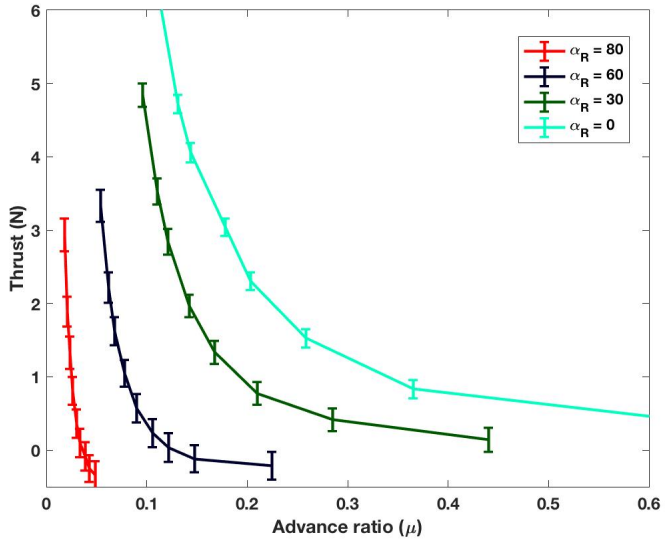

Figure 4.10: Uncertainty in thrust for $V_\infty = 10$ m/s.

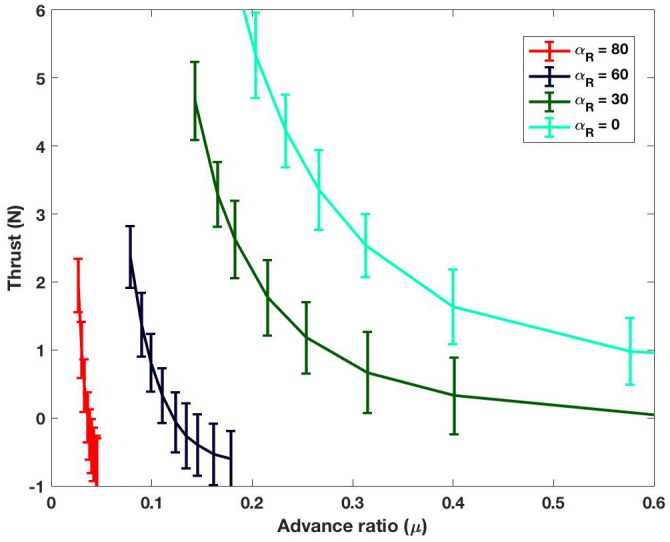

Figure 4.11: Uncertainty in thrust for $V_\infty = 15$ m/s.

As noted, the uncertainty is significantly larger for $V_\infty = 15$ m/s compared to lower speeds where the flow fluctuations appear to be less intense.

4.3 Evaluation of Predictive Capabilities

The predictions from the HBEM model were compared and validated against the experimental wind tunnel data. For every free-stream speed V_∞ and rotor angle of attack α_R, the motor throttle input varied from 0 to 0.9 (i.e. 90%) as discussed in Section 4.2. There are thus a total of 9 data points for each combination of $\{V_\infty, \alpha_\mathrm{R}\}$. It is noted that the first data point (not shown in the plots) is the "off" condition where the throttle input is zero.

For $V_\infty = 0$ m/s and $\alpha_\mathrm{R} = 90°$, the predicted thrust given propeller RPM condition is shown in Fig. 4.12. The experimental data and HBEM model are clearly in good agreement.

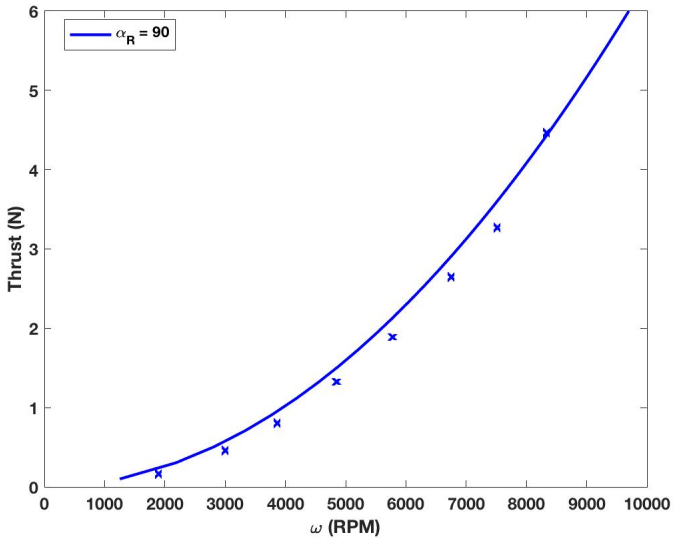

Figure 4.12: Model validation, thrust versus μ for $V_\infty = 0$ m/s. Symbols: Experiment, Lines: HBEM Model.

Figs. 4.13-4.15 show thrust versus advance ratio for the three free-stream speeds: $V_\infty = 5, 10$ and 15 m/s.

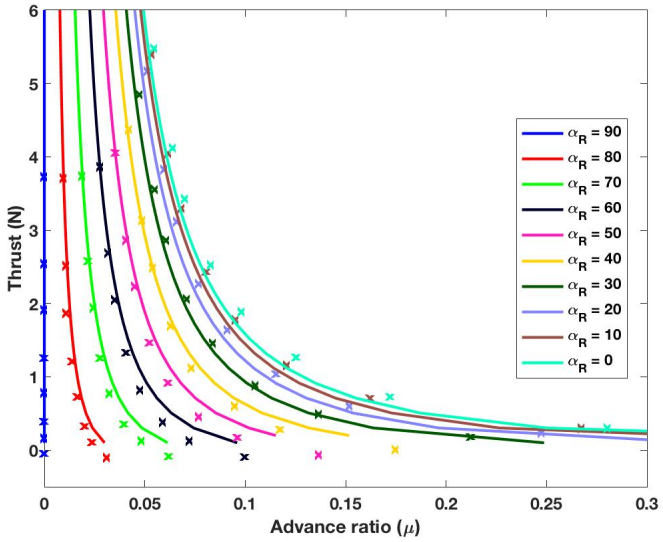

Figure 4.13: Model validation, thrust versus μ for $V_\infty = 5$ m/s. Symbols: Experiment, Lines: HBEM Model.

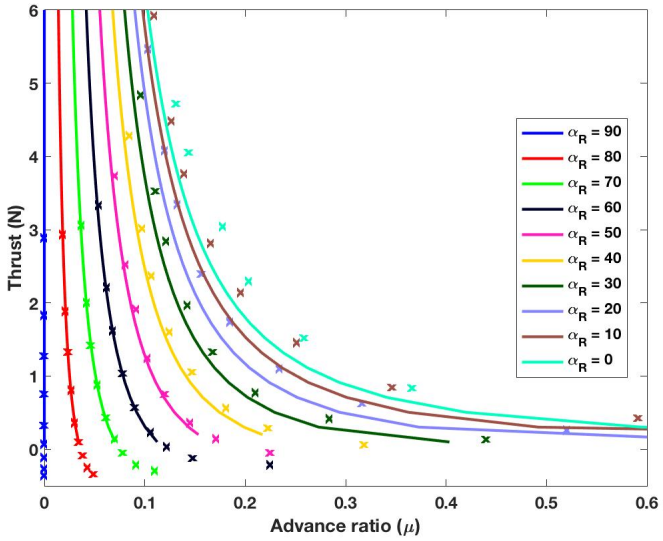

Figure 4.14: Model validation, thrust versus μ for $V_\infty = 10$ m/s. Symbols: Experiment, Lines: HBEM Model.

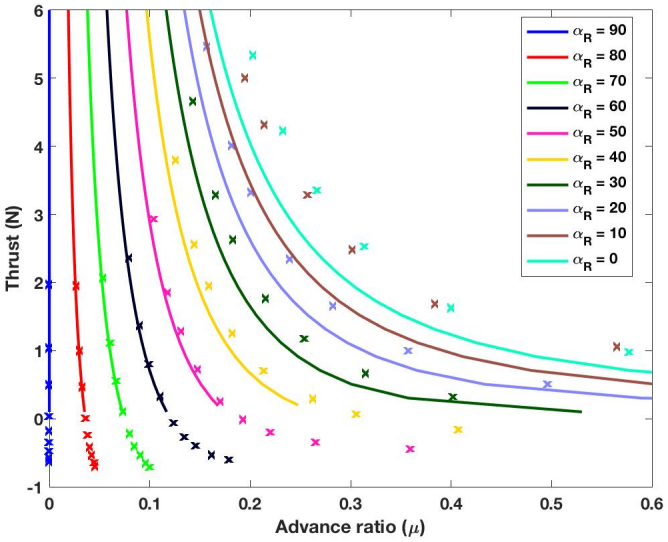

Figure 4.15: Model validation, thrust versus μ for $V_\infty = 15$ m/s. Symbols: Experiment, Lines: HBEM Model.

The predictions of thrust from the HBEM model are generally in good agreement with the experimental data for all three free-stream speeds. It is noted that the model discrepancy is larger for lower angles of attack. As discussed in Section 4.2.1, the experimental conditions may have more pronounced ground effect for lower angles of attack.

In Figs. 4.14 and 4.15, some experimental data points indicate negative thrust values. For instance, in Fig. 4.15, thrust is negative for $50^\circ < \alpha_R < 90^\circ$. This implies that the inflow angle Φ is larger than the blade twist angle Θ on average, leading to an effective angle of attack ($\alpha_{\text{eff}} < 0$) that is negative for a majority of airfoil sections along the span, and thus an aggregate negative lift/thrust for the rotor (see Eq.(4.5) and Eq. (4.7)).

Similar plots are shown for rotor thrust versus climb ratio in Figs. 4.16-4.18.

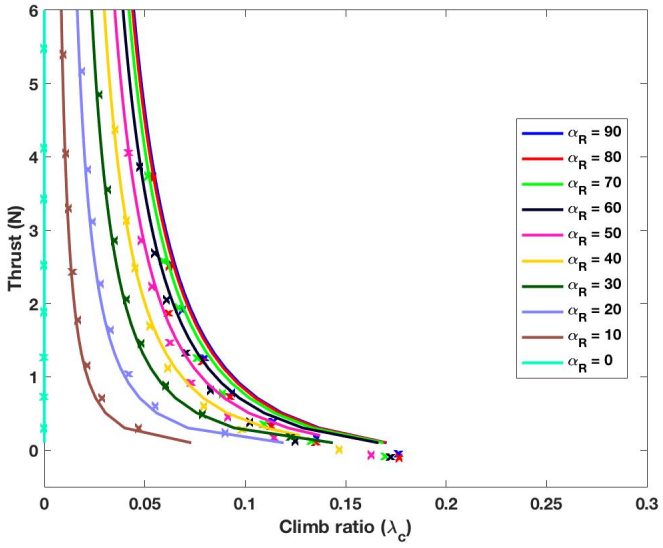

Figure 4.16: Model validation, thrust versus λ_c for $V_\infty = 5$ m/s. Symbols: Experiment, Lines: HBEM Model.

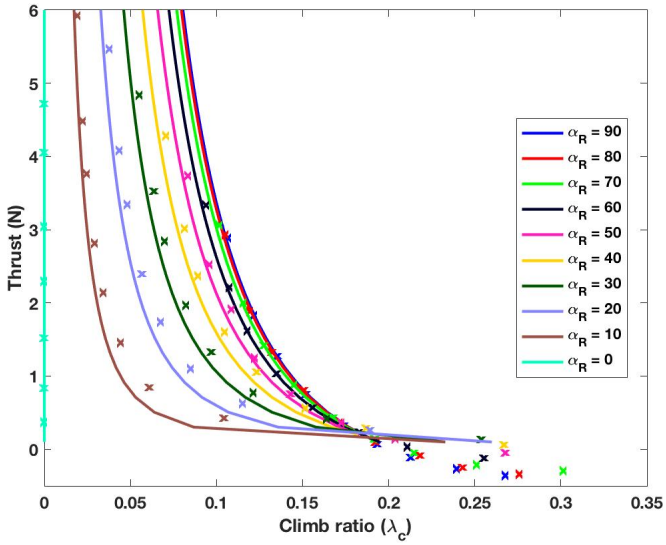

Figure 4.17: Model validation, thrust versus λ_c for $V_\infty = 10$ m/s. Symbols: Experiment, Lines: HBEM Model.

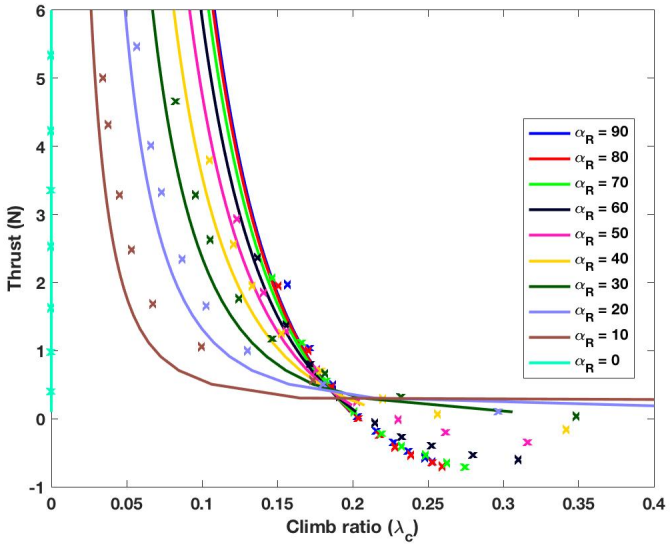

Figure 4.18: Model validation, thrust versus λ_c for $V_\infty = 15$ m/s. Symbols: Experiment, Lines: HBEM Model.

The HBEM model predictions are again in good agreement with the experimental data. The HBEM model shows a similar trend and predicts the point of collapse of the curves at $\mu = 0.15, 0.18$ and 0.19 for $V_\infty = 5, 10$ and 15 m/s respectively as shown in Fig. 4.16-4.18.

In the operation of rotary wing UAVs, the relationship between thrust and RPM condition is extremely important. These plots are often referred to as the "thrust map," and used as a lookup table that relates each throttle value to a thrust value in embedded control software.

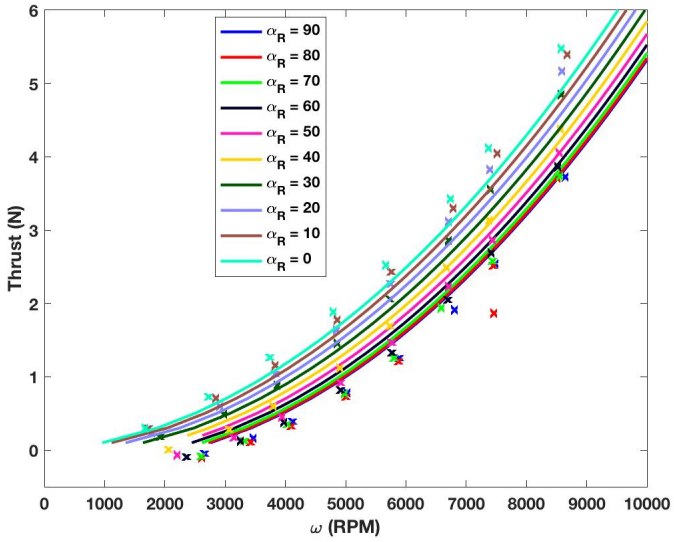

Figure 4.19: Model validation, thrust versus RPM for $V_\infty = 5$ m/s. Symbols: Experiment, Lines: HBEM Model.

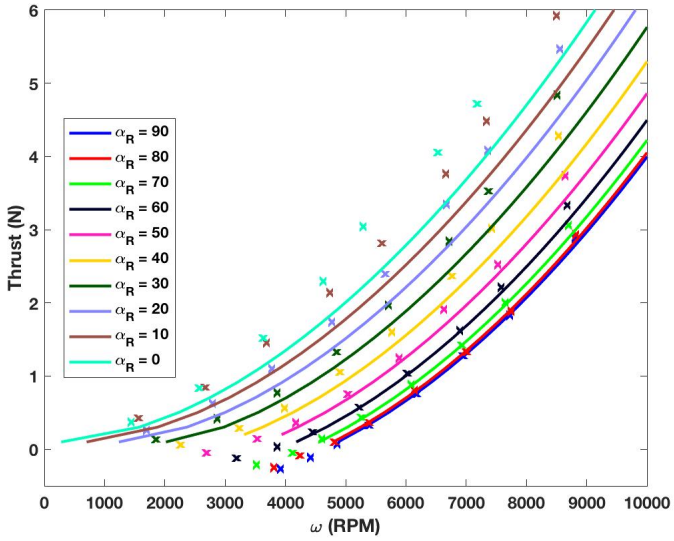

Figure 4.20: Model validation, thrust versus RPM for $V_\infty = 10$ m/s. Symbols: Experiment, Lines: HBEM Model.

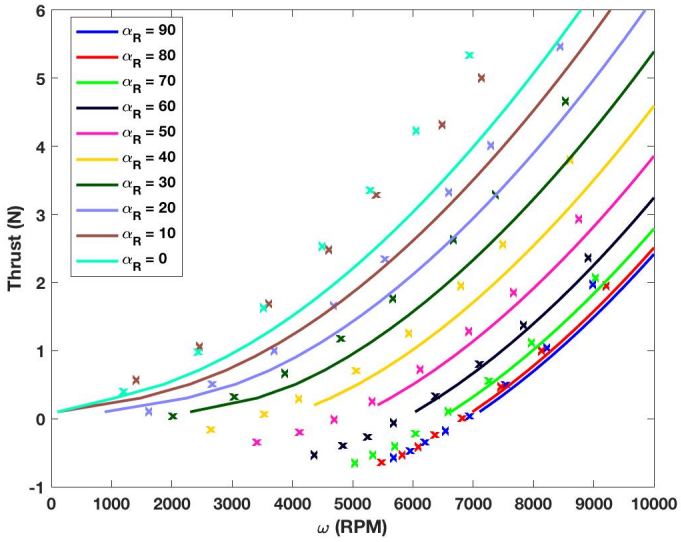

Figure 4.21: Model validation, thrust versus RPM for $V_\infty = 15$ m/s. Symbols: Experiment, Lines: HBEM Model.

As expected, Figs. 4.19, 4.20, 4.21 show that the thrust is a strong function of the free-stream speed and rotor angle of attack. However, in some embedded controller routines, the thrust map of a propeller in hover condition is usually employed over the entire flight envelope.

The predictions error and their associated experimental uncertainties are shown in Fig. 4.22. The root mean-square of the difference between experimental and predicted values of thrust is averaged over different RPMs (i.e., throttle condition) for every rotor angle of attack (α_R) and free stream speed V_∞.

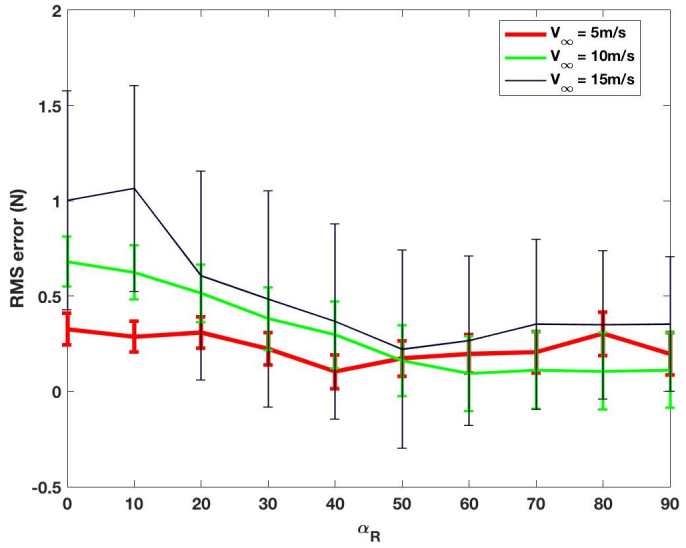

Figure 4.22: RMS error with respect to experimental mean Error bars represent experimental uncertainty.

As noted, the predictions are more accurate for lower free stream speeds and higher angle of attacks. It is also noted that very low angles of attack and high free stream speeds may not be realizable during actual flight, because the rotor needs to tilt enough to generate a high forward speed. The experimental data was obtained in a wind tunnel in which the free stream speed can be changed independently.

4.4 Rotor In-plane Force (RIP) Model

The Rotor In-plane Force (RIP) model is often referred to as drag represented in body frame. For a single rotor, the in-plane force (also called ”side force”) consists of blade profile drag and induced drag. It is cumbersome to quantify in-plane force accurately using geometry and flight parameters given the complex nature of the problem. Therefore, drag in the body frame or equivalently the in-plane force can be approximated as a ratio of the thrust. For instance, Ref. [113] introduced a lumped drag force model that relates drag in the body frame to the thrust for a quadrotor that is discussed in Section 3.2.2.

In this research work, an explicit model is introduced in Eq. (4.12) using in-plane force

measurements and an optimization procedure. This model relates in-plane force coefficient ($C_{\mathrm{F_I}} = F_{\mathrm{I}}/\rho\pi R^2 V_{\mathrm{tip}}^2$) to thrust coefficient (that can be quantified and obtained using HBEM model discussed earlier) and other non-dimensional flight parameters as follows:

$$C_{\mathrm{F_I}} = [(a_1 C_{\mathrm{T}}(sin(\alpha_{\mathrm{R}}) + b_1)) {Re_{V_\infty}}^{0.4} + c_1 \sigma c_{\mathrm{d_0}}(\mu^2 + \lambda^2)(sin(\alpha_{\mathrm{R}}) + d_1)] \cos\alpha_{\mathrm{R}}, \quad (4.12)$$

where the Reynolds number based on the free stream and rotor diameter is $Re_{V_\infty} = 2RV_\infty/\nu$. Also, blade solidity is $\sigma = 0.1083$, blade profile drag is $c_{d0} = 0.008$. Coefficients a, b, c and d are obtained using curve fitting and an optimization procedure, and they are $a_1 = 27.87e-04, b_1 = 75.37e-4, c_1 = 178.8960, d_1 = -0.1463$. It is good to mention that Eq. 4.12 with an additional parasite drag (see Eq. (5.20)) can be used to fully represent a quad-copter drag force that will be later discussed in Eqs. (5.14)-(5.16).

It is noted that the in-plane force model (i.e., drag force in body frame) is universal and not specific to the rotor used in this study. Geometric properties of the rotor manifest themselves in the thrust coefficient. It is noted that the experimental data incorporate extensive measurements over different incoming velocity (i.e., wind tunnel speeds), rotor angle of attacks (α_{R}) and rotor RPM conditions.

Experimental data versus predictions made by the in-plane force model (represented in Eq.4.12) for different incoming velocity $V_\infty = 5, 10, 15$ m/s and $0^\circ \leq \alpha_{\mathrm{R}} \leq 80^\circ$ are shown in Figs. 4.23-4.25.

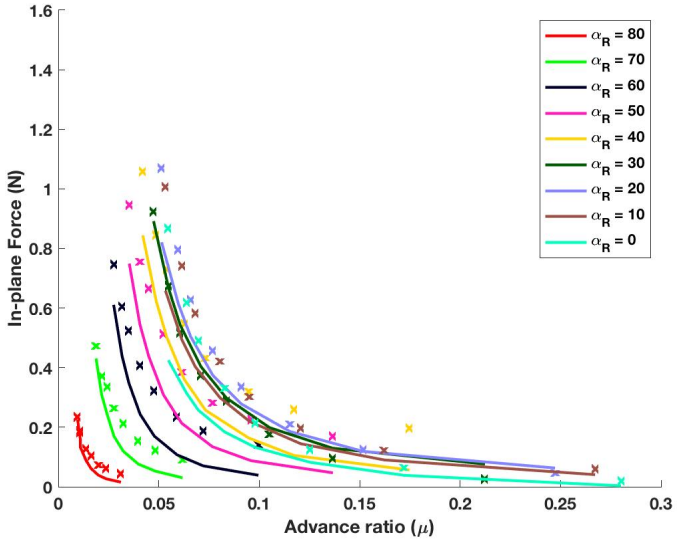

Figure 4.23: In plane force versus advance ratio for $V_\infty = 5$ m/s.

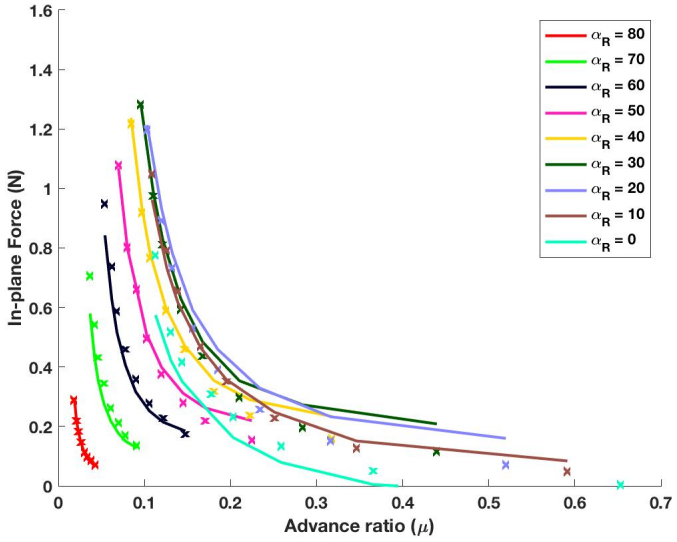

Figure 4.24: In plane force versus advance ratio for $V_\infty = 10$ m/s.

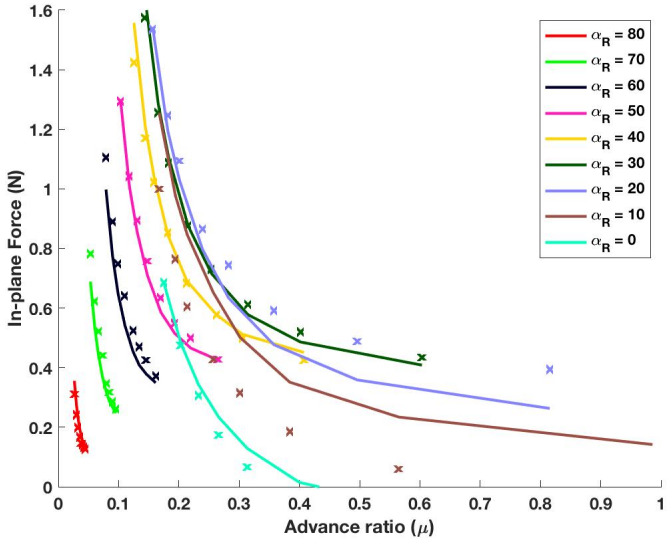

Figure 4.25: In plane force versus advance ratio for $V_\infty = 15$ m/s.

As noted, the predictions are in remarkable agreement with experimental data given that in-plane force is often very hard to estimate due its complex nature. As noted, the in-plane force decreases with angle of attack increase for the range about $0^\circ \leq \alpha_\mathrm{R} \leq 30^\circ$ and then consistently decrease for $30^\circ \leq \alpha_\mathrm{R} \leq 80^\circ$ which is indicative of a non-linear behaviour of drag in body frame versus rotor angle of attack. The in-plane force model seem to have captured the non-linearity reasonably well. To better illustrate the non-linearity, the in-plane force versus rotor angle of attack for different RPM conditions are plotted using experimental data in Eqs. 4.26-4.28.

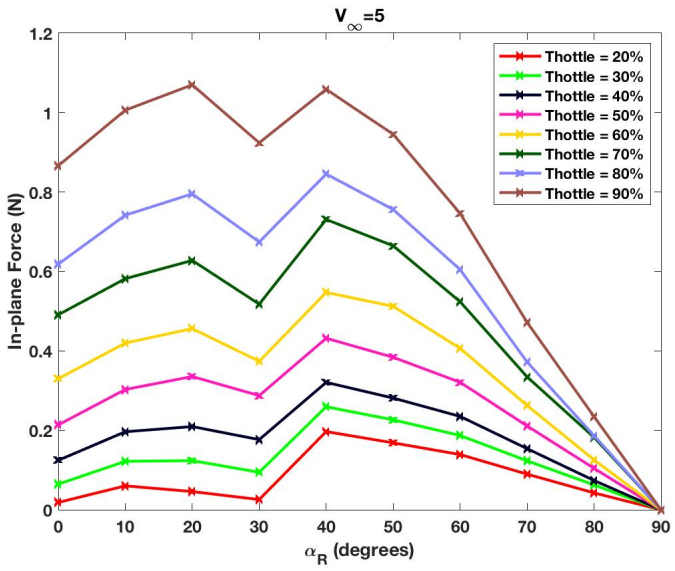

Figure 4.26: In-plane force versus rotor angle of attack for $V_\infty = 5$ m/s.

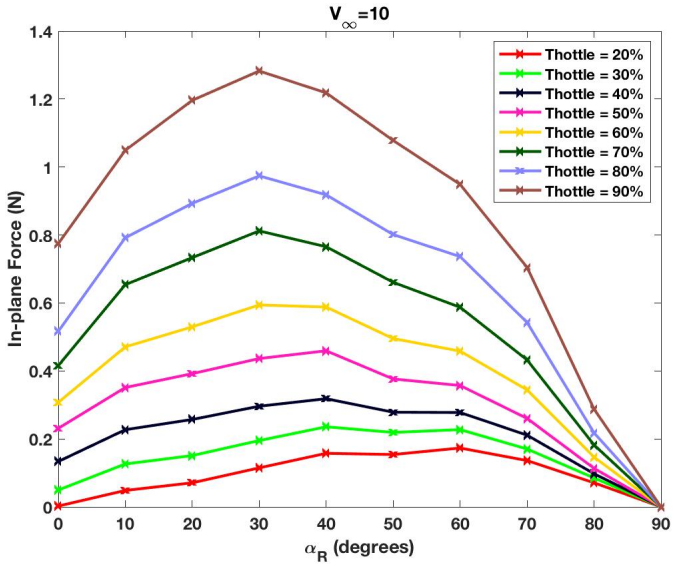

Figure 4.27: In plane force versus rotor angle of attack for $V_\infty = 10$ m/s.

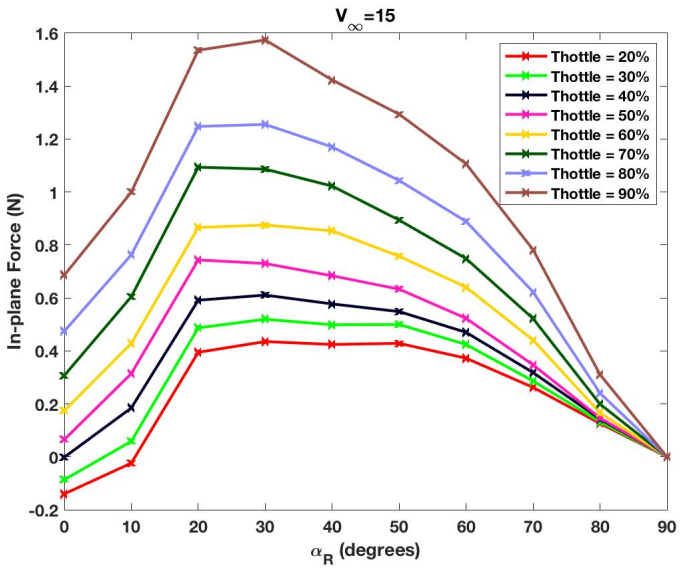

Figure 4.28: In-plane force versus rotor angle of attack for $V_\infty = 15$ m/s.

As noted, the in-plane force is maximum at about $20° < \alpha_R < 30°$.

4.4.1 RPM-Throttle Model

The relationship between RPM condition and throttle values are often only obtained in hover condition using a dynamometer. In practice, the incoming flow and rotor angle of attack alter the relationship between RPM condition and throttle value because the loading on the blades change.

Experimental data presented in this chapter can be used to find accurate relationship between throttle value and RPM condition. For incoming speed $V_\infty = 5, 10$ and 15 m/s, the relationship between RPM and throttle values for different rotor angles of attacks are plotted in Figs. 4.29-4.31.

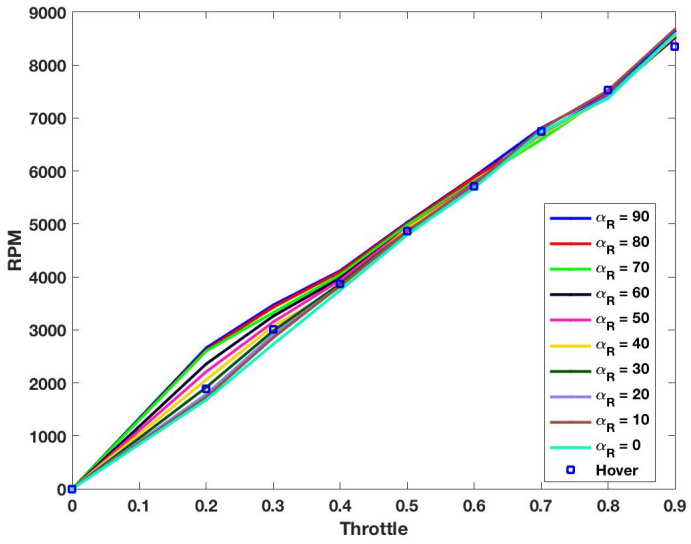

Figure 4.29: Relationship between RPM and throttle for $V_\infty = 5$ m/s.

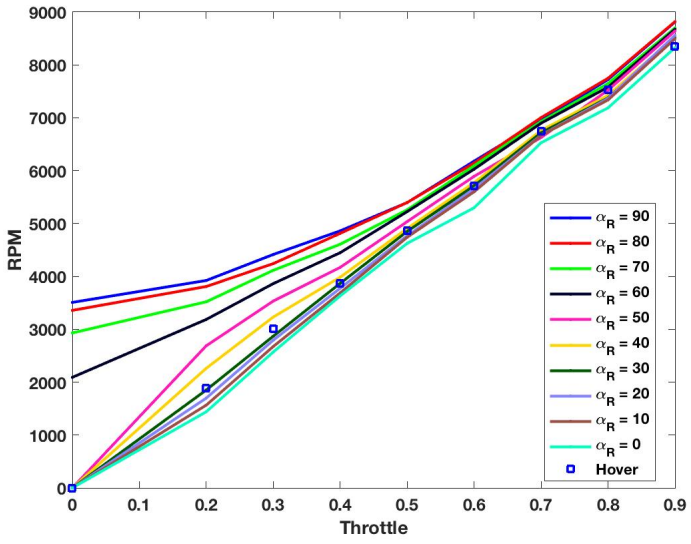

Figure 4.30: Relationship between RPM and throttle for $V_\infty = 10$ m/s.

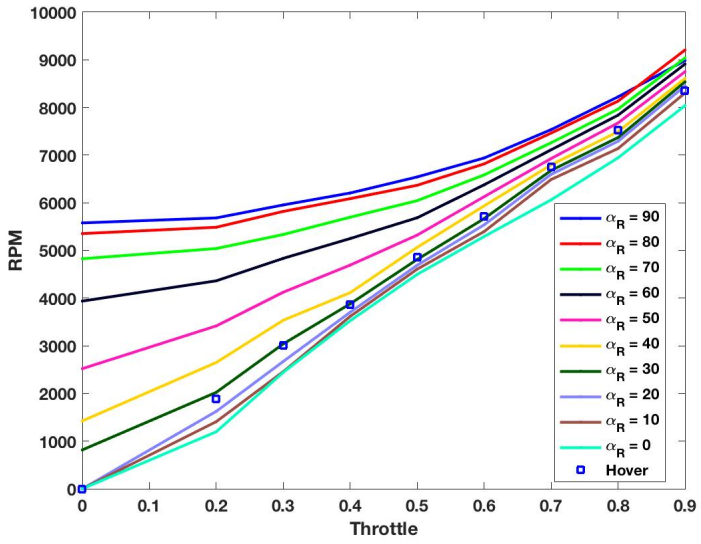

Figure 4.31: Relationship between RPM and throttle for $V_\infty = 15$ m/s.

As shown in Figs. 4.29-4.31, the larger the free stream and rotor angle of attack are, the more the results for RPM-Throttle deviate from the one of hover condition. Based on Fig. 4.29, it is evident that for low speed flights < 5m/s, the hover condition relationship is acceptable to be used for all rotor angles of attack.

4.5 Performance Model for Torque and Power

A typical quad-copter in $+$ configuration (refer to schematic and rotor configuration in Fig. 4.1 is considered. The differential thrust among the four rotors of the quad-copter and moments from each individual rotor leads to the roll and pitch moments (τ_x and τ_y).

$$\tau_{\mathrm{x}} = l(T_4 - T_2) + \sum_{i=1}^{4} \tau_{\mathrm{x}_{r_i}}, \qquad \tau_{\mathrm{y}} = l(T_1 - T_3) + \sum_{i=1}^{4} \tau_{\mathrm{y}_{r_i}}. \tag{4.13}$$

It is noted that each rotor individually has some roll and pitch moments associated with it that are usually neglected. These extra moments are amplified in forward flight, and can

be quantified using Eq. (4.8).

The roll and pitch moments in Eq. (4.8) are defined in the configuration in which the incoming velocity is aligned with the zero azimuth angle position ($\Psi = 0$). Therefore, these moments have to be projected on the body coordinate system. A heading angle, $h = \tan^{-1}(V_{\text{rel}_{B_y}}/V_{\text{rel}_{B_x}})$, is defined to represent the angle between the relative incoming wind and the x-axis of the body coordinate system. Note that this is different from the Euler yaw heading angle (ψ). The moments generated by rotor # i are:

$$\tau_{\text{x}_{r_i}} = \rho\pi R^3 V_{\text{tip}}^2 \left[C_{\text{r}} \cos(h)(-1)^{i+1} - C_{\text{p}} \sin(h)\right], \tag{4.14}$$

$$\tau_{\text{y}_{r_i}} = \rho\pi R^3 V_{\text{tip}}^2 \left[C_{\text{r}} \sin(h)(-1)^{i+1} + C_{\text{p}} \cos(h)\right]. \tag{4.15}$$

The coefficient $(-1)^{i+1}$ takes into account the sense of the rotor rotation. Roll moments are negative for rotors #1 and 3, and positive for rotors #2 and 4. This implies that the net roll moment on the quad-copter should be close to zero as a consequence of the opposing contributions of each of the rotors. However, the pitching moment contribution from each rotor is accumulative, and the net will not be close to zero. This will further be discussed in the flight simulation section, yet it was already indicated that the total pitching moment should be positive (pitch-up), see Fig. 4.5.

Yaw moments (τ_{z}) produced by a quad-copter - similar to roll - are not accumulative. Rotors #1 and 3 generate positive yaw moment (yaw moment vector points to the ground) and Rotors #2 and 4 generate a negative yaw moment. As described in Section 3.2.1, the yaw moment coefficient (C_{y}) is the same as the power coefficient (C_{P}) in rotary wing aerial vehicles. The yaw moment is found using Eq. (3.10).

4.6 Flight simulation

Flight simulation was performed for a typical quad-copter with the following geometric properties: mass, $m = 1.0362$ kg, arm length, $l = 0.15$ m, X-moment of inertia, $I_{\text{x}} =$

0.01167 kg m^2, Y-moment of inertia, $I_{\mathrm{y}} = 0.011465$ kg m^2, Z-moment of inertia, $I_{\mathrm{z}} = 0.0216$ kg m^2, rotor moment of inertia, $I_{\mathrm{r}} = 1.5 \times 10^{-5}$ kg m^2. The coefficient b and k used for thrust and torque for the simplified model ($T_{\mathrm{i}} = b\omega_{\mathrm{i}}^2$ and $\tau_{\mathrm{z_i}} = k\omega_{\mathrm{i}}^2$) are $b = 5.6 \times 10^{-8}$ [N/(RPM)^2] and $k = 8.9 \times 10^{-10}$ [Nm/(RPM)^2] respectively.

Flight simulations were performed in the Simulink environment of MATLAB. Details of dynamic Model and control hierarchy are presented in Ref.[74]. A non-linear backstepping controller is used [73] to track the target trajectory.

A simple rectangular path was defined as: 1) taking off to an altitude of 40 m, 2) accelerating to a cruise speed of 10 m/s, 3) continuing with the cruise speed, 4) decelerating to make a stop 400 meters from the start point. 5) landing.

The target trajectory and the vehicle attitude and position were successfully controlled. The target and resultant position of the quad-copter are shown in Fig.4.32.

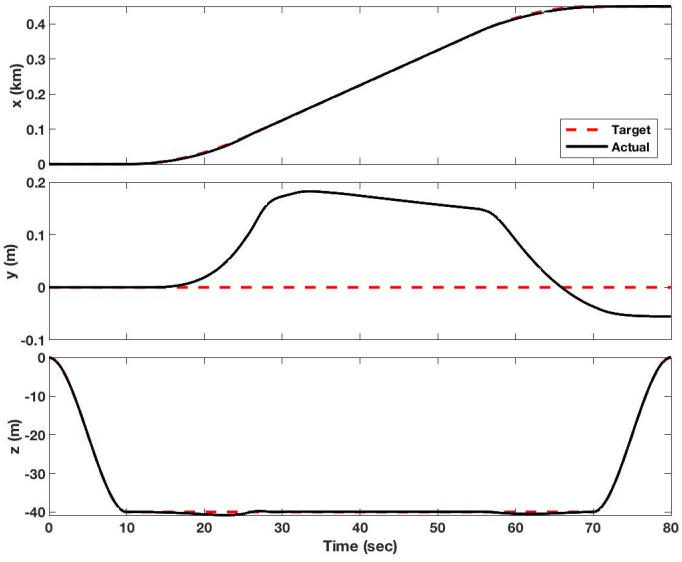

Figure 4.32: Location of the quad-copter CG in flight simulation.

The target position is well-tracked as observed in Fig. 4.32. Next, the target velocity versus the actual velocity of the vehicle is plotted in Fig. 4.33.

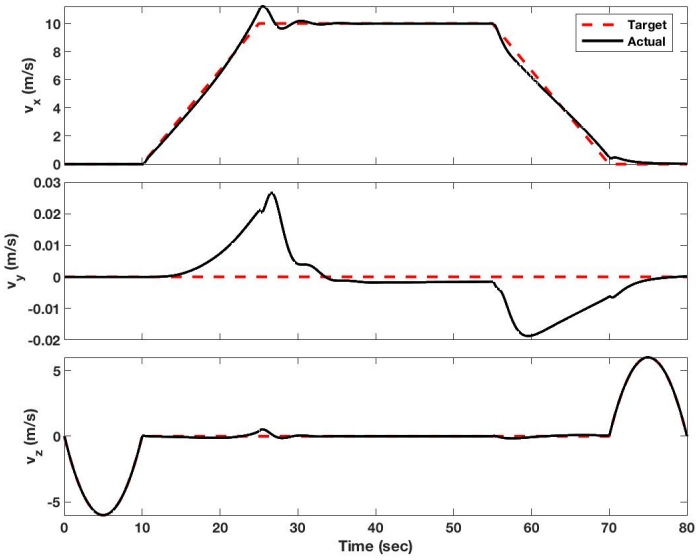

Figure 4.33: Velocity of the quad-copter CG.

Similar to the vehicle position, the target velocity is also well-tracked. The largest discrepancy was observed in the deceleration phase of the flight ($55\text{ s} < t < 70\text{ s}$). The target path versus the actual path is shown in Fig. 4.34. Note that the axis scales are not equal, and in fact the target and actual paths are very close.

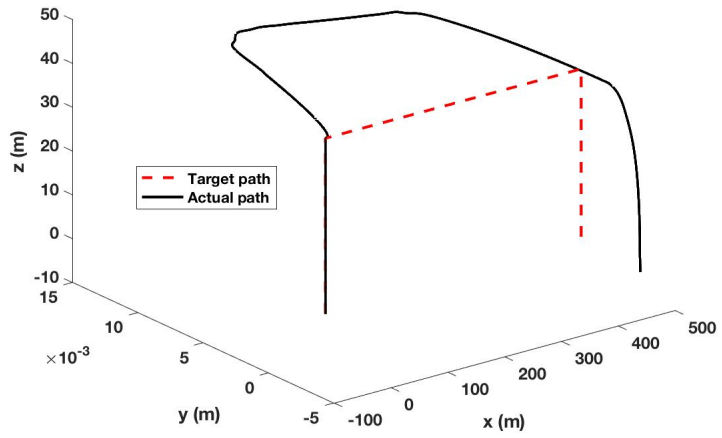

Figure 4.34: Flight path. Note: Scales in each axis are different.

The Euler angles, Euler angles rates and moments are shown in Fig. 4.35. It is noted

that the yaw Euler angle can be set independently, and the yaw angle was commanded to be zero during the flight.

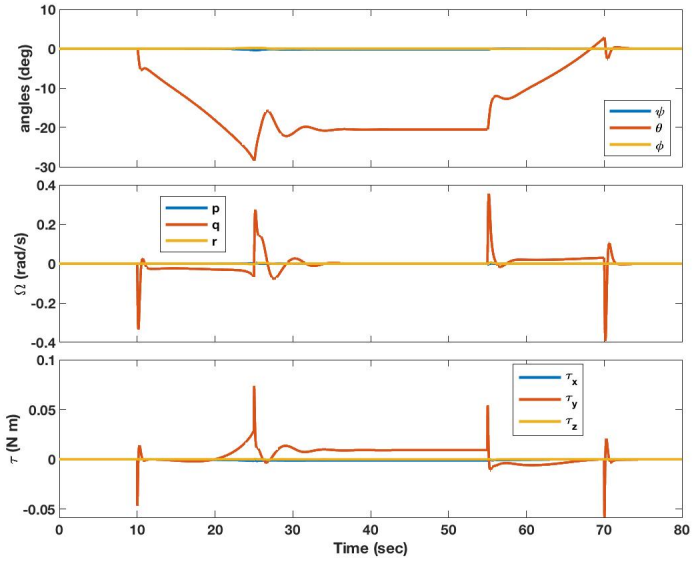

Figure 4.35: Euler angles (yaw, pitch and roll), Euler angles rates and moments of the quad-copter during flight.

As noted in Fig. 4.35, the pitch Euler angle is about $\theta = -20^\circ$ (pitch down, as shown in Fig. 4.1). The HBEM model is integrated with the 6 DoF controller, and thus the required RPM condition to generate the required thrust can be estimated in every flight condition. The RPM predictions by the HBEM model, Radial Inflow model (used in Ref. [74]), and simplified model are compared against each other in Fig. 4.36.

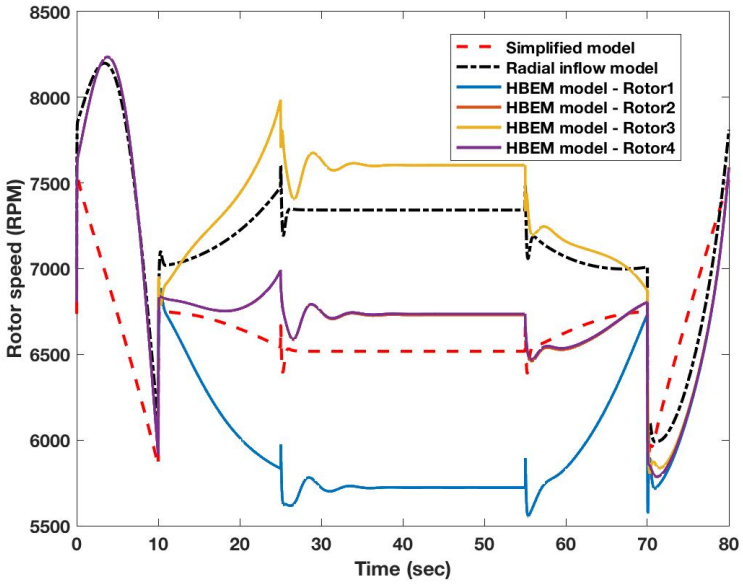

Figure 4.36: Rotor RPM predictions from different models.

The Radial inflow model is known to be accurate in axial flight. Interestingly, the HBEM model agrees very well with the radial inflow model in the axial flight phase (0 s $< t <$ 10 s and 70 s $< t <$ 80 s) as seen in Fig. 4.36. As mentioned earlier, the HBEM is capable of estimating roll and pitch moments of each rotor individually. It was also noticed that each rotor will generate a pitch-up moment. As observed, in Fig. 4.36, rotor $\#3$ is operating at a larger angular velocity (i.e., generating more thrust) compared to rotor $\#1$. The resultant moment of this thrust differential counter-acts the extra pitch-up by developing a pitch-down moment (Fig. 4.1).

The radial inflow and simplified models predict the same RPM for all rotors except at the points of transition. The rotation speed of rotor $\#1$ of these two models is shown in Fig. 4.36.

CHAPTER 5

Experimental Quadrotor Sensor Design and Control

The reliability and resilience of autonomous systems is tied to effective planning and control models, which in turn can benefit from efficient physical models. Moreover, sensing and reconstructing extreme environmental conditions are crucial for robust autonomous systems. In the previous chapters, efficient aeromechanical models of appropriate fidelity for UAV were developed. The goal of this chapter is to enable the developed rotary-wing aeromechanical models to be used onboard a quadrotor. A feedforward controller is designed that uses the physics-based models, and these models are implemented within the flight software.

Firstly, a custom quadrotor with an *Xconfiguration* was built. A quadrotor using the *X configuration* is selected rather than a $+$*configuration*, because of the higher maneuverability of the *X configuration* given that two rotors are used for rolling and pitching moments [131]. Sensors for measuring the RPM of the electrical motors and the incident wind were developed to be well-integrated with the quadrotor.

A flight controller software from *Strawson Robotics Library* was adopted and modified to meet the expectations and requirements of the current study. Controllers for attitude, altitude and position are developed.

5.1 Quadrotor Characteristics

The 3S Li-Po battery and 8-inch propeller combination are selected for the quadrotor based on the minimum thrust required to levitate and provides the necessary acceleration in forward flight. Four 8-inch propellers offer enough lift for the quadrotor given the overall weight of the system. It is noted that HBEM model can be used in the design process to find the appropriate blade shape and size. The custom quadrotor is shown in Fig.5.1.

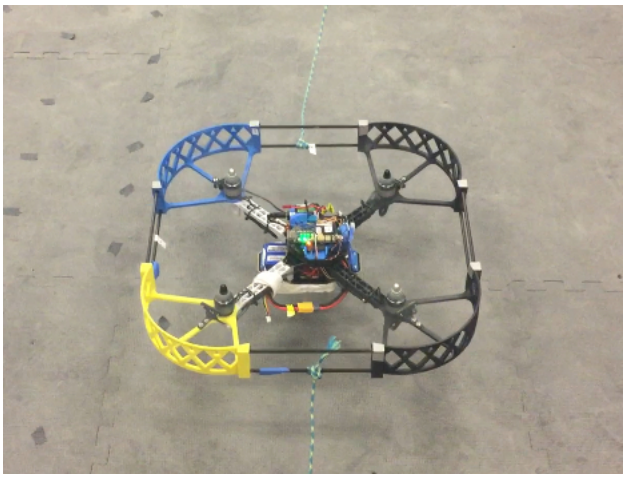

Figure 5.1: Assembled quadrotor.

The onboard computer is BeagleBone Blue (shown in Fig. 5.2) that has the AM335x 1GHz ARM® Cortex-A8 processor. The overall weight of quadrotor is measured at 1080 grams, and its size is about 40 cm x 40 cm x 6 cm. The mass of the different components of the quadrotor is provided in Table 5.1.

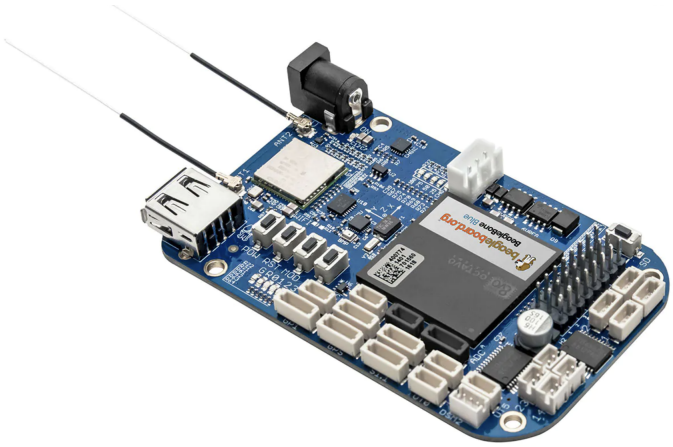

Figure 5.2: BeagleBone Blue.

Table 5.1: Mass of quadrotor components (in grams).

	Corner 1	Corner 2	Corner 3	Corner 4
Motor	61.7	62.4	61.4	61.9
Propeller	8.8	8.7	8.8	8.8
Propeller nut	1.8	1.8	1.8	1.8
ESC	15.4	15.7	15.4	15.4
Shell	39.2	38.8	39.7	38.5
Carbon Rod(x2)	6.8	6.7	6.9	6.7
Arm	24.5	24.6	24.3	24.8
RPM Sensor	0.8	0.8	0.7	0.8
RPM Sensor wiring	0.6	0.6	0.6	0.6
Wind sensor		50		
Mid Plate1		15.7		
Mid Plate2		14.2		
Mid Plate3		31.7		
BeagleBone Board		37.2		
Receiver		4.2		
Main Battery		221		
Small Battery		13.7		
Cable		37.1		
Estimated Overall Mass : 1086.2				

The moments of inertia are found using two different ways. The first method is to use Bifilar Pendulum, and the second method is by modeling a simplified quadrotor using Creo model and the quadrotor components' mass.

5.1.1 Bifilar Pendulum Method

The quadrotor is hung via a long string. The periodic back-and-forth movements around each axis are counted and timed. The moment of inertia about x axis is obtained using Eq. (5.1):

$$J_{\text{xx}} = \frac{m_0 g d^2}{16\pi^2 L} T_0^2, \tag{5.1}$$

Similarly, J_{yy} and J_{zz} are also obtained using Eq. (5.1).

5.1.2 Estimating Moments of Inertia

The density can be calculated based on the mass of each component. The Density, size, and position of each component are provided for Creo model in order to estimate the moments of inertia. The Creo model of the quadrotor is shown in Fig. 5.3.

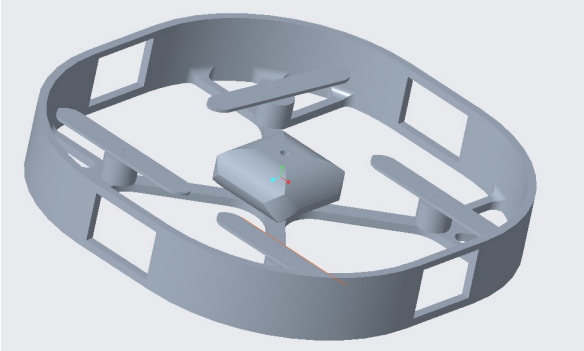

Figure 5.3: Creo model of the quadrotor.

The comparison between the estimated versus measured moments of inertia is provided in Table 5.2.

Table 5.2: Moment of inertia.

Moment of Inertia	Measured with Pendulum	Creo Model Estimates
J_{XX}	0.01167902	0.01345732
J_{YY}	0.011465268	0.01474434
J_{ZZ}	0.021638232	0.02795551

5.2 Feedback Controllers

5.2.1 Inter-Loop Attitude PD Controller

The proportional-integral-derivative (PID) controller is a simple, yet reliable controller and is used for attitude control. It is often used for feedback control in applications that require continuous modulated control. A block diagram for a PID controller is shown in Fig. 5.4.

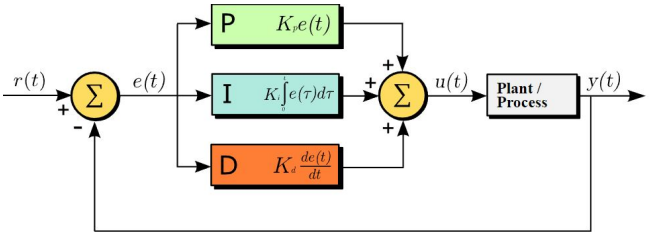

Figure 5.4: PID block diagram.

The input to the PID controller is an error ($e(t)$) that is defined as the desired state minus the current state; $e(t) = x_{\mathrm{d}}(t) - x(t)$. The output ($u(t)$) is the control that drives the system towards the desired setpoints. In attitude control, the desired Euler angles are set by the outer-loop position controller described in Section 5.2.2. Also, the current Euler angles are measured using BeagleBone Blue's onboard gyroscope.

$$u(t) = K_{\mathrm{p}} e(t) + K_{\mathrm{i}} \int_0^t e(\tau)d\tau + K_{\mathrm{d}} \frac{de(t)}{dt}. \tag{5.2}$$

The PID controller equation contains three separate terms, namely proportional, inte-

gral and derivative. The proportional term ($u_p(t)$) drives the system to the desired state by multiplying the error term by a constant proportional gain, K_{p}

$$u_{\mathrm{p}}(t) = K_{\mathrm{p}} e(t). \tag{5.3}$$

The integral term ($u_{\mathrm{i}}(t)$) reduces steady state error in the system. This integral term is often set to zero for attitude control, hence $K_{\mathrm{i}} = 0$.

$$u_{\mathrm{i}}(t) = K_{\mathrm{i}} \int_0^t e(\tau) d\tau. \tag{5.4}$$

The derivative term ($u_{\mathrm{d}}(t)$) helps the system to reduce oscillations that originally caused by overshooting that can be introduced by the proportional term. However, over-damping causes a steady state error into the system. The derivative gain (K_{d}) should be tuned with respect to the proportional gain (K_{p}).

$$u_{\mathrm{d}}(t) = K_{\mathrm{d}} \frac{de(t)}{dt}. \tag{5.5}$$

All three gains are tuned to produce the most desirable response in the system. A trial and error procedure in manual flight using a transmitter is a proper way to observe the behaviour of the quadrotor and tune the PID gains. Therefore, tuning PID gains primarily defines how the PID feedback controller would determine the response of the system.

As mentioned before, given that there is no steady state error, the low level controllers for the quadrotor uses a PD controller $K_{\mathrm{i}} = 0$. The tuned gains are presented in Table 5.3 as follows:

Table 5.3: Low level control gains.

	K_{p}	K_{i}	K_{d}
roll	0.35	0.0	0.25
pitch	0.35	0.0	0.25
yaw	3.0	0.0	0.2

5.2.2 Outer-loop PD position controller

Similarly, a PD controller is used to track the target trajectory. For every time step, the difference between the current and desired position are found, (i.e., err_{X}, err_{Y} and err_{Z}), and roll and pitch Euler angle setpoints are

$$\theta_{\text{sp}} = \text{PD}(-err_{\mathrm{X}}), \tag{5.6}$$

$$\phi_{\text{sp}} = \text{PD}(err_{\mathrm{Y}}). \tag{5.7}$$

These setpoint pitch and roll angles are next sent to the attitude controller to command the quadrotor to follow the trajectory. Gains for the X- and Y-position controls are provided in Table 5.4.

Table 5.4: X and Y position control gains.

K_{p}	K_{i}	K_{d}
0.5	0.0	0.2

Controlling Z-position (the altitude) of the vehicle should be treated differently and is discussed next.

5.2.2.1 Altitude Control

The same principles of a PD controller are applied to the altitude feedback controller. The err_{Z} is determined as difference between the current and target heights and is fed into the controller. The altitude controller design is presented in Eq. (5.8):

$$U_{\text{z}} = \text{Throttle}_{\text{hover}} + \frac{\text{PD}(err_{\mathrm{Z}})}{\cos\phi\cos\theta}, \tag{5.8}$$

where $U(Z)$ is the control output, and $\text{Throttle}_{\text{hover}}$ is the approximate throttle for hovering and is constant, $\text{Throttle}_{\text{hover}} = -0.6$ for the current quadrotor. It is noted that altitude control gains should be updated based on the current battery voltage. The following gains shown in Table 5.5 are found to be optimal for altitude control.

Table 5.5: Altitude control gains.

K_{p}	K_{i}	K_{d}
0.2	0.0	0.2

5.2.2.2 Motion Capture System and Ground Station Setup

OptiTrack motion capture system is used to estimate the position of the quadrotor in real-time. A camera of the motion capture system is shown in Fig. 5.5. Seven cameras are used to accurately track the location of the quadrotor. Position of the cameras are shown in Fig. 6.1. The motion capture system is calibrated every two hours to ensure the location information is correct.

It is noted that the OptiTrack motion capture system can provide the position information as well as the Euler angles of the vehicle, however, the built-in onboard gyroscope in the BeagleBone is used to estimate the current roll, pitch and yaw information.

Figure 5.5: A camera of the OptiTrack motion capture system.

The position information is first sent to the *Motive* software installed on a Laptop. The data is then sent to a BeagleBone Black where it is further sent through a serial port to an Xbee transmitter. There is also another Xbee receiver on the quadrotor, and the two xbees are programmed to communicate and transfer the location data. A schematic of the circulation of information is shown in Fig. 5.6

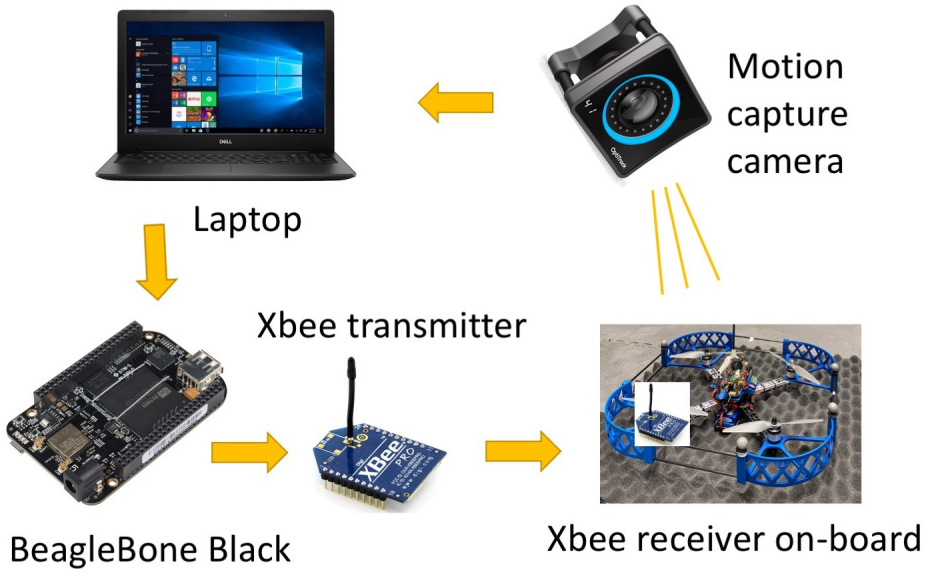

Figure 5.6: Communication setup for autonomous position control.

5.3 Feedforward Controller

The relationship between throttle condition (or equivalently RPM condition) and thrust is traditionally quantified using a table look-up called thrust map. The thrust maps are often obtained using a dynamometer installed on a desk in the lab (resemblance hover condition). Use of such table look-up leads to a considerable inaccuracy in forward flight [132]. Therefore, a model for thrust reliable across a wide range of flight regimes is desired. The HBEM model was implemented in C Code language. The C Codes were compiled using specific Cortex-A CPU libraries to increases performance in the BeagleBone Blue onboard hardware.

While the contributions to the drag comes from many different sources, they can be decomposed into a rotor in-plane force and parasite drag at the system level. A full balance of forces on a quadrotor tracking a general path and undergoing a random wind condition is shown in Fig.5.7.

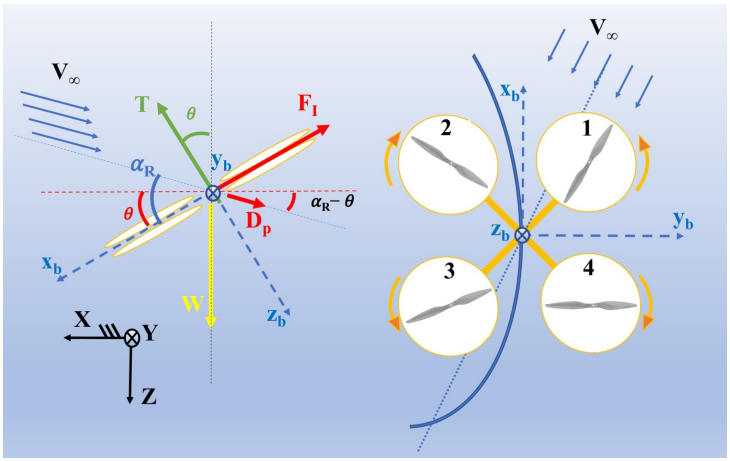

Figure 5.7: quadrotor applied forces subject to a cross wind on an arbitrary path.

In the body frame of the vehicle the balance of forces can be represented by the following equations:

$$\sum F_{\mathrm{xb}} = (F_{\mathrm{I}} + D_{\mathrm{p}} \cos \alpha_{\mathrm{R}}) \frac{v_{\mathrm{x}}}{\sqrt{v_x^2 + v_y^2}} - W \sin \theta, \tag{5.9}$$

$$\sum F_{\mathrm{yb}} = (F_{\mathrm{I}} + D_{\mathrm{p}} \cos \alpha_{\mathrm{R}}) \frac{v_{\mathrm{y}}}{\sqrt{v_x^2 + v_y^2}} + W \cos \theta \sin \phi, \tag{5.10}$$

$$\sum F_{\mathrm{zb}} = D_{\mathrm{p}} \sin \alpha_{\mathrm{R}} - T + W \cos \theta \cos \phi. \tag{5.11}$$

The Directional Cosine Matrix (DCM) is a rotation matrix that transfers a vector from the vehicle body frame to the inertial frame. The rotation sequence matters and is often assumed in the order of yaw-pitch-roll. The DCM is presented in Eq.(5.12):

$$DCM = \begin{bmatrix} \cos\theta\cos\psi & \cos\psi\sin\theta\sin\phi - \sin\psi\cos\phi & \cos\psi\sin\theta\cos\phi + \sin\psi\sin\phi \\ \cos\theta\sin\psi & \sin\psi\sin\theta\sin\phi + \cos\psi\cos\phi & \sin\psi\sin\theta\cos\phi - \cos\psi\sin\phi \\ -\sin\theta & \sin\phi\cos\theta & \cos\phi\cos\theta \end{bmatrix}. \tag{5.12}$$

The balance of forces in the body frame can be transferred to inertial frame. In our case, we intend to keep the reference yaw angle zero, therefore, the inertial forces can be obtained as:

$$\begin{bmatrix} \sum F_{\mathrm{X}} \\ \sum F_{\mathrm{Y}} \\ \sum F_{\mathrm{Z}} \end{bmatrix} = \begin{bmatrix} \cos\theta & \sin\theta\sin\phi & \sin\theta\cos\phi \\ 0 & \cos\phi & -\sin\phi \\ -\sin\theta & \sin\phi\cos\theta & \cos\phi\cos\theta \end{bmatrix} \begin{bmatrix} \sum F_{\mathrm{xb}} \\ \sum F_{\mathrm{yb}} \\ \sum F_{\mathrm{zb}} \end{bmatrix}. \tag{5.13}$$

Therefore, the net forces in the inertial frame can be found as follows:

$$\sum F_{\mathrm{X}} = \frac{F_{\mathrm{I}} + D_{\mathrm{p}}\cos\alpha_{\mathrm{R}}}{\sqrt{v_x^2 + v_y^2}}(v_{\mathrm{x}}\cos\theta + v_{\mathrm{y}}\sin\theta\sin\phi) + \sin\theta\cos\phi(D_{\mathrm{p}}\sin\alpha_{\mathrm{R}} - T), \tag{5.14}$$

$$\sum F_{\mathrm{Y}} = \frac{F_{\mathrm{I}} + D_{\mathrm{p}}\cos\alpha_{\mathrm{R}}}{\sqrt{v_x^2 + v_y^2}}(v_{\mathrm{y}}\cos\phi) - \sin\phi(D_{\mathrm{p}}\sin\alpha_{\mathrm{R}} - T), \tag{5.15}$$

$$\sum F_{\mathrm{Z}} = \frac{F_{\mathrm{I}} + D_{\mathrm{p}}\cos\alpha_{\mathrm{R}}}{\sqrt{v_x^2 + v_y^2}}(-v_{\mathrm{x}}\sin\theta + v_{\mathrm{y}}\sin\phi\cos\theta) + \cos\theta\cos\phi(D_{\mathrm{p}}\sin\alpha_{\mathrm{R}} - T) + W. \tag{5.16}$$

In the equilibrium condition, the net forces in all three directions in the inertial frame are zero. Equations (5.14)-(5.16) can be set to zero to find the equilibrium pitch and role angles (note that yaw was set to zero). By multiplying Eq.(5.14) by "$\cos\theta$" and adding it to Eq. (5.14) multiplied by "$-\sin\theta$", the pitch angle can directly be obtained.

$$\theta_{\mathrm{ref}} = \sin^{-1}\frac{\frac{F_{\mathrm{I}}+D_{\mathrm{p}}\cos\alpha_{\mathrm{R}}}{\sqrt{v_x^2+v_y^2}}v_{\mathrm{x}}}{W}. \tag{5.17}$$

By more mathematical manipulation, a closed form solution is possible. Thrust and roll angle (ϕ) can also be found and is given in Eqns. (5.18) and (5.19) respectively:

$$T_{\mathrm{ref}} = D_{\mathrm{p}}\sin\alpha_{\mathrm{R}} + \sqrt{W^2 - (F_{\mathrm{I}} + D_{\mathrm{p}}\cos\alpha_{\mathrm{R}})^2}, \tag{5.18}$$

$$\phi_{\mathrm{ref}} = \tan^{-1}\frac{\frac{F_{\mathrm{I}}+D_{\mathrm{p}}\cos\alpha_{\mathrm{R}}}{\sqrt{v_x^2+v_y^2}}(v_{\mathrm{y}})}{-\sqrt{W^2 - (F_{\mathrm{I}} + D_{\mathrm{p}}\cos\alpha_{\mathrm{R}})^2}}. \tag{5.19}$$

It is noted that Eq. (5.18) must be solved prior to Eqs. (5.17) and (5.19), because there is also a thrust term embedded in the rotor in-plane force (F_{I}). Therefore, a simple optimization method is needed to solve Eq.(5.18) to find T_{ref}, and subsequently, the other two equations for ϕ_{ref} and θ_{ref} are directly computed.

The rotor in-plane force F_{I} is computed using RIPF model (see Section 4.4). Also, a simple model for parasite drag can be formed and shown in Eq.(5.20) assuming the body of quadrotor as a flat strip:

$$D_{\mathrm{p}} = \frac{1}{2}\rho(S_{\mathrm{q}})(v_{\mathrm{x}}^2 + v_{\mathrm{y}}^2 + v_{\mathrm{z}}^2), \tag{5.20}$$

where $S_{\mathrm{q}} = 0.4 * 0.06\ m^2$ is an approximate to the frontal area of the quadrotor.

5.3.1 An important Accommodation

A very important step to use the feedforward controller presented earlier is to implement a strategy to remove the extraneous motion of quadrotor from the wind measurements. Also, assuming that wind velocity is mostly horizontal in the inertial frame, once can find z-velocity (here, it is denoted as w_{ff}) in the body frame (sensor frame) using directional cosine matrix (DCM). Therefore, the velocity input to the feedforward controller is defined in Eqs. (5.21)-(5.23) as follows:

$$u_{\mathrm{ff}} = v_{\mathrm{x}} + U - U_{\mathrm{sp}}, \tag{5.21}$$

$$v_{\mathrm{ff}} = v_{\mathrm{y}} + V - V_{\mathrm{sp}}, \tag{5.22}$$

$$w_{\mathrm{ff}} = u_{\mathrm{ff}} \tan\theta \cos\phi - v_{\mathrm{ff}} \tan\phi, \tag{5.23}$$

where U and V are the horizontal velocities of the quadrotor obtained by taking derivative of the positions recorded by the motion capture system. Also, U_{SP} and V_{SP} are the setpoint horizontal velocities assigned by the target trajectory. Thus, u_{ff}, v_{ff} and w_{ff} can replace v_{x},

v_y and v_z respectively in Eqs. (5.17)-(5.20). As indicated before, the reference roll and pitch angles (ϕ_{ref} and θ_{ref}) are the physical steady solutions to quadrotor attitude subject to a crosswind wind. These two reference values are directly added to the inner-loop attitude PD control outputs.

Also, the reference required thrust (T_{ref}) should be used in altitude control to replace the assumed constant hover throttle. That is, T_{ref} is firstly mapped to a RPM condition using HBEM model. Then, the RPM condition is converted to throttle using the RPM-Throttle model introduced in Section 4.4.1.

5.4 Wind Sensor

Wind sensors are usually mounted on a stationary object due to weight considerations. Also, they do not often measure the wind velocity in all the three directions. The HBEM and RIPF models require the wind information in both horizontal and vertical directions. Also, a wind sensor with minimal weight is desired to be mounted on the quadrotor.

The TriSonica™ Mini Wind and Weather Sensor (shown in Fig.5.8) is selected by evaluating different available sensors in the market. The TriSonica sensor uses ultra sound technology and measures the wind speed in the three directions with a limited measurement capability in the vertical direction.

Manufacturing specifications for accuracy and characteristics of the wind sensor are shown in Table 5.6.

Table 5.6: TriSonica™ Mini Wind and Weather Sensor manufacturer specifications.

	Wind Speed	Wind Direction
Range	0-50 m/s	For x and y: 0-360, For z: ±30°
Resolution	For 0-10 m/s: 0.1 m/s	1.0°
Accuracy	For 0-10 m/s: ±0.1 m/s	±1.0°

Figure 5.8: Trisonica Mini wind sensor.

The sensor weight is 50 grams. Also, a low-weight support was designed and 3D printed to mount the sensor onboard. The wind sensor and its assembly are installed on the quadrotor (see Fig.5.10). The sensor is placed about 10 inches (25 cm) above the rotor plane to minimize the effect of the rotor inflow steam on the sensor.

BeagleBone Blue has an available UART port, and the sensor is connected to the BeagleBone using RS232 to TTL converter shown in Fig.5.9.

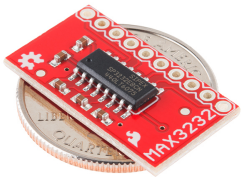

Figure 5.9: RS232 to TTL converter.

A snapshot of the experimental setup is shown in Fig. 5.10.

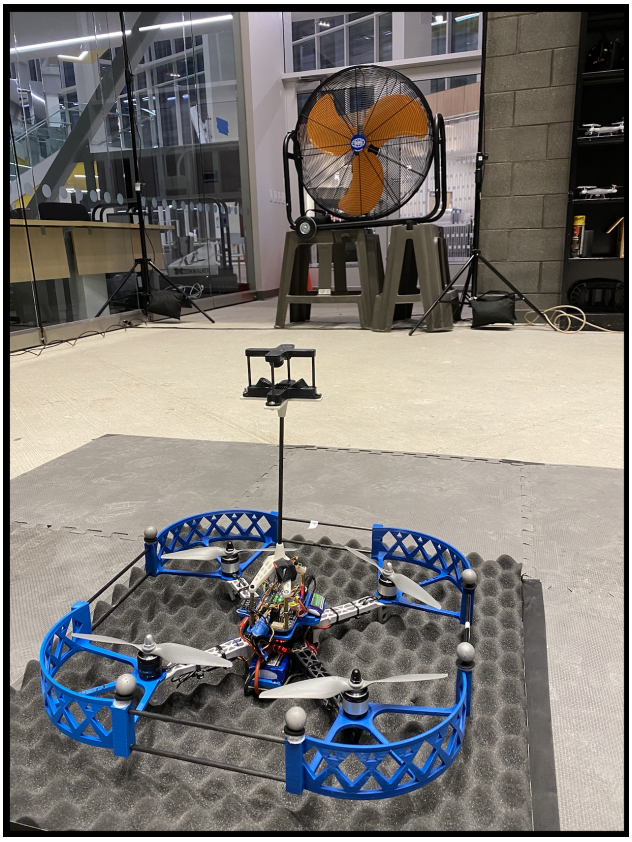

Figure 5.10: Wind sensor installed on the quadrotor.

5.5 RPM Sensor

The RPM condition and the blade pitch offer the two fundamental ways of controlling the thrust output of a propeller-based aircraft. In fixed wing aircraft, the pitch and RPM can both be controlled allowing for a wide range of control and fine-tuning for the desired thrust. In helicopters, the pitch of the blades is controlled both cyclically and collectively. On small quadrotors, the pitch is often fixed which limits thrust to be controlled only through the RPM of the motors. Quadrotors have relied on EMF information coming from the motors and Electronic Speed Controllers (ESC)s to estimate the RPMs.

The quadrotor is equipped with RPM sensors to collect accurate RPM data. The result of this sensor modification allows for more accurate RPM measurements, paving way towards a better understanding of the propulsion system onboard a quadrotor. Physical RPM

data can significantly assist the available aerodynamic models in flight simulation.

The sensors consist of a set of IR sources and light detection sensors on a single chip. The light detection sensors pick up reflected light from the IR sources and send pulses when they detect a change in reflection. Reflective tape is added onto portions of the motors such that the sensor can detect the operation of the motors. A picture of the RPM sensor in close proximity of the motor is shown in Fig. 5.12.

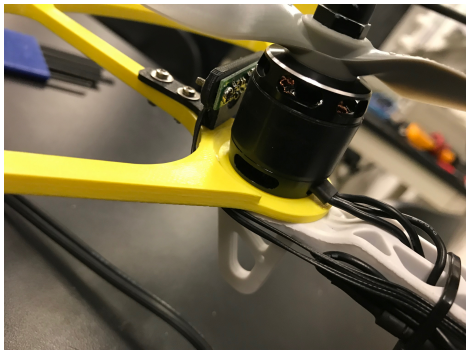

Figure 5.11: RPM sensor mounted on quadrotor.

Several modifications are made to the existing chip with the source and detectors. Fig. 5.12 shows the two 100kΩ resistors that are disconnected from the board to lower the voltage required to trigger the detectors. This is to increase the sensitivity of the sensors as the stock sensors could not pick up the reflected light from the motors. Additionally, encoder input ports on the BeagleBone Blue required modification to accept data from the RPM sensor. With these modifications, the sensors are able to record the motors speed up to 10,000 RPM.

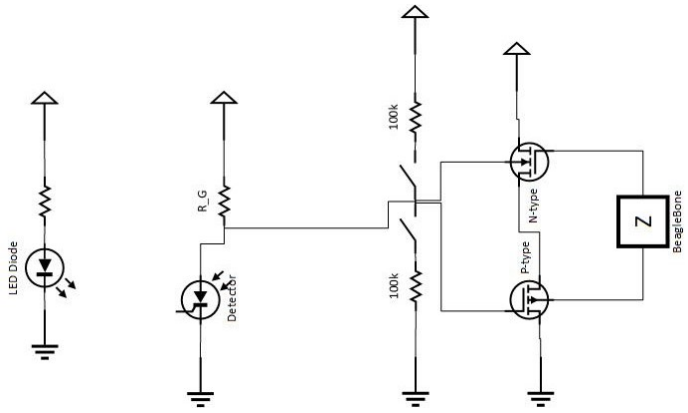

Figure 5.12: Circuit diagram of the RPM sensor.

5.5.1 RPM Sensor Measurements

A cross trajectory is designed, and the quadrotor performed an autonomous flight over it to test the RPM sensors. The trajectory was tracked well as seen by the nominal and actual horizontal position of the quadrotor in Fig. 5.13.

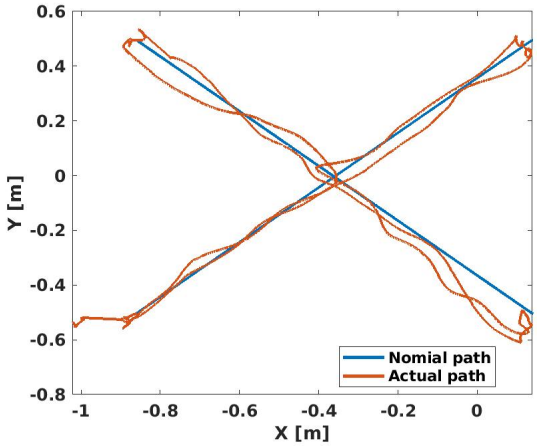

Figure 5.13: Cross path position during flight.

The RPM data is also collected by counting the number of revolutions during the flight using the optic RPM sensors. It should be noted that there is an offset between each rotor RPM even in hover condition. This is due to the fact that there exist unsymmetrical factors in the systems leading to the offset between the rotational speeds of the respective rotors.

The sampling frequency is 200 Hz, and the RPM during flight is about 7000 RPM (or 120 rev/seconds). The data has been averaged at a rate of 4 Hz which is about measuring RPM every thirty revolutions (equivalent to every 0.25 seconds). RPM data is shown in Fig. 5.14 for the cross path trajectory.

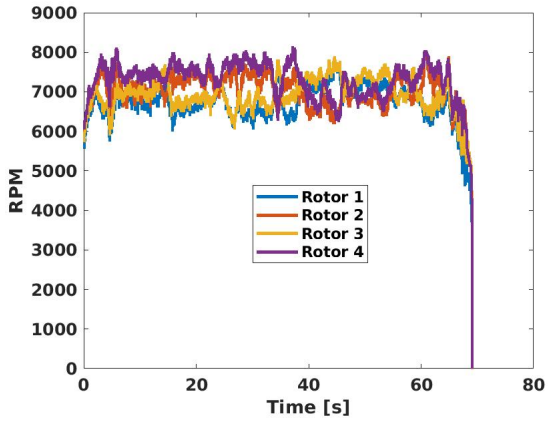

Figure 5.14: Cross path RPM data during flight.

CHAPTER 6

Autonomous Flight Testing

In this chapter, integrability, capability, and usability of the models such as HBEM, RIPF (see Chapter 4) and the feedforward controller (see Section 5.3) are investigated in autonomous flight tests. These models are implemented onboard the quadrotor introduced in Chapter 5. An industrial axial fan with diameter of 3-ft is used to simulate harsh environmental conditions in an indoor testing facility.

Compatible and efficient C codes were developed to be executed on the onboard flight software. Appropriate C libraries suited for BeagleBone Blue processor (ARM® Cortex-A8 processor) and efficient coding algorithms increased the efficiency and reduced real-time run of the codes onboard by a factor of 10.

Flight tests were conducted for two modes, namely: *Autonomous*, and *Sensed Autonomous* flight modes. *Autonomous* mode refers to the flight mode in which only a feedback controller (see section 5.2.2) for position control is used. *Sensed Autonomous* refers to the flight mode in which a feedforward controller is used along with the position feedback controller.

The experimental setup is described, and a desired trajectory is defined. Firstly, flight test results in the no-crosswind environmental condition (fan-off) are presented. Following the fan-off flight tests, results for flying in extreme environmental conditions (fan-on) are presented, and they are compared with the no-crosswind results thereof.

6.1 Experimental Setup

Flight tests were conducted in the Robotics Fly Lab (RFL) located in the Ford Robotics Building (FRB) of the University of Michigan. RFL is an indoor facility that is equipped with a motion capture system. An axial fan with a diameter of 36 in ($\approx 0.91m$) is used to simulate an extreme environmental condition. A picture of the quadrotor in the test setup is shown in Fig. 5.10. A schematic of the RFL is shown in Fig. 6.1.

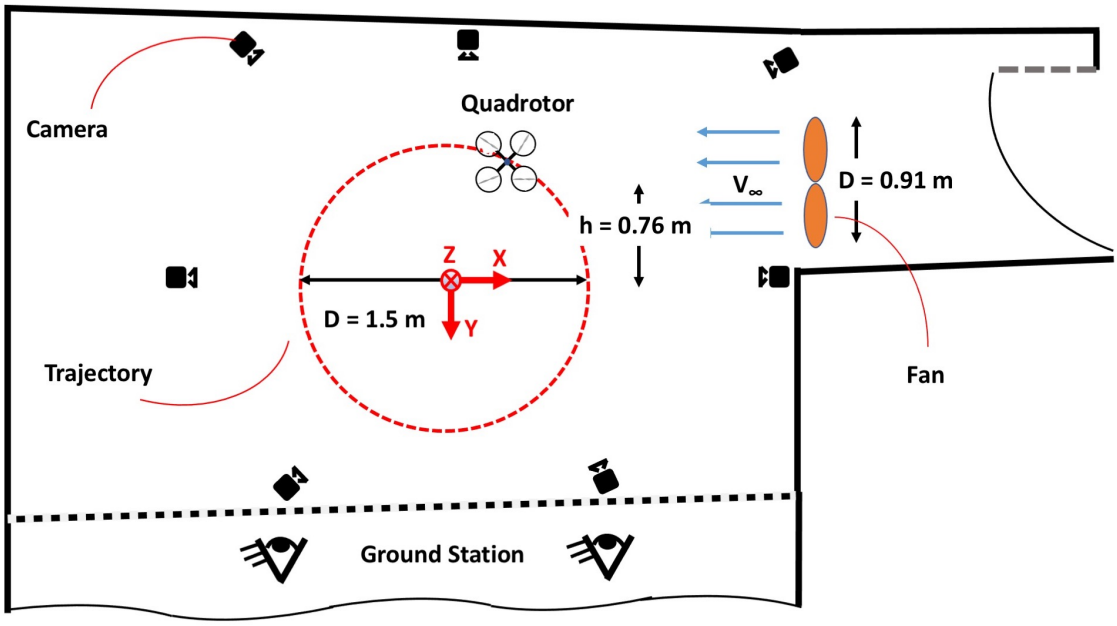

Figure 6.1: Robotics Fly Lab experimental setup.

Flight tests are conducted for two distinct environmental conditions. In the first condition, the quadrotor is flown in a no-crosswind condition in the RFL. In the second condition, the fan is turned on and generates a strong turbulent crosswind up to 5m/s for approximately half of a circular trajectory. As shown in Fig. 6.1, seven cameras are used to track the motion of the quadrotor. It is noted that multiple autonomous and manual flight tests were conducted to tune the PD gains for attitude, altitude and position feedback controls.

6.1.1 Trajectory Specification

A circular trajectory with a diameter $D_{\text{t}} = 1.5\ m$ is designed. The trajectory contains the following segments:

1. Take off from the ground to an altitude of $h_{\text{sp}} = 1.1$ m with a constant speed in 4 seconds
2. Hover for 1 second
3. Move from the center of the circle to its perimeter with a constant speed in $0.167D_{\text{t}}/V_{\text{t}}$ seconds
4. Hover for 1 second
5. Accelerate clock-wise linearly to the cruise speed of $V_{\text{t}} = 0.5$ m/s over span of one full circle
6. Fly with the cruise speed over one full circle in a clock-wise direction
7. Reverse Step 5 to 1 which is to decelerate and make a stop, hover, move back to center of the circle, hover and land.

Therefore, three full circles are tracked at the setpoint altitude. For the remainder of this dissertation, all plots that are function of time include 4 vertical lines in between which these three circles are enclosed.

6.2 Considerations Regarding The Wind Sensor and Sensed Autonomous Flight Mode

There are a few observations made about the sensor that need to be addressed before presenting the *Sensed Autonomous* mode results. The wind sensor, despite being very light, did

not perform as described by the manufacturer. The sensor outputs were often very noisy. It has also different sensitivity for different wind directions. The sensor measurements were different for mean velocity and fluctuations in the x and y directions when the sensor was exposed to the same flow-field and placed in the corresponding orientations with respect to the wind direction.

Moreover, the z-velocity is not measured properly. Given that it is a safe assumption that the flow field made by the fan is mostly horizontal, Eq.(5.23) as an approximation to vertical velocity can instead be used. To mitigate the impact of velocity data fluctuations, averaging is required. It is noted that when the velocity is noisy, that will affect the reference Euler angles and thrust values (see Eqs. 5.17-5.18) and leads to instability. However, averaging comes at a cost:

- Slower response rate
- Time delay

The maximum sensor output rate is nominally 40 Hz, however, the sensor output rate was set to 5 Hz from the sensor internal software that corresponds to a sample of size 8. Also, in order to further smooth out the velocity inputs to the feedforward controller, a moving average is applied to Eqs.(5.21)-(5.23) with a window size of 5 samples, and that causes a time delay of $1 - 1.5$ seconds to the velocity information stream.

Another consideration is the fact that - despite the fan having a 3 ft diameter, there is no guarantee the sensor and quadrotor (i.e. rotors) are exposed to the same flow field. It is noted that the largest turbulent eddies may not be as large enough to impinge on the sensor and quadrotor simultaneously (see Fig. 5.10).

6.3 Flight in Still Air

PD gains are tuned for attitude, altitude and position controls, and they are reported in Tables 5.3, 5.5 and 5.4. The quadrotor autonomously followed the circular path with a

diameter of 1.5 m. It is noted that the yaw angle (ψ) is an independent state variable that can be arbitrarily set and held during an autonomous mission. The heading angle was set to $\psi = 0$ for the entire flight envelop.

In the absence of the fan operation, there is no nominal external flow field in the test area. However, it is noted that the the rotors generate a small random turbulent field around and underneath of the quadrotor.

6.3.1 Autonomous Mode

The quadrotor was confirmed to successfully execute the designed trajectory. The Euler angles are shown in Figs.6.2-6.4. The Euler angles vary between -4 and 4 degrees that shows the trajectory is followed effectively.

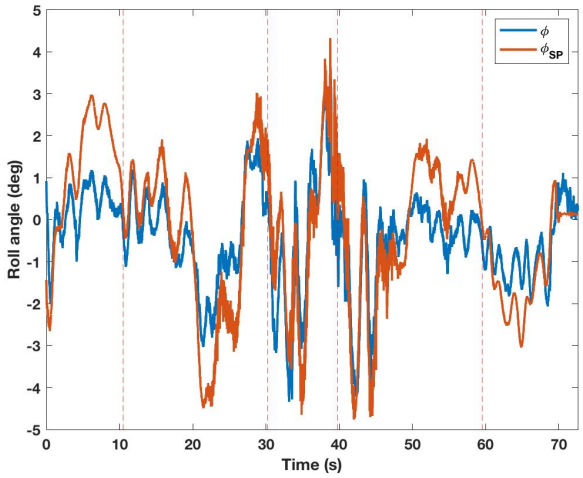

Figure 6.2: Roll angle tracking in *Autonomous* flight mode.

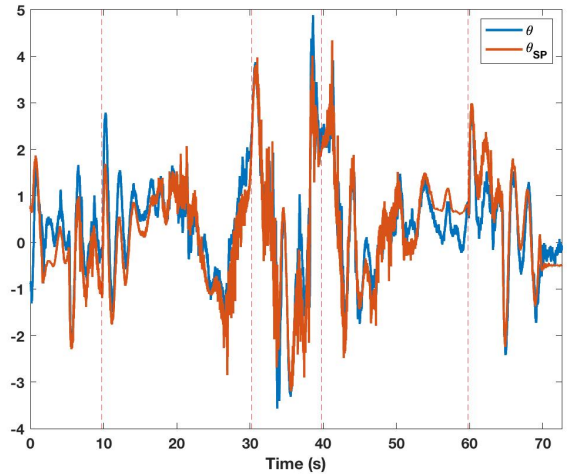

Figure 6.3: Pitch angle tracking in *Autonomous* flight mode.

As shown in Fig. 6.4, the yaw angle (heading) is well-tracked to the desired value of zero, $\psi_{\text{sp}} = 0$ except in the take-off phase in which the ground effect is strong. Also, the roll and especially pitch angles are tracked adequately, and the roll angle is about 90 degrees delayed with respect to the pitch angle. Larger gains could be used to make the tracking more aggressive, however, that could lead to more instability and therefore a less smooth flight.

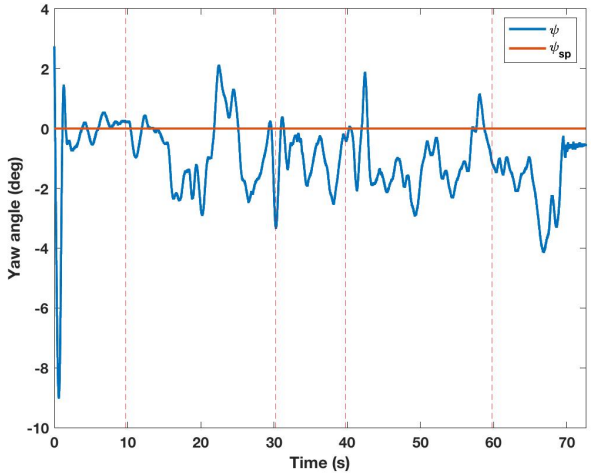

Figure 6.4: Yaw angle tracking in *Autonomous* flight mode.

The throttle values are shown in Fig. 6.5 for all rotors. It is evident that as flight speed

increases, both throttle values and their changes with respect to time also increase so that the quadrotor can catch up with the desired trajectory.

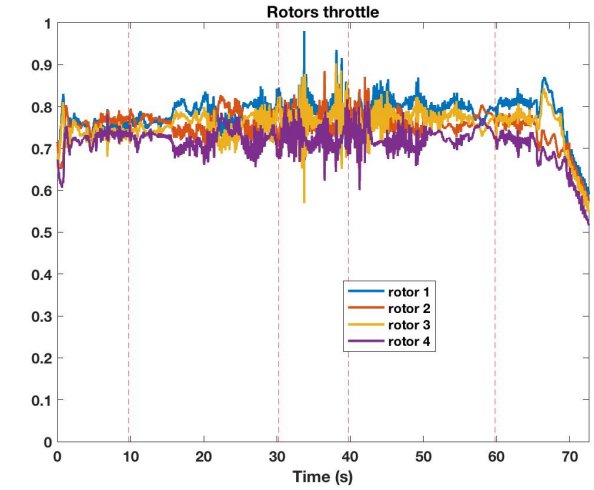

Figure 6.5: Throttle values in *Autonomous* flight mode.

The control outputs for altitude, roll and pitch (i.e., U_{z}, U_{roll} and U_{pitch}) are demonstrated in Fig. 6.6. As observed, the roll control output has a negative offset that is added manually to account for physical asymmetries on the quadrotor. The asymmetry can come from weight imbalance or discrepancies in motors thrust output. The added offset is -0.055.

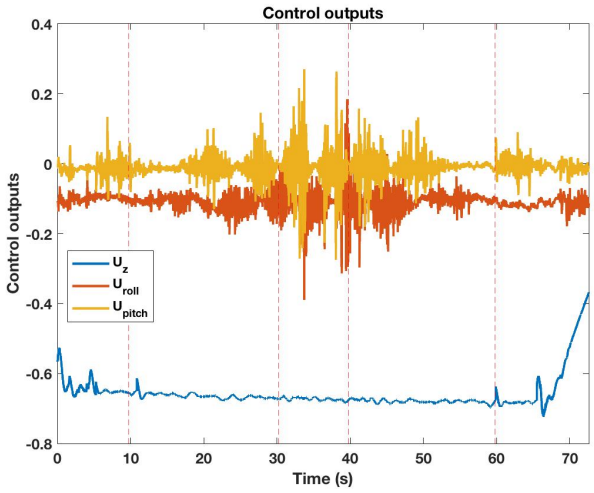

Figure 6.6: Control outputs in *Autonomous* flight mode.

The position tracking is depicted in Fig. 6.7. As noted, the planned trajectory is tracked

very well over the majority of the designed path. The maximum discrepancy between the target and actual trajectories is about 0.15 m, and occurs when $X = 0$ and Y is at its maximum.

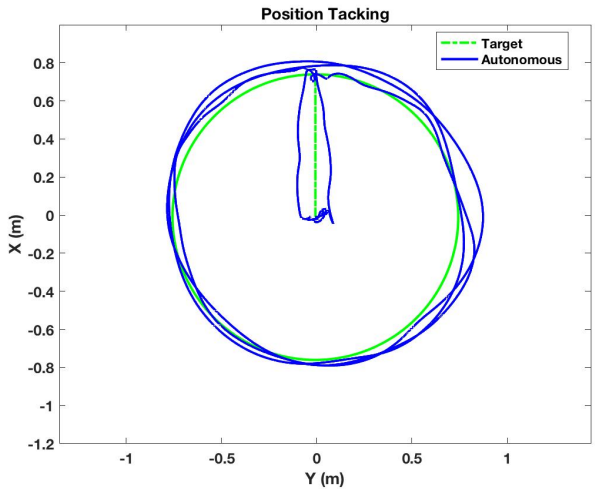

Figure 6.7: Trajectory tracking in *Autonomous* flight mode.

The position of the quadrotor as a function of time is illustrated in Fig. 6.6. It is noted that the altitude tracking has a constant offset. This can be due to the fact that either the hover throttle is not large enough, or the battery onboard was not fully charged during the flight to sufficiently power up the motors. Also, increasing the altitude PD gains may remedy the Z-position error.

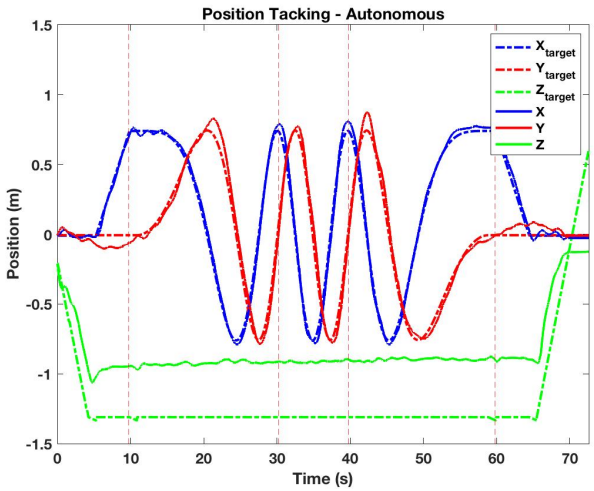

Figure 6.8: Position tracking in *Autonomous* flight mode.

In this study, velocity control was not performed. However, it is instructive to compare the target trajectory velocities (U_{SP} and V_{SP}) versus the actual quadrotor velocities (U and V). The velocity of the quadrotor is obtained by taking its position derivative with respect to time.

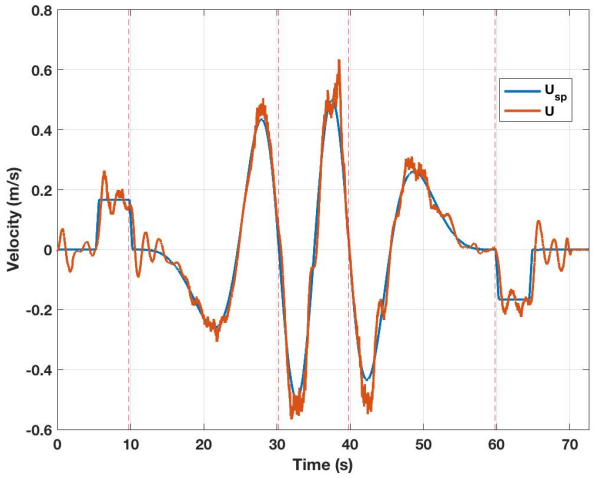

Figure 6.9: V velocity tracking in *Autonomous* flight mode.

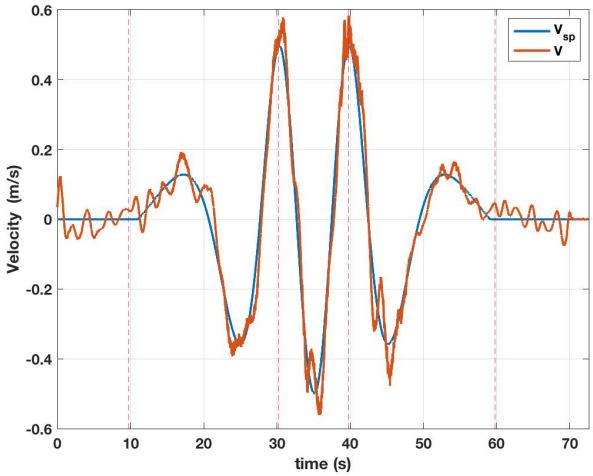

Figure 6.10: U velocity tracking in *Autonomous* flight mode.

As noted in Figs. 6.9 and 6.10, the U and V velocities are tracked very well with a maximum error of 0.1 m/s.

6.3.2 Sensed Autonomous Mode

In this mode, the wind sensor outputs are directly used in the physics-based models, and subsequently in the feedforward controller. The feedforward controller is designed based on a steady-state cruise condition, whereas in the design circular trajectory, the quadrotor is constantly under radial acceleration and mostly under tangential acceleration.

The velocity tracking results are shown in Figs. 6.11 and 6.12 to better understand how accurately the wind sensor measures the relative wind velocity. In the absence of external crosswind, the relative wind velocity should have the same magnitude as the quadrotor speed.

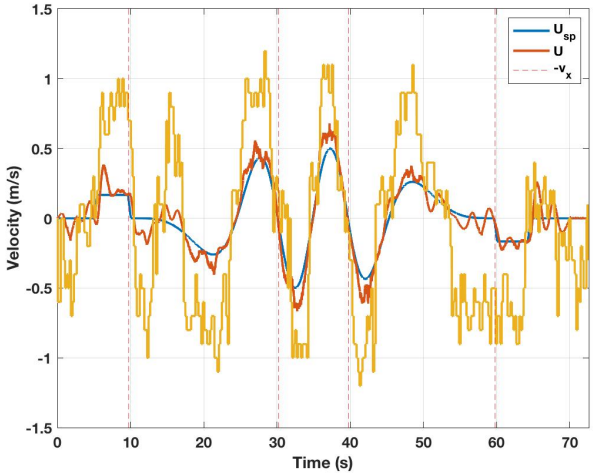

Figure 6.11: U velocity tracking in *Sensed Autonomous* flight mode.

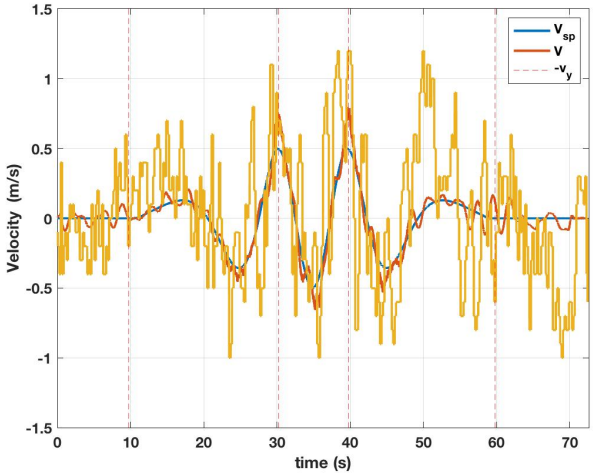

Figure 6.12: V velocity tracking in *Sensed Autonomous* flight mode.

As noted in Figs. 6.11 and 6.12, the wind sensor outputs are not accurate, and there exists large fluctuations even after averaging with a window size of 8 consecutive measurements. Also, the sensitivity of the sensor is different for X and Y directions given than there are more fluctuations in v (see Fig. 6.12) than u velocity component (see Fig. 6.11).

Next, Euler angles tracking is presented in Figs. 6.13-6.15. Firstly, it is evident that the heading angle (Yaw) is well maintained at its setpoint value with a maximum error of 3.5 degrees.

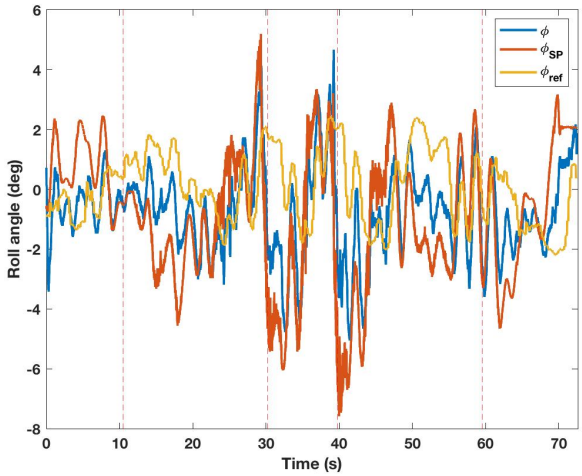

Figure 6.13: Roll angle tracking in *Sensed Autonomous* flight mode.

In Figs 6.13 and 6.14, three different variables are shown. Firstly, the quadrotor Euler angles (roll and pitch). Secondly, the setpoint Euler angles originated from feedback position control, and thirdly, the reference Euler angles that are the solutions to the quasi-steady force equilibrium problem where the quadrotor is subject to a instantaneous relative wind (see Section 5.3).

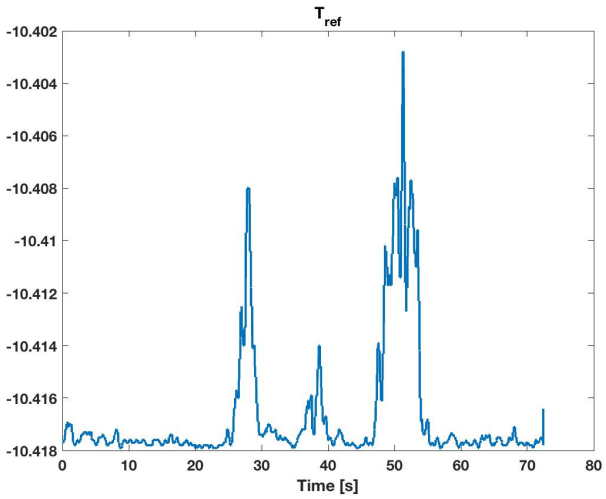

Figure 6.14: Pitch angle tracking in *Sensed Autonomous* flight mode.

It is interesting to note that the reference Euler angles are periodic in the time range of $10s$ <time< $60s$. Closely examine - for instance - the reference pitch angle, in the range of

$30s$ <time< $40s$ which is the cruise phase of the flight over one full circle. At $t \approx 30s$, the quadrotor is at top of the circular trajectory (see Fig. 6.18, $Y = 0$ and X at its max), and the reference pitch angle is zero ($\theta_{ref} \approx 0$)which is the correct physical solution. As the quadrotor moves clockwise (to the right) towards $X = 0$ and Y at its max, the reference pitch angle reaches to its positive maximum at $\approx 32.5s$ which is physically expected since the U-velocity is negative and its absolute value is maximum.

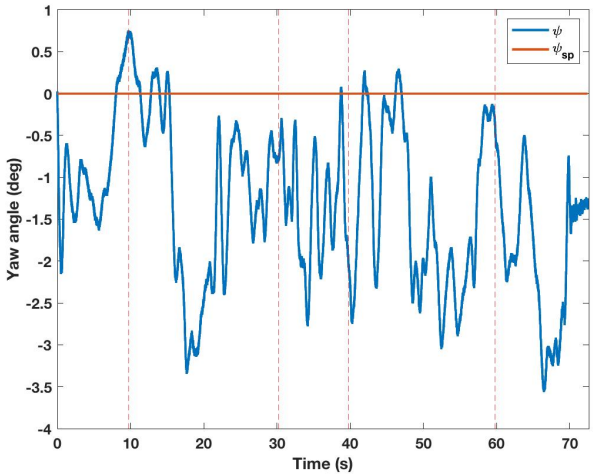

Figure 6.15: Yaw angle tracking in *Sensed Autonomous* flight mode.

A valid question is that why the actual quadrotor Euler angles are different and have a time delay with respect to the reference Euler angles. It is instructive to imagine a scenario: if the quadrotor only uses the feedforward controller and follows the reference Euler angles, it would keep adding to its tangential speed, and would follow a widening outward spiral trajectory. Therefore, the position feedback control kicks in and restrains the widening spiral motion that overall led to a phase shift of the onboard Euler angles with respect to the reference Euler angles.

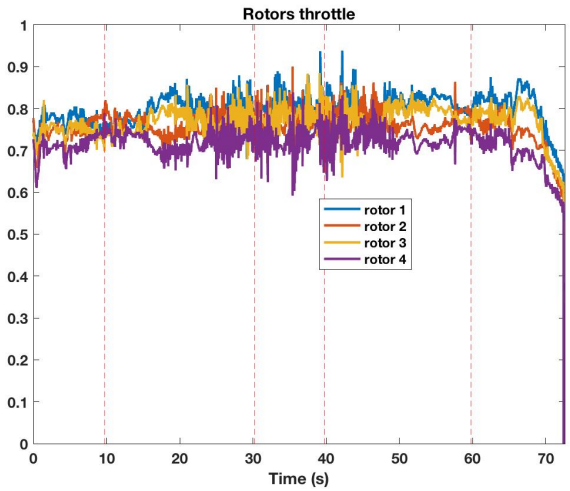

Figure 6.16: Throttle values in *Sensed Autonomous* flight mode.

Throttle values and control outputs are shown in Figs. 6.16 and 6.17. Similar trends in the results are observed to those of the *Autonomous* flight mode.

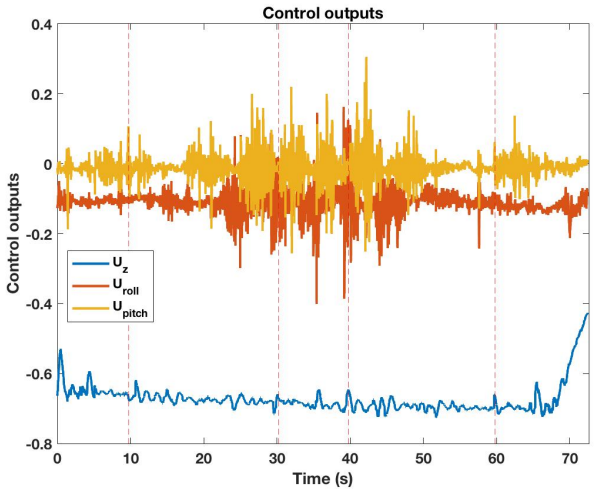

Figure 6.17: Control outputs in *Sensed Autonomous* flight mode.

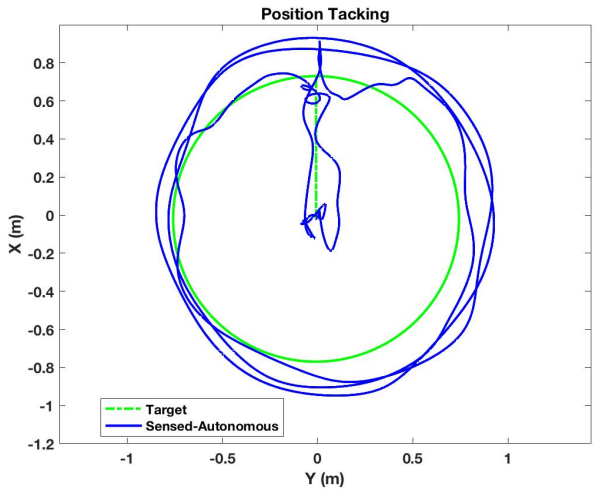

Figure 6.18: Trajectory in *Sensed Autonomous* flight mode.

As expected and shown in 6.18, the resultant trajectory has a larger diameter compared to the target. This is due to the fact that feedforward controller reinforces the tangential motion of the quadrotor (for every azimuth angle), leading to a growing tangential velocity compared to the setpoint velocity values. It is noted that the feedforward controller has no ”knowledge” of the planned circular path, and therefore does not produce reference angles necessary to provide a centrifugal (i.e., radial) acceleration.

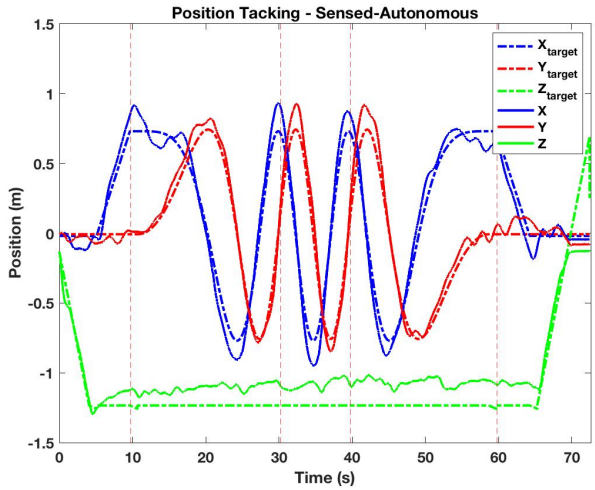

Figure 6.19: Position tracking in *Sensed Autonomous* flight mode.

The position tracking for all directions is shown in Fig. 6.19. The maximum error in

X and Y is about 0.2 m. Also, the altitude is tracked very well, and in fact better than the *Autonomous* mode. It is reminded that in the altitude controller, the $hover_{\text{throttle}}$ (see section 5.2.2.1) is obtained using the HBEM model as described in Section 5.3.1.

6.4 Flight in Extreme Crosswind

As the fan is switched on, a strong crosswind roughly impinges the quadrotor and wind sensor with the same intensity during the flight given the large diameter of the fan (3ft). The flow around the quadrotor is highly turbulent, and the turbulent crosswind has a magnitude of approximately 5 m/s as measured by the wind sensor. It is noted that the quadrotor is in a headwind condition given the wind blows against the direction of flight.

6.4.1 Autonomous Mode

A strong crosswind is made by the fan that has a direct impact on approximately half of the circular trajectory. Given the turbulent nature of the flow field, attitude control is very challenging as shown in Figs. 6.20-6.22.

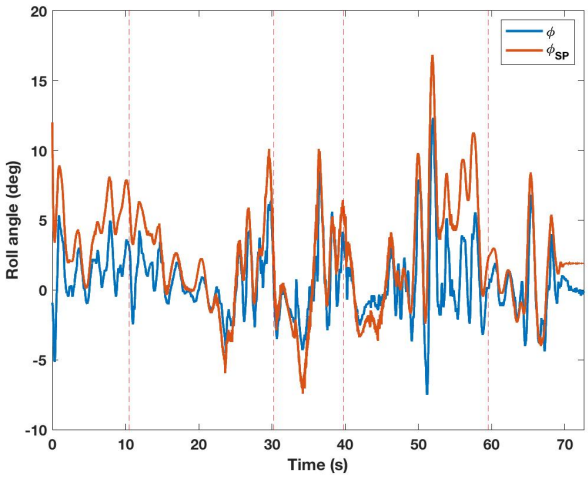

Figure 6.20: Roll angle tracking in *Autonomous* flight mode.

The large negative peaks in setpoint pitch angle (see Fig. 6.21) are indicative of the

flight phases where the quadrotor is subject to the strong crosswind provided by the fan. Also, as shown in Fig. 6.20, the roll angle fluctuates, corresponding to side-to-side motions.

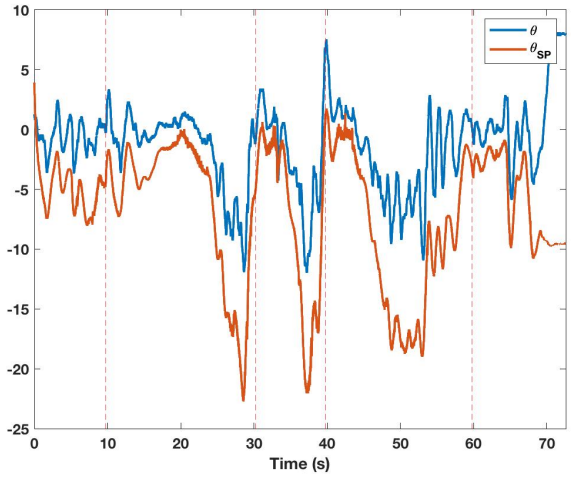

Figure 6.21: Pitch angle tracking in *Autonomous* flight mode.

As depicted in Fig. 6.22, tracking the setpoint yaw angle is very challenging especially when the quadrotor is entering/leaving the crosswind zone due to fact that an external Z-moment is exerted on the vehicle when only a portion of the quadrotor is being exposed the wind.

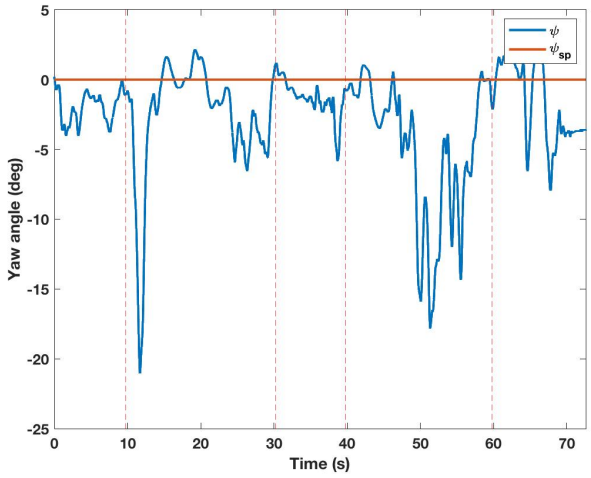

Figure 6.22: Yaw angle tracking in *Autonomous* flight mode.

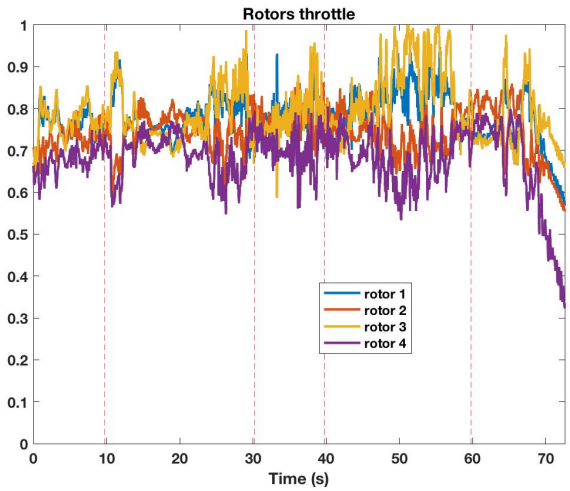

Figure 6.23: Throttle values in *Autonomous* flight mode.

Next, the throttle values and control outputs are shown in Figs. 6.23 and 6.24. As noted, the throttle level is at maximum (> 0.9) to move through the adverse wind. It should be mentioned that, for the electric motors used in this study, the throttle values of 0.9 and 1 approximately generate the same amount of thrust if not identical. It is evident that the control outputs are larger comparing to the no-wind condition data of Fig. 6.6.

One important observation is that when throttle saturation occurs, that can affect roll and pitch control given that motors are working at full capacity.

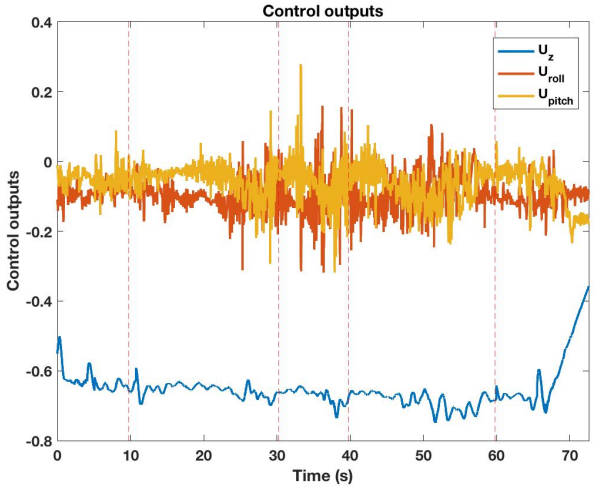

Figure 6.24: Control outputs in *Autonomous* flight mode.

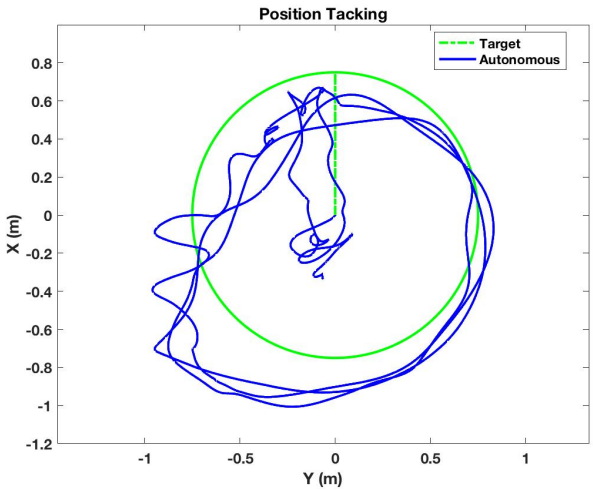

Figure 6.25: Trajectory tracking in *Autonomous* flight mode.

The trajectory tracking results are shown in Fig. 6.25. As observed, in the left half of the circular trajectory ($Y < 0$), that is impacted by the crosswind, the tracking error is at its maximum (≈ 0.5m). Next, the position of the quadrotor along with the target position is shown in Fig. 6.26. There are altitude dropouts where the quadrotor is impinged by the crosswind. As mentioned before, in that phase of flight, motors are running almost at their maximum capacity, and also the quadrotor is tilted (large pitch angle). Thus, the upward lift force is slightly reduced that leads to the dropouts.

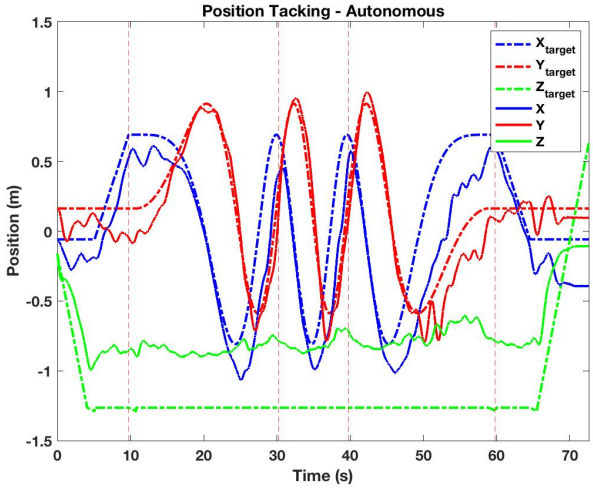

Figure 6.26: Position tracking in *Autonomous* flight mode.

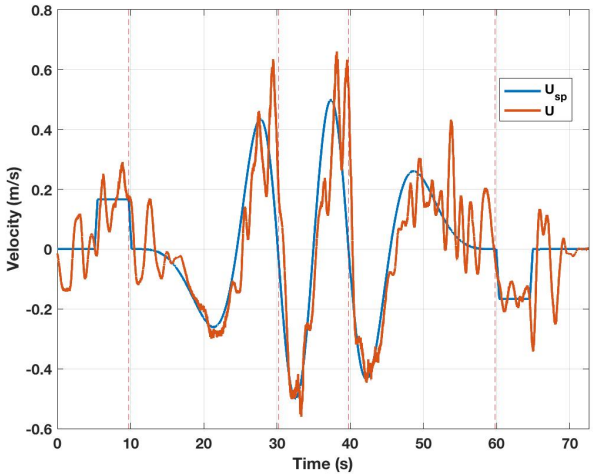

Figure 6.27: V velocity tracking in *Autonomous* flight mode.

The velocities of the quadrotor comparing to those of target are shown in Figs. 6.27 and 6.28. Similar to other state variables discussed above, where the extreme condition exists, the error is larger.

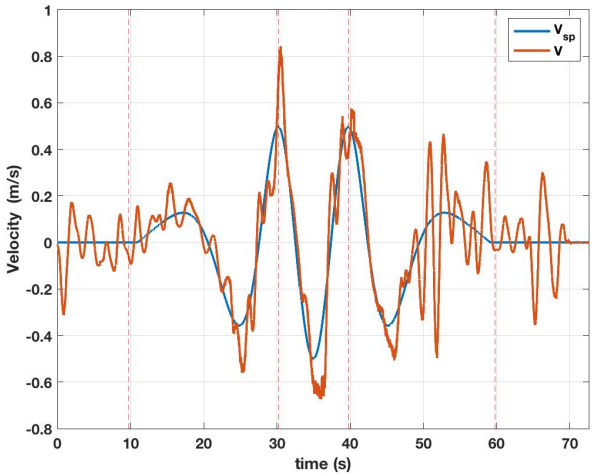

Figure 6.28: U velocity tracking in *Autonomous* flight mode.

6.4.2 Sensed Autonomous Mode

In this mode, near to the very end of the flight, motion capture system lost the location of the quadrotor due to a momentarily delay in position data streaming, and flight was

unexpectedly terminated just before landing phase. Therefore, the flight duration is slightly shorter for this flight mode than the others in this dissertation.

To better understand the flow field, the velocity of the quadrotor along with the wind sensor-measured velocity (multiplied by a negative) are shown in Figs. 6.29 and 6.30.

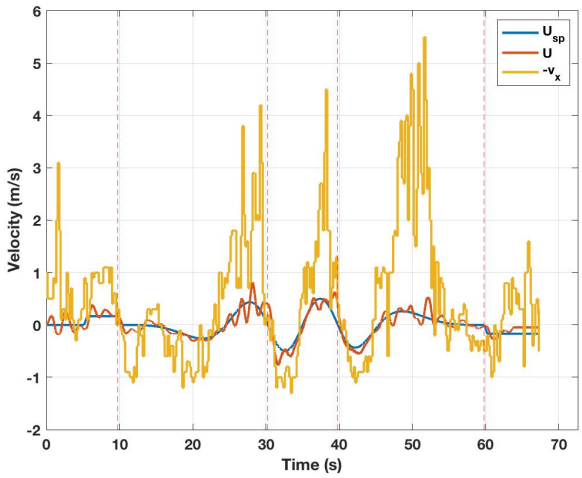

Figure 6.29: U-velocity tracking in *Sensed Autonomous* flight mode.

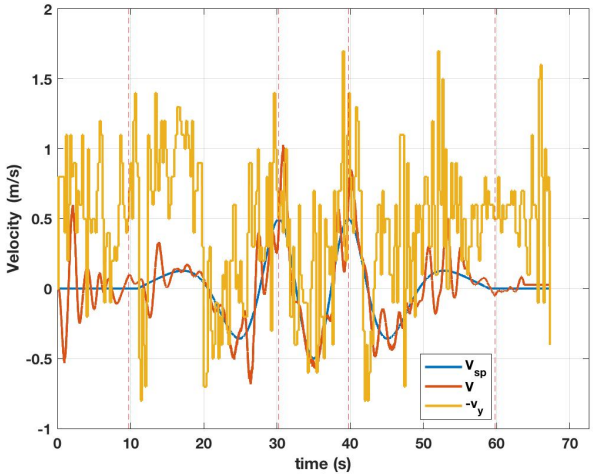

Figure 6.30: V-velocity tracking in *Sensed Autonomous* flight mode.

As noted, the maximum recorded velocity by the wind sensor in the X-direction is about 4 to 5.5 m/s. Also, strong fluctuations in both steam- and span-wise directions are observed.

Next, the onboard, setpoint (from position feedback controller) and reference Euler angles are shown in Figs. 6.31-6.33.

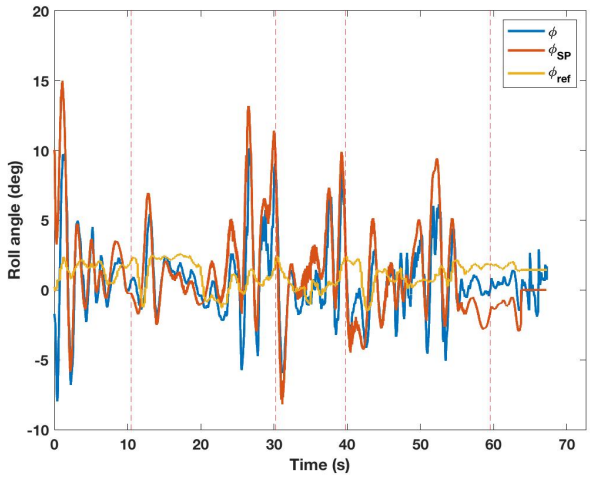

Figure 6.31: Roll angle tracking in *Sensed Autonomous* flight mode.

The reference roll angle is smaller compared to the reference pitch angle. Also, the setpoint roll (from position feedback controller) is the major contributor that determines the roll motion for this flight. Additionally, it is interesting to note that the reference pitch and onboard pitch angles are in good agreement in terms of magnitude.

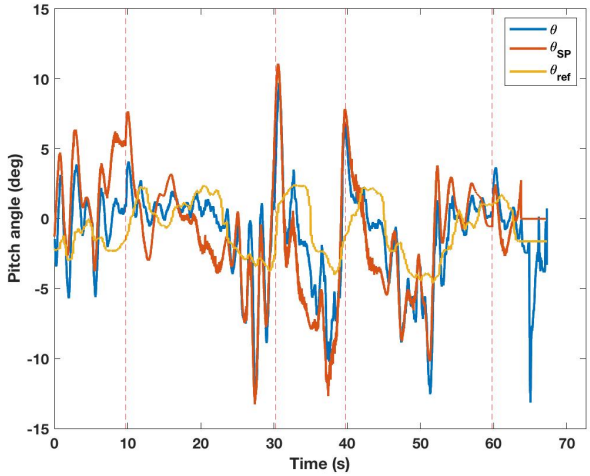

Figure 6.32: Pitch angle tracking in *Sensed Autonomous* flight mode.

Similar to the results presented earlier in *Autonomous* flight mode section, large nega-

tive yaw angles are observed in Fig. 6.33.

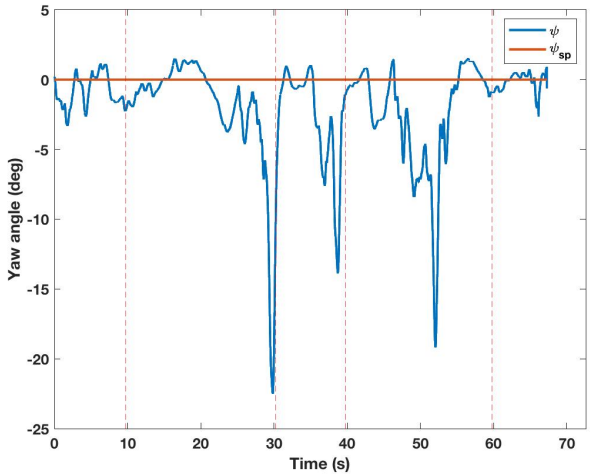

Figure 6.33: Yaw angle tracking in *Sensed Autonomous* flight mode.

As shown in Fig. 6.34, the throttle values indicate that motors are operating at their maximum capacity (where the adverse wind is present) to try to keep the quadrotor on the nominal path.

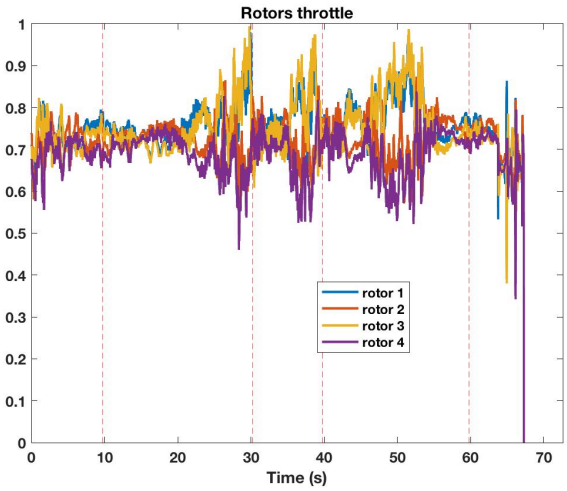

Figure 6.34: Throttle values in *Sensed Autonomous* flight mode.

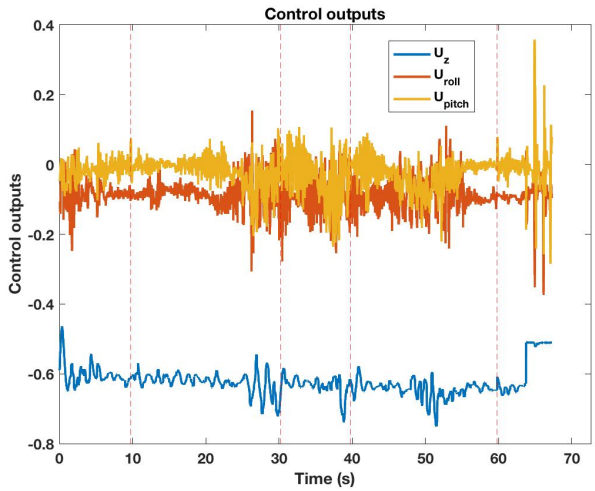

Figure 6.35: Control outputs in *Sensed Autonomous* flight mode.

Control outputs are shown in Fig. 6.34. It is observed that the altitude control output U_{Z} increases (where the crosswind is present) to keep the altitude constant, however, there are altitude dropouts (see Fig. 6.37) despite this effort.

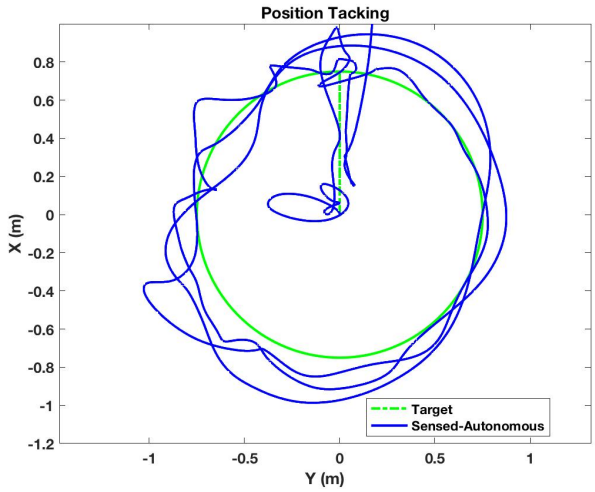

Figure 6.36: Trajectory tracking in *Sensed Autonomous* flight mode.

The actual versus nominal trajectories are depicted in Fig. 6.36. Overall, the target trajectory is followed adequately, in spite of the extreme environmental condition. For $Y > 0$, where it is less impacted by the fan stream, similar overshoots are evident, observed in Fig. 6.18. In the left half circle ($Y < 0$), where the feedforward controller is designed

for, position tracking is reasonable. Comparisons between the *Sensed Autonomous* ans *Autonomous* flight modes are made in the following section.

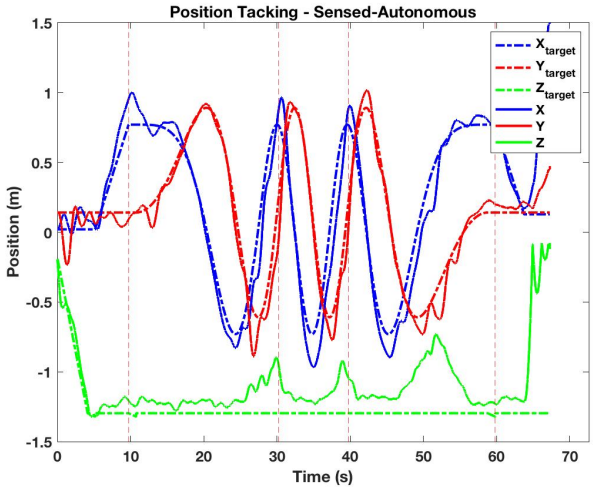

Figure 6.37: Position tracking in *Sensed Autonomous* flight mode.

6.4.3 Sensed Autonomous versus Autonomous Flight

Despite the challenges in incorporating the wind sensor to the *Sensed Autonomous* flight, a comparison between the two modes is made. First, the trajectories of the two flight modes are shown in Fig. 6.38. It is noted that the fan airflow is dominant for $Y < 0$ (left half-circle in Fig. 6.38) as the gust blows from $+X$ to $-X$ (from top to bottom).

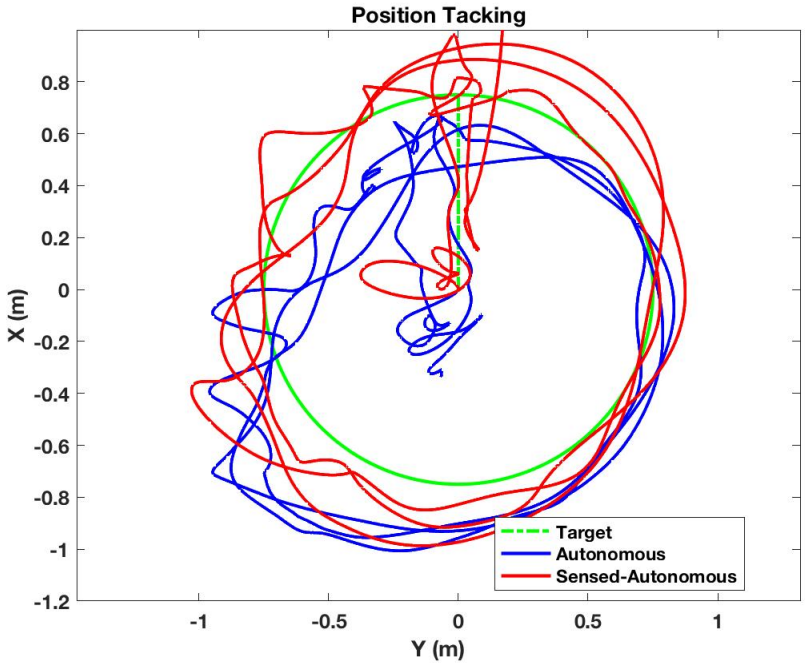

Figure 6.38: Trajectory tracking in *Sensed Autonomous* vs *Autonomous* flight mode.

As shown in Fig. 6.38, it is evident that the quadrotor maintains the target trajectory more accurately in the *Sensed Autonomous* mode compared to the *Autonomous* flight mode in the left half circle ($Y < 0$) where is subject to the extreme wind. Next, the position information as a function of time is shown in Figs. 6.39-6.41.

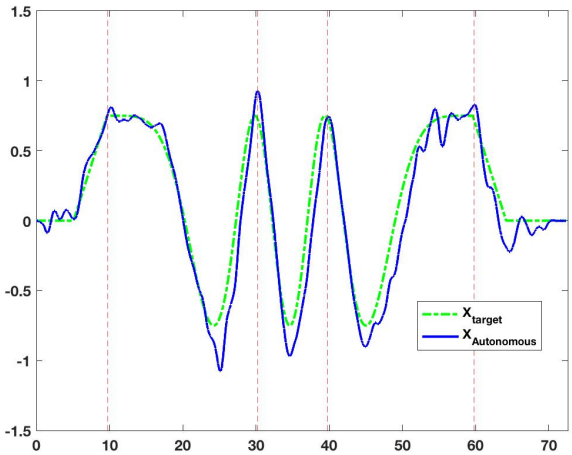

Figure 6.39: X-position tracking, *Sensed Autonomous* vs *Autonomous* flight mode.

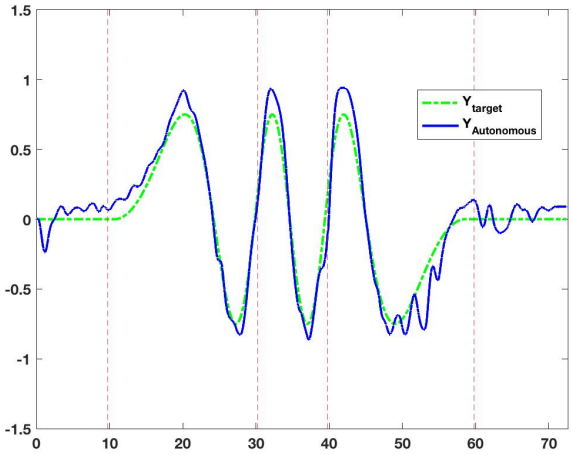

Figure 6.40: Y-position tracking, *Sensed Autonomous* vs *Autonomous* flight mode.

As noted in Figs.6.39 and 6.40, the position as a function time also reiterates the advantage of the *Sensed Autonomous* mode. Finally, the altitude of the quadrotor between the two modes are compared in Fig. 6.41.

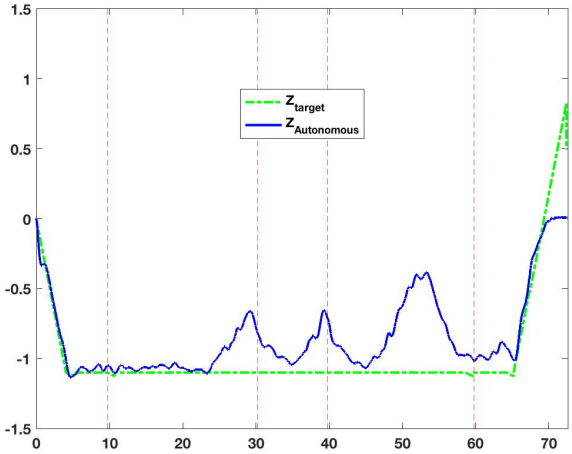

Figure 6.41: Z-position tracking, *Sensed Autonomous* vs *Autonomous* flight mode.

The altitude of the *Sensed Autonomous* mode is closer to target, however, three dropouts are observed which is indicative of losing upward lift due to tilting of the thrust vector corresponding the extreme pitch angle. Motion capture dropout in the *Sensed Autonomous* mode is evident at $t \approx 65s$.

CHAPTER 7

Summary and Conclusions

In this dissertation, physics-based models were developed for interactional aerodynamics, guidance and autonomous operation of rotary-wing UAVs. This includes vortex-based lifting surface models and newly developed rotor aeromechanic models (i.e., HBEM, RIPF, etc), and a feedforward controller. These models are self-contained and integrated in flight software. Additionally, a framework for performing accurate flight simulations of rotary-wing UAVs in realistic environmental conditions was developed. Flight simulations for specific missions were performed to illustrate the effect of modeling fidelity on the flight simulation outcomes. The above models were validated against experimental data and high-fidelity simulations. To evaluate the utility of these models in harsh environmental conditions, a custom quadrotor was built and equipped with wind and RPM sensors. Flight tests were conducted in and out of strong crosswind. The following sections summarize the major contributions:

7.1 Interactional Aerodynamics

The interaction of trailing vortices with lifting surfaces was studied using two levels of modeling fidelity. An overset mesh-based compressible RANS solver was chosen as the high-fidelity model (HFM). A lower-fidelity model (LFM) was developed by combining a vortex panel method with a propeller aerodynamic model and slipstream theory. Detailed

validations were pursued against data from three main experimental studies. Key observations from the studies are summarized below.

Wing-vortex Interaction:

- The HFM was used to model the vortex generator, vortex evolution and interaction with a downstream wing. The HFM accurately predicts wing airloads to within 2%, operating in a vortex wake of varying strengths. The predictions were found to be generally more accurate in the outboard sections and are found to deviate from the experiment near the wind tunnel wall. Inboard discrepancies are expected due to the presence of a wing slot opening in the experiment as well as the sensitivity of wing loading to flow fence size. The HFM accurately captured peak-to-peak values and the location of the incremental lift variation due to the presence of the trailing vortex from the generator wing. In addition, the vortex strength values, flow features, interaction of wing vortex with the incoming vortex (locations and relative positions of the vortices) and vortex wakeage effects on wing airloads were accurately predicted, including in the case where the vortex core directly impacted the wing surface. For cases of strong interaction, some discrepancies are noticeable inboard of the interaction. The HFM predicted the experimental wing surface pressure data to within a few % accuracy for all the cases considered.

- The LFM provided reasonably accurate predictions of the wing airloads for several horizontal and vertical locations of vortex wake with respect to the wing. The overprediction (of up to 10%) of the magnitude of the vortex-induced lift predictions in the case of strong interactions, is partially attributable to the fact that the vortex distortion is not modeled.

Isolated propeller:

- Both the HFM and LFM accurately represented the swirl angles in the propeller wake to within 1°. The HFM-predicted axial velocities in the wake are extremely accurate

outboard of the 0.8 R location. Inboard of this location, an under-prediction of about 5% is noticeable. The converse is true for the low-fidelity model.

- The HFM successfully captured a quadruple helix structure with slight contraction of the propeller vortex wake.

Wing mounted propeller:

- The helical wake vortex structure showed slight contraction before expanding upon its interaction with the wing in its wake and ultimately disintegrating downstream of the wing.

- The mean wing surface pressure was accurately predicted at several spanwise stations.

Qualitatively, it is shown that the low-fidelity model captures essential flow features and performance trends very well, although quantitative discrepancies were noticeable in comparison to the the RANS-based model and experiment. The level of agreement of the computational results with experimental measurements suggests that as long as the circulation is globally well-represented, both RANS-based and vortex-based methods are adequate in modeling vortex interactions with lifting surfaces.

7.2 Flight Simulation Framework for Quadrotors

A comprehensive suite of tools was introduced towards the end of performing realistic flight simulations for quadrotors. The focus is on operations in low-altitude atmospheric conditions, where turbulent gusts are expected to have a significant impact on the performance and stability of small unmanned aerial vehicles. Different fidelities of aeromechanical models for rotor performance of the quadrotors were discussed. The major accomplishments can be found in the list below:

- Large-eddy simulations (LES) were performed to accurately represent the atmospheric boundary layer (ABL). The canonical ABL used to generate the data in this study is modeled as a rough flat wall boundary layer with surface heating from solar radiation, forced by a geostrophic wind in the horizontal plane and solved in the rotational frame of reference fixed to the earth's surface.

- From the LES data, a reduced-order representation of the wind field was also constructed. Additionally, the Dryden turbulence model for wind velocity fluctuations was included as a benchmark wind model for comparison.

- The aerodynamics of the quadrotor was modeled using adaptations of blade element momentum theory. Models for thrust, drag and power of the quadrotor were integrated with the flight dynamics and wind models. A non-linear flight controller (backstepping controller) was developed to control all six degrees of freedom of the motion of the quadrotors.

- An ascent-straight-descent path and a circular path were designed for the simulations of the closed-loop system. These two trajectories were of interest due to the fact that they both incorporate a representative set of possible trajectories of a quadrotor. Representative results for flight parameters, required RPM inputs, resultant trajectory and power of the quadrotor for different aerodynamic and wind models and planned trajectories were obtained and compared against each other. A multiple cruise-speed trajectory phase was defined to determine the optimal cruise speed of the quadrotor.

- Discussions were presented regarding the region of validity of momentum theory. It was shown the momentum theory is approximately valid for the entire flight of a quadrotor except the landing phase.

Collectively, this study presented a suite of tools for realistic, flight simulations, and provides insight into the impact of modeling fidelity on trajectory planning and control.

The entire simulation suite is open-sourced for use by the community [1].

7.3 Rotor Aerodynamic Models in Forward Flight

A novel aerodynamic model was developed to estimate power, thrust, moments, and rotor in-plane force in real-time. These models were both implemented in flight simulation framework and also experimental quadrotor flight software.

Specifics of the research work carried out for advanced aeromechanical models are summarized as follows:

- A novel aerodynamic model-termed Hybrid Blade Element Momentum HBEM Model- is proposed for efficient and accurate predictions of rotor loads and moments for rotary wing UAVs.
- The HBEM model combines momentum and blade element theories with a linear inflow model in a consistent manner and can be executed in near-real-time. The key idea is to identify the integrated inflow velocity by seeking an agreement between momentum and blade element theories. The model is self-contained and the inputs to the model are geometry, aerodynamic properties of the blade and the flight condition
- To validate the HBEM model, a detailed set of experiments were performed in a wind tunnel. An 8 in diameter propeller was mounted in the wind tunnel, and the shaft angle was varied with respect to the incoming wind, and the thrust and in-plane forces are measured. The rotation rate of the propeller was measured using an optic sensor. Experimental data for a combination of wind tunnel speed and rotor angle of attack $\{V_\infty, \alpha_\mathrm{R}\}$ was obtained. The thrust as a function of advance ratio, climb ratio and RPM condition was compared against measurements for a wide range of configurations, and the HBEM model predictions were found to be in very good agreement with the experimental data.

[1] `https://github.com/behdad2018/FlightSim_QR_AIAA`

- The model is integrated with a 6 DoF flight dynamics module with a backstepping controller, and used to plan the trajectory of a typical quadrotor during a ascend-cruise-descend flight path. The RPM predictions from the HBEM model are compared with other aerodynamic models, namely; Radial inflow model and Simplified model. Flight simulation results indicate the importance of the aerodynamic model.

- In a more general setting, the HBEM model can be used in other rotating blade applications such as in horizontal axis wind turbines under yawed conditions. The source code is available for use by the community.

- Based on the aforementioned experimental study, a data-driven semi-empirical model for rotor in-plane force (RIPF) was constructed. This symbolic model estimates the RIPF as a function thrust (estimated by HBEM model), rotor angle of attack, relative wind velocity.

7.4 Experimental Quadrotor Controller and Sensor Design and Flight Tests

A custom quadrotor with a weight of 1080 grams was built and equipped with a state-of-the-art light-weight ultrasonic sensor for onboard wind velocity and RPM condition measurements. The quadrotor was programmed and physics-based models and a feedforward controller were implemented onboard. Autonomous light tests were conducted to illustrate that the aeromechanical models can run within quadrotor flight software. The following items are the key takeaways from the experimental quadrotor developments, programming and flight tests:

- Advanced rotor aerodynamic models of appropriate fidelity were successfully implemented on board a custom-built quadrotor. An ultrasonic wind sensor was installed approximately 10 inch above the rotor plane to measure the wind velocity. The 10

inch separation was deemed ”enough” to avoid the effects rotors inflow on the measured velocity.

- The run-time of the onboard physics-based codes was significantly reduced (by 10 order of magnitude) comparing to the initial generated codes by using the appropriate C libraries (suited for ARM® Cortex-A8), optimized compilation, and also modifying, and developing an efficient state-of-the-art non-linear solver algorithm.

- The velocity measurements made by the wind sensor were used for the purpose of quadrotor control.

- A feedforward controller was designed to leverage physics-based aeromechanical models into flight software. That is, the steady state solutions to Euler angles and required thrust are provided by the feedforward controller, and are directly sent to the motors along with the feedback outputs.

- A circular trajectory with a diameter of 1.5 m was defined in which the quadrotor reaches a cruise speed of 0.5 m/s. The quadrotor accelerates from to the cruise speed over one full revolution, stay on the circular trajectory during the second circle, and in the third circle, it decelerates to zero speed. A motion capture was used to obtain the location of the quadrotor during the flight.

- Flight tests were conducted for two modes, namely *Autonomous* and *Sensed Autonomous* modes. In the autonomous mode, only a PD feedback controller was used for position control. In the sensed autonomous mode, a feedforward controller was used to incorporate environmental conditions. An extreme environmental condition was simulated by an industrial axial fan was used to simulate an extreme turbulent gusts of up to 5m/s. Overall, the goal of the flight testing was to show that one can use physics-inspired models enabled by environmental sensor measurements especially in extreme wind conditions.

- It was illustrated that the use of the sensor to obtain wind velocities and the use of this information in the feedforward controller enhances the accuracy of trajectory tracking in extreme crosswind conditions.

7.5 Future Work

There is significant potential to improve and extend the scope of this dissertation and enable new generations of UAS by further bridging the gap between physics-based models and onboard decision-making. In this regard, the present work can be considered as proof-of-concept of some of the preliminary steps. The following items is a selective but not exhaustive list that can further be worked and improved upon.

- A more advanced flight simulation module can be developed in which both interactional and rotary-wing aeromechanical models are integrated and implemented. Thus, flight simulations in realistic atmospheric condition for a variety of advanced VTOL vehicles can be made.

- More challenging flow fields, such as in urban areas between tall towers can be obtained, and accurate flight simulations for fixed- and rotary-wing vehicles can conducted to further study the capability of such vehicles and their flight envelope.

- The PD feedback controller used onboard in this study can be improved upon. Feedback controllers that use Model Predictive Controller (MPC) may be better suited for flying under extreme environmental conditions.

- The HBEM model, while being a versatile model, is quasi-steady. Building unsteady rotor aerodynamic models, that can be executed in real-time is an interesting path to pursue.

- With a more accurate wind sensor with faster output rate, one can achieve better performance in the *Sensed Autonomous* flight tests. Also, more advanced feed-forward

controller models that can estimate an unsteady dynamic solution to the Euler angles can improve the stability and resilience in extreme wind conditions.

- In this dissertation, the autonomy relied on an indoor motion capture system. Using vision-based for position control of UAS is an ideal way where more aggressive and faster flight tests can be conducted outdoor to further show the benefits of physical sensors and physics-inspired models.

- In swarming operations of UAVs, one can enable UAVs to use aeromechanical models, onboard sensors in decision making to increase flight stability and noise reduction. Another interesting problem to explore is to optimize swarm flock formation patterns.

APPENDIX A

A.1 Evolution of Vortices

This section validates the high-fidelity model predictions of vortex evolution as well as vortex wake age effects against experimental data. Figure A.1 shows that the predicted vortex contours for the isolated wing compare qualitatively well with experiments. Figures A.2, A.3, A.4 demonstrate the evolution of vortex interaction from wing and VG for a nominal direct hit case for a VG placed at 58.5 inch from the wind tunnel side wall (0.5 chord inboard of wing tip). This is consistent with the observations in Figure 2.6, which detailed the interaction of the tip vortex of the wing with that from the VG, and the subsequent downstream roll-up.

Figure A.5 shows the effect of vortex wake age on wing loading. It is observed that, with increasing distance of VG, the strength of VG gradually decreases resulting in weaker spike in normal load near the vortex, further confirming the numerical accuracy of the CFD model.

A.2 Mesh Convergence on Propeller Study

To justify the choice of the grid resolution in the vortex core used in the present work, finer mesh results (axial velocity and swirl angles) are compared with that using the meshes

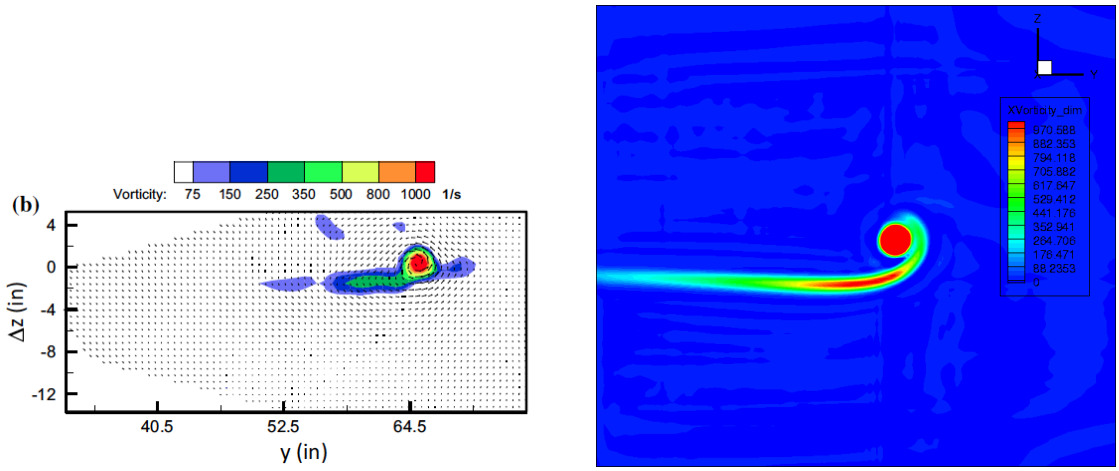

(a) Experiment [23] (b) CFD

Figure A.1: Comparing wing only vortex strength at 4 ft behind wing TE for $\alpha_{\mathbf{w}} = \mathbf{7}^{\circ}$.

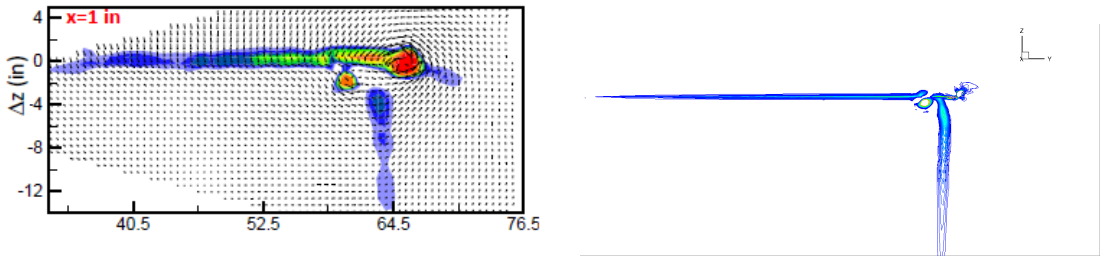

(a) Experiment (b) CFD

Figure A.2: Wing and VG vortex interaction at 1 in behind wing TE for $\alpha_{\mathbf{vg}} = \mathbf{4}^{\circ}$, $\mathbf{\Delta Z} = \mathbf{0}$.in. and VG at 58.5 in. (4.875c) span.

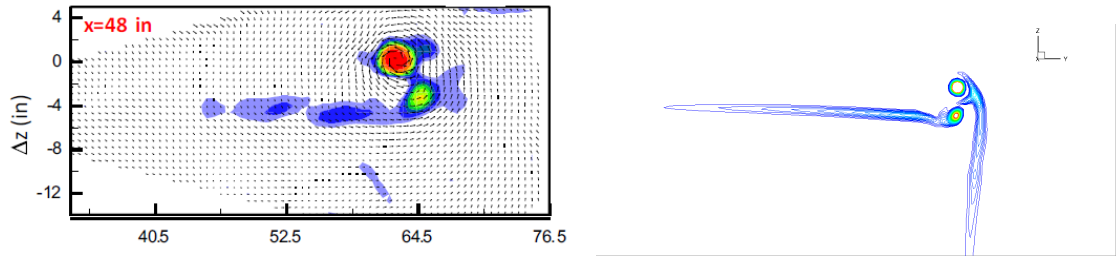

(a) Experiment (b) CFD

Figure A.3: Wing and VG vortex interaction at 48 in behind wing TE for $\alpha_{\mathbf{vg}} = \mathbf{4}^{\circ}$, $\mathbf{\Delta Z} = \mathbf{0}$.in. and VG at 58.5 in. (4.875c) span.

employed in the main text of the paper. Figure A.6 suggests that a mesh resolution that ensures approximately eight mesh points in the vortex core is sufficiently accurate in predicting the vortex wake solution when compared with the finer mesh that is twice as fine

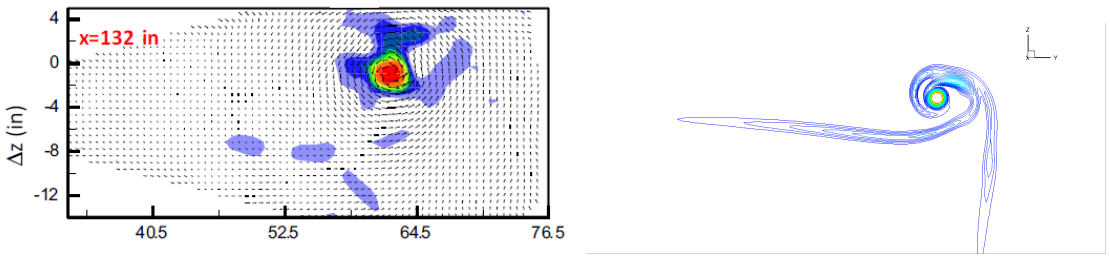

(a) Experiment (b) CFD

Figure A.4: Wing and VG vortex interaction at 132 in behind wing TE for $\alpha_{\mathbf{vg}} = 4°$, $\mathbf{\Delta Z} = \mathbf{0}$.in and VG at 58.5 in. (4.875c) span.

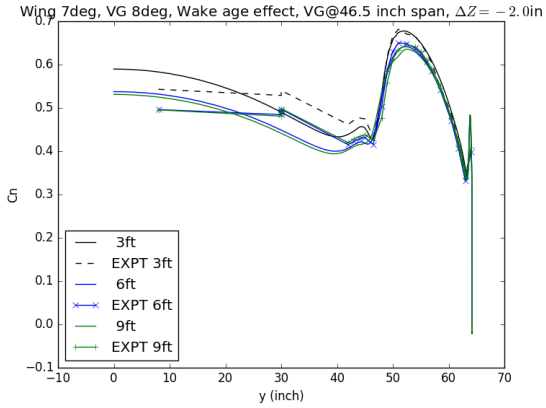

Figure A.5: Vortex wake age effect: $\alpha_{\mathbf{vg}} = 8°$, $\mathbf{\Delta Z} = -\mathbf{2.0}$in and VG at 46.5 in. (3.875c) span.

(approximately 16 points) in the vortex core region.

A.3 Extraction of Sectional Lift Properties for The Propeller Blade

The airfoil cross-section of the propeller blade varies smoothly across the span. Two dimensional CFD simulations of the airfoils representing three spanwise locations, namely $r/R = 0.2, 0.4, 1$, for a set of angles of attack were performed. Lift coefficient versus angle of attack is depicted in Fig. A.7 for the three locations. Linear curve fits are used to obtain their corresponding lift curve slopes (C_{l_α}) and zero lift angles of attack ($\alpha_{L=0}$). Given the

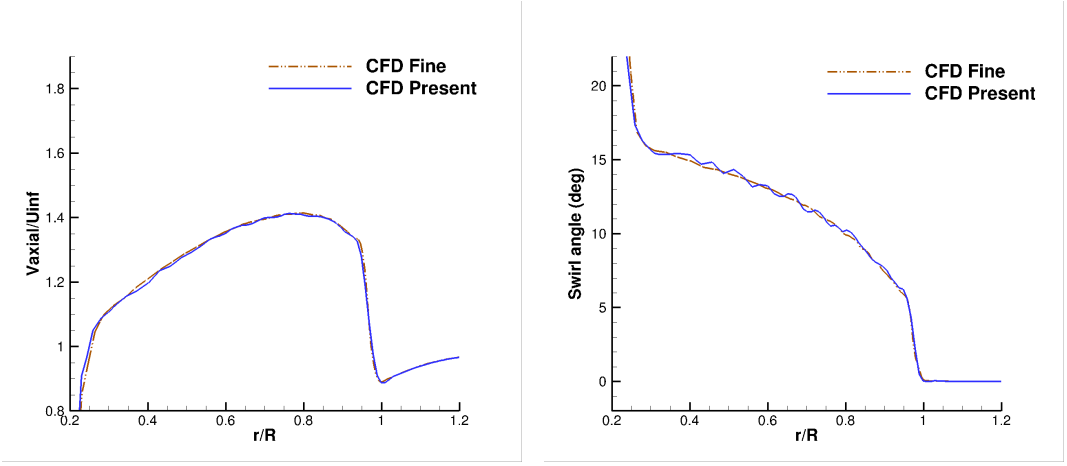

(a) Axial velocity 0.14 R_p behind propeller plane (b) Swirl angle (deg) 0.14 R_p behind propeller plane

Figure A.6: Mesh convergence on isolated propeller grid.

$C_{l\alpha}$ and $\alpha_{L=0}$ values for the three locations, second degree polynomial curve fits on the data are used to infer appropriate values over the span. The inferred values for lift curve slope and zero lift angles of attack are shown in Fig. A.7(b) and A.7(c) respectively.

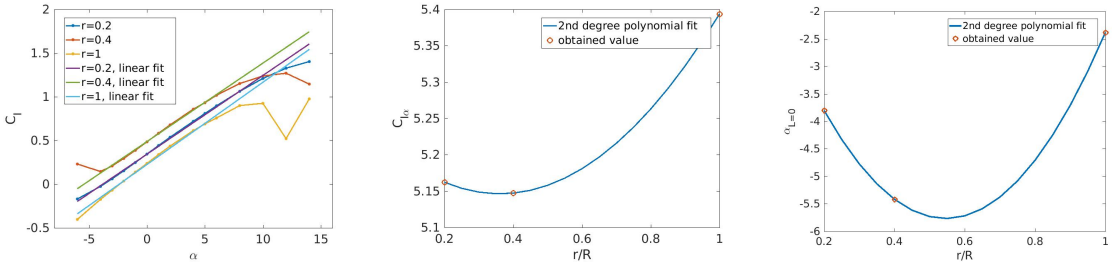

(a) 2D CFD simulation lift information along with linear fitted curves

(b) Inferred Cl_α

(c) Inferred $\alpha_{L=0}$

Figure A.7: 2D CFD simulation results.

APPENDIX B

B.1 Validity of Momentum Theory

The versatile dynamics of vertical take-off and landing (VTOL) vehicles such as a quadrotor creates different flow regimes surrounding the vehicle. It is instructive to analyze the validity of the assumptions made about the aerodynamics of the quadrotor, which is based on Momentum theory. In rotorcraft aerodynamics, it is well-known that there are multiple structural configurations that the rotor wake can assume. Specifically, when the ratio of climb inflow ratio to the hover inflow ratio satisfies $-2 < \lambda_c/\lambda_h < 0$, the momentum theory is not valid. This analysis was carried out only for a rotor. Here, λ_h is the hover inflow ratio and is simply given by $\lambda_h = \sqrt{C_{\mathrm{T}}/2}$. In hover, thrust is equal to the weight ($T = W$). Therefore, $\lambda_h = \sqrt{\frac{W}{4}/(\rho\pi R^2 V_{\text{tip}}^2)}$ which is 0.0784 for the rotor studied herein. Also, the required RPM in hover is about 10150.

It is instructive to further analyze the two different paths explored previously and determine how those paths fit into the flight envelope and momentum theory theory regimes.

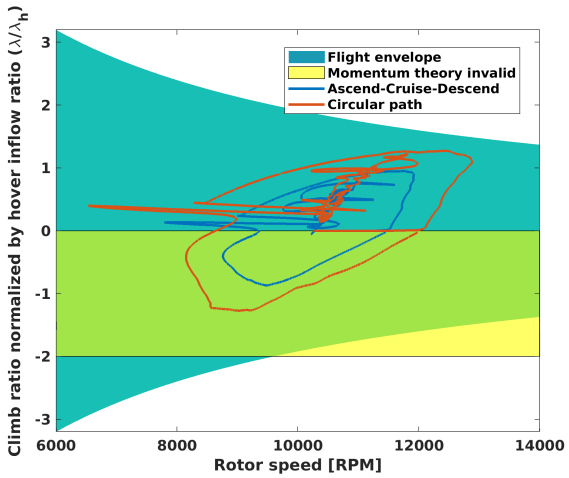

Figure B.1: Validity of the momentum theory.

Fig. B.1 shows that the majority of the both paths are in the valid region, indicating that the use of momentum theory is suitable. It is noted that the portions of the curves that are in the invalid region of momentum theory (shown by shaded yellow) belong to the landing phase of the flight where the rotor is in vortex ring state, and momentum theory is not strictly valid, but might still be used as a rough approximation.

The advance ratio is shown in Fig. B.2. Given that the rotor speeds are high, the relatively low advance ratio values further offer credence to momentum theory.

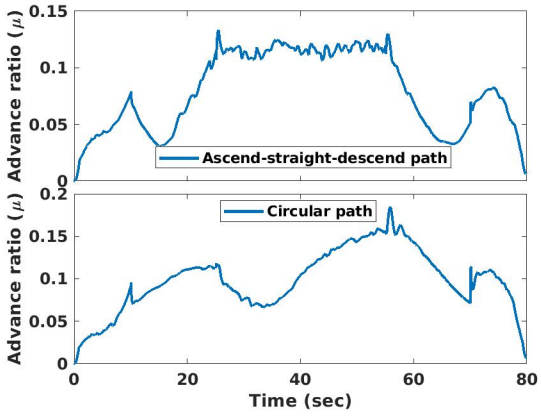

Figure B.2: Advance ratio for ascent-straight-descent and circular paths.

APPENDIX C

C.1 Evaluation of Ref. [1] Model

Recent work from Shastry *et al.* [1] is similar in scope to HBEM model as it leverages blade element and momentum theories. Shastry *et al* [1] obtain the inflow across the rotor using the following equation through an iterative method:

$$4r\lambda(r,\psi)u_{\text{disk}} = \frac{1}{2}\sigma\left[C_{\text{l}}cos(\phi) - C_{\text{d}}sin(\phi)\right]\ u^2, \tag{C.1}$$

where $u = \sqrt{u_{\text{p}}^2 + u_{\text{t}}^2}$ as in our work. Our view is that, in the above equation, the left hand-side is only *inspired* by momentum theory, as $u_{\text{disk}} = \sqrt{u_{\text{p}}^2 + u_{\text{t}}^2 + u_{\text{r}}^2}$ is not momentum theory *per se*. In fact, u_{disk} appears to be adopted from blade element theory which makes the net velocity going through the rotor disk to be a function of radial location (r) and azimuth angle(ψ). It is noted that momentum theory formulation is originally derived for a stream tube passing through the entire rotor disk, and the net velocity is constant through the disk.

One other feature of the model of Shatry *et al.* is the inflow is symmetric in the front-aft direction (x-direction) and only varies in the side-to-side (y-direction) direction. This is because there is no $cos(\psi)$ term in Eq.(C.1), and as a consequence, the inflow is in disagreement with many studies [120, 121, 122, 123, 124]. As an example, the inflow using Eq.(C.1) for $V = 10m/s$ and $\alpha_R = 40^\circ$ is shown in Fig. C.1.

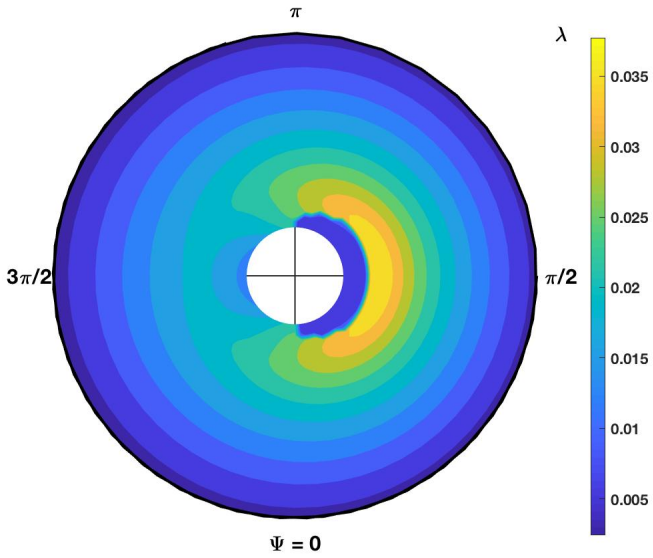

Figure C.1: Inflow distribution based on Ref. [1], $V = 10m/s$ and $\alpha_R = 50^o$.

As noted, the inflow only changes from to side-to-side, potentially leading inaccuracies in load distribution, pitch and roll moments. Despite the differences above, it is acknowledged that both models are phenomenological in spirit, as momentum theory is not strictly valid in forward flight.

For $V = 10m/s$ and $\alpha_R = 20, 40, 60$ and 80^o, HBEM model is compared with Shastry's model (Eq. (C.1)) in Fig. C.2.

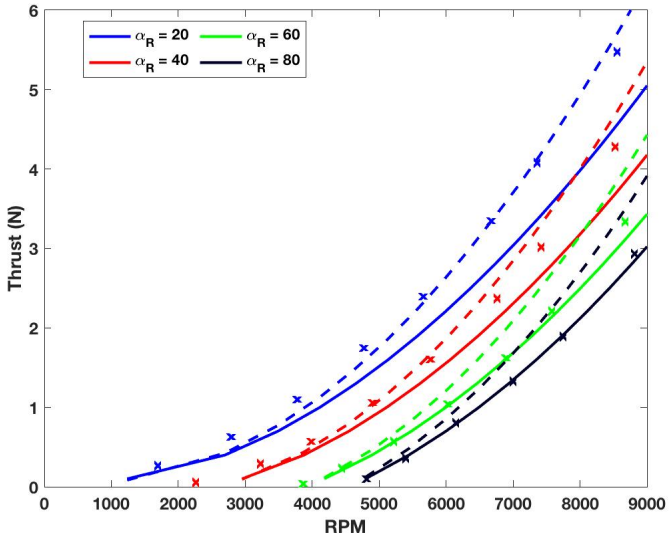

Figure C.2: Thrust prediction at $V = 10m/s$, current model ($solid\ lines$), Shastry's ($--$), experiment (x).

Both models show similar trends, with Shastry's model yielding better predictions at smaller rotor angles of attack and high RPMs, while the current hybrid model provides a better estimation of thrust at larger rotor angle of attacks. It is notable, that the present model executes a few hundred times faster than the Shastry model, making it viable for real-time flight simulations and trajectory optimization.

BIBLIOGRAPHY

[1] Shastry, A. K., Kothari, M., and Abhishek, A., "Generalized Flight Dynamic Model of Quadrotor Using Hybrid Blade Element Momentum Theory," *Journal of Aircraft*, Vol. 55, No. 5, 2018, pp. 2162–2168.

[2] Clarke, S., Lin, Y., Papathakis, K., and Samuel, A., "LEAPTech HEIST power architecture and testing," Tech. Rep. NTRS 20150022383, NASA, June 2015.

[3] Rothhaar, P. M., Murphy, P. C., Bacon, B. J., Gregory, I. M., Grauer, J. A., Busan, R. C., and Croom, M. A., "NASA Langley Distributed Propulsion VTOL TiltWing Aircraft Testing, Modeling, Simulation, Control, and Flight Test Development," *14th AIAA Aviation Technology, Integration, and Operations Conference*, 2014, p. 2999.

[4] Cai, G., Dias, J., and Seneviratne, L., "A survey of small-scale unmanned aerial vehicles: Recent advances and future development trends," *Unmanned Systems*, Vol. 2, No. 02, 2014, pp. 175–199.

[5] Wall, T. and Monahan, T., "Surveillance and violence from afar: The politics of drones and liminal security-scapes," *Theoretical Criminology*, Vol. 15, No. 3, 2011, pp. 239–254.

[6] Irizarry, J., Gheisari, M., and Walker, B. N., "Usability assessment of drone technology as safety inspection tools," *Journal of Information Technology in Construction (ITcon)*, Vol. 17, No. 12, 2012, pp. 194–212.

[7] Nex, F. and Remondino, F., "UAV for 3D mapping applications: a review," *Applied Geomatics*, Vol. 6, No. 1, 2014, pp. 1–15.

[8] Zhang, C. and Kovacs, J. M., "The application of small unmanned aerial systems for precision agriculture: a review," *Precision Agriculture*, Vol. 13, No. 6, 2012, pp. 693–712.

[9] Gavrilovic, N., Benard, E., Pastor, P., and Moschetta, J.-M., "Performance improvement of small unmanned aerial vehicles through gust energy harvesting," *Journal of Aircraft*, Vol. 55, No. 2, 2017, pp. 741–754.

[10] Katz, J., "Aerodynamic Aspects of Unmanned Aerial Vehicle Aerial Refueling," *Journal of Aircraft*, Vol. 54, No. 6, 2017, pp. 2311–2316.

[11] Niemiec, R. and Gandhi, F., "Multirotor Controls, Trim, and Autonomous Flight Dynamics of Plus-and Cross-Quadcopters," *Journal of Aircraft*, Vol. 54, No. 5, 2017, pp. 1910–1920.

[12] Watkins, S., Milbank, J., Loxton, B. J., and Melbourne, W. H., "Atmospheric winds and their implications for microair vehicles," *AIAA journal*, Vol. 44, No. 11, 2006, pp. 2591–2600.

[13] Luo, J., Zhu, L., and Yan, G., "Novel quadrotor forward-flight model based on wake interference," *AIAA Journal*, Vol. 53, No. 12, 2015, pp. 3522–3533.

[14] Bannwarth, J. X., Jeremy Chen, Z., Stol, K. A., MacDonald, B. A., and Richards, P. J., "Aerodynamic Force Modeling of Multirotor Unmanned Aerial Vehicles," *AIAA Journal*, 2018, pp. 1–10.

[15] McKay, M. E., Niemiec, R., and Gandhi, F., "Analysis of Classical and Alternate Hexacopter Configurations with Single Rotor Failure," *Journal of Aircraft*, Vol. 55, No. 6, 2018, pp. 2372–2379.

[16] Selig, M. S., "Real-time flight simulation of highly maneuverable unmanned aerial vehicles," *Journal of Aircraft*, Vol. 51, No. 6, 2014, pp. 1705–1725.

[17] Lee, D.-K. and Han, J.-H., "Safety-Guaranteed Flight Test Environment for Micro Air Vehicles," *AIAA Journal*, Vol. 54, No. 3, 2015, pp. 1018–1029.

[18] Reel, J. L. and Baltadjiev, N. D., "Using computational fluid dynamics to generate complex aerodynamic database for VTOL aircraft," *2018 Applied Aerodynamics Conference*, 2018, p. 4211.

[19] Ham, N. D., "Some conclusions from an inverstigation of blade-vortex interaction," *Journal of the American Helicopter Society*, Vol. 20, No. 4, 1975, pp. 26–31.

[20] Wittmer, K. S. and Devenport, W. J., "Effects of perpendicular blade-vortex interaction, part 1: Turbulence structure and development," *AIAA Journal*, Vol. 37, No. 7, 1999, pp. 805–812.

[21] Wittmer, K. S., Devenport, W. J., and Glegg, S. A., "Effects of perpendicular blade-vortex interaction, part 2: Parametric Study," *AIAA Journal*, Vol. 37, No. 7, 1999, pp. 813–817.

[22] Komerath, N. M., Smith, M. J., and Tung, C., "A review of rotor wake physics," *Journal of the American Helicopter Society*, Vol. 56, No. 2, 2011, pp. 1–19.

[23] Bhagwat, M. J., Caradonna, F. X., and Ramasamy, M., "Wing–vortex interaction: unraveling the flowfield of a hovering rotor," *Experiments in Fluids*, Vol. 56, No. 1, 2015, pp. 1–17.

[24] Ramasamy, M., Pete, A. E., Bhagwat, M. J., and Caradonna, F. X., "An experiment to simulate the airloads and wake typical of a hovering rotor," *American Helicopter Society Aeromechanics Specialists' Conference*, San Fransisco, CA, 2014.

[25] Berning, A. W., Taheri, E., Girard, A., and Kolmanovsky, I., "Rapid Uncertainty Propagation and Chance-Constrained Trajectory Optimization for Small Unmanned Aerial Vehicles," *2018 Annual American Control Conference (ACC)*, IEEE, 2018, pp. 3183–3188.

[26] Zipfel, P. H., *Modeling and simulation of aerospace vehicle dynamics*, American Institute of Aeronautics and Astronautics, 2007.

[27] Roshanian, J., Ebrahimi, M., Taheri, E., and Bataleblu, A. A., "Multidisciplinary design optimization of space transportation control system using genetic algorithm," *Proceedings of the Institution of Mechanical Engineers, Part G: Journal of Aerospace Engineering*, Vol. 228, No. 4, 2014, pp. 518–529.

[28] Kamyar, R. and Taheri, E., "Aircraft optimal terrain/threat-based trajectory planning and control," *Journal of guidance, control, and dynamics*, Vol. 37, No. 2, 2014, pp. 466–483, doi:10.2514/1.61339.

[29] Kosovic, B. and Curry, J. A., "A large eddy simulation study of a quasi-steady, stably stratified atmospheric boundary layer," *Journal of the atmospheric sciences*, Vol. 57, No. 8, 2000, pp. 1052–1068.

[30] Michalakes, J., Dudhia, J., Gill, D., Klemp, J., and Skamarock, W., "Design of a next-generation regional weather research and forecast model," *Towards teracomputing*, 1998, pp. 117–124.

[31] Dudhia, J., Gill, D., Henderson, T., Klemp, J., Skamarock, W., and Wang, W., "The weather research and forecast model: software architecture and performance," *Proceedings of the Eleventh ECMWF Workshop on the Use of High Performance Computing in Meteorology*, World Scientific, 2005, pp. 156–168.

[32] Friedmann, P., "Rotary-wing aeroelasticity with application to VTOL vehicles," *31st Structures, Structural Dynamics and Materials Conference*, 1990, p. 1115.

[33] Wachspress, D. A., Michael, K. Y., and Brentner, K. S., "Rotor/airframe aeroacoustic prediction for EVTOL UAM aircraft," *Vertical Flight Society's 75th Annual Forum and Technology Display*, 2019.

[34] Ventura Diaz, P. and Yoon, S., "High-Fidelity Computational Aerodynamics of Multi-Rotor Unmanned Aerial Vehicles," *2018 AIAA Aerospace Sciences Meeting*, 2018, p. 1266.

[35] Sydney, N., Smyth, B., and Paley, D. A., "Dynamic control of autonomous quadrotor flight in an estimated wind field," *Decision and Control (CDC), 2013 IEEE 52nd Annual Conference on*, IEEE, 2013, pp. 3609–3616.

[36] Wang, J., Bierling, T., Achtelik, M., Hocht, L., Holzapfel, F., Zhao, W., and Hiong Go, T., "Attitude free position control of a quadcopter using dynamic inversion," *Infotech@ Aerospace 2011*, 2011, p. 1583.

[37] Bouadi, H., Bouchoucha, M., and Tadjine, M., "Modelling and stabilizing control laws design based on backstepping for an UAV type-quadrotor," *IFAC Proceedings Volumes*, Vol. 40, No. 15, 2007, pp. 245–250.

[38] Huang, H., Hoffmann, G. M., Waslander, S. L., and Tomlin, C. J., "Aerodynamics and control of autonomous quadrotor helicopters in aggressive maneuvering," *Robotics and Automation, 2009. ICRA'09. IEEE International Conference on*, IEEE, 2009, pp. 3277–3282.

[39] Zhang, X., Li, X., Wang, K., and Lu, Y., "A survey of modelling and identification of quadrotor robot," *Abstract and Applied Analysis*, Vol. 2014, Hindawi, 2014.

[40] Lakshminarayan, V., Bush, B., Duraisamy, K., and Baeder, J., "Computational investigation of micro hovering rotor aerodynamics," *24th AIAA Applied Aerodynamics Conference*, p. 2819.

[41] Kim, H. W., Kenyon, A. R., Brown, R., and Duraisamy, K., "Interactional aerodynamics and acoustics of a hingeless coaxial helicopter with an auxiliary propeller in forward flight," *The Aeronautical Journal*, Vol. 113, No. 1140, 2009, pp. 65–78.

[42] Bannwarth, J., Chen, Z., Stol, K., and MacDonald, B., "Disturbance accomodation control for wind rejection of a quadcopter," *2016 International Conference on Unmanned Aircraft Systems (ICUAS)*, IEEE, 2016, pp. 695–701.

[43] Thom, A. and Duraisamy, K., "Computational Investigation of Unsteadiness in Propeller Wake–Wing Interactions," *Journal of Aircraft*, Vol. 50, No. 3, 2013, pp. 985–988.

[44] Thibault, S., Holman, D., Garcia, S., and Trapani, G., "CFD Simulation of a Quad-Rotor UAV with Rotors in Motion Explicitly Modeled Using an LBM Approach with Adaptive Refinement," *55th AIAA Aerospace Sciences Meeting*, 2017, p. 0583.

[45] Yoon, S., Lee, H. C., and Pulliam, T. H., "Computational Analysis of Multi-Rotor Flows," *54th AIAA Aerospace Sciences Meeting*, 2016, p. 0812.

[46] Yoon, S., Diaz, P. V., Boyd Jr, D. D., Chan, W. M., and Theodore, C. R., "Computational aerodynamic modeling of small quadcopter vehicles," *American Helicopter Society (AHS) 73rd Annual Forum Fort Worth, Texas*, 2017.

[47] Céspedes, J. F. and Lopez, O. D., "Simulation and validation of the aerodynamic performance of a quadcopter in hover condition using overset mesh," *AIAA Aviation 2019 Forum*, 2019, p. 2824.

[48] Leishman, J. G., *Principles of Helicopter Aerodynamics*, Cambridge University Press, 2002.

[49] Khan, W. and Nahon, M., "Toward an accurate physics-based UAV thruster model," *IEEE/ASME Transactions on Mechatronics*, Vol. 18, No. 4, 2013, pp. 1269–1279.

[50] Sartori, D. and Yu, W., "Experimental Characterization of a Propulsion System for Multi-rotor UAVs," *Journal of Intelligent & Robotic Systems*, 2019, pp. 1–12.

[51] MacNeill, R. and Verstraete, D., "Blade element momentum theory extended to model low Reynolds number propeller performance," *The Aeronautical Journal*, Vol. 121, No. 1240, 2017, pp. 835–857.

[52] Haans, W., Sant, T., van Kuik, G., and van Bussel, G., "Stall in yawed flow conditions: A correlation of blade element momentum predictions with experiments," *Journal of Solar Energy Engineering*, Vol. 128, No. 4, 2006, pp. 472–480.

[53] Sun, Z., Chen, J., Shen, W. Z., and Zhu, W. J., "Improved blade element momentum theory for wind turbine aerodynamic computations," *Renewable energy*, Vol. 96, 2016, pp. 824–831.

[54] Ponta, F. L., Otero, A. D., Lago, L. I., and Rajan, A., "Effects of rotor deformation in wind-turbine performance: the dynamic rotor deformation blade element momentum model (DRD–BEM)," *Renewable Energy*, Vol. 92, 2016, pp. 157–170.

[55] Dehouck, V., Lateb, M., Sacheau, J., and Fellouah, H., "Application of the Blade Element Momentum Theory to Design Horizontal Axis Wind Turbine Blades," *Journal of Solar Energy Engineering*, Vol. 140, No. 1, 2018, pp. 014501.

[56] Kavari, G., Tahani, M., and Mirhosseini, M., "Wind shear effect on aerodynamic performance and energy production of horizontal axis wind turbines with developing blade element momentum theory," *Journal of Cleaner Production*, Vol. 219, 2019, pp. 368–376.

[57] Abutunis, A., Hussein, R., and Chandrashekhara, K., "A neural network approach to enhance blade element momentum theory performance for horizontal axis hydrokinetic turbine application," *Renewable Energy*, Vol. 136, 2019, pp. 1281–1293.

[58] McCrink, M. H. and Gregory, J. W., "Blade element momentum modeling of low-Reynolds Electric propulsion systems," *Journal of Aircraft*, 2016, pp. 163–176.

[59] Broglia, R., Dubbioso, G., Durante, D., and Di Mascio, A., "Simulation of turning circle by CFD: analysis of different propeller models and their effect on manoeuvring prediction," *Applied Ocean Research*, Vol. 39, 2013, pp. 1–10.

[60] Phillips, A. B., Turnock, S. R., and Furlong, M., "Evaluation of manoeuvring coefficients of a self-propelled ship using a blade element momentum propeller model coupled to a Reynolds averaged Navier Stokes flow solver," *Ocean Engineering*, Vol. 36, No. 15-16, 2009, pp. 1217–1225.

[61] Johnson, W., *Helicopter theory*, Courier Corporation, 2012.

[62] Peters, D. A., Boyd, D. D., and He, C. J., "Finite-state induced-flow model for rotors in hover and forward flight," *Journal of the American Helicopter Society*, Vol. 34, No. 4, 1989, pp. 5–17.

[63] Niemiec, R. and Gandhi, F., "Effects of inflow model on simulated aeromechanics of a quadrotor helicopter," *72nd Annual Forum of the American Helicopter Society International*, 2016.

[64] Elliott, J. W., Althoff, S. L., and Sailey, R. H., "Inflow measurement made with a laser velocimeter on a helicopter model in forward flight. Volume 2: Rectangular planform blades at an advance ratio of 0.23," 1988.

[65] Su, A., Yoo, K. M., and Peters, D. A., "Extension and validation of an unsteady wake model for rotors," *Journal of aircraft*, Vol. 29, No. 3, 1992, pp. 374–383.

[66] Fei, Z. and Peters, D. A., "Fundamental solutions of the potential flow equations for rotorcraft with applications," *AIAA Journal*, Vol. 53, No. 5, 2014, pp. 1251–1261.

[67] Morillo, J. A. and Peters, D. A., "Velocity field above a rotor disk by a new dynamic inflow model," *Journal of aircraft*, Vol. 39, No. 5, 2002, pp. 731–738.

[68] Fernando, H., De Silva, A., De Zoysa, M., Dilshan, K., and Munasinghe, S., "Modelling, simulation and implementation of a quadrotor UAV," *Industrial and Information Systems (ICIIS), 2013 8th IEEE International Conference on*, IEEE, 2013, pp. 207–212.

[69] Koehl, A., Rafaralahy, H., Boutayeb, M., and Martinez, B., "Aerodynamic modelling and experimental identification of a coaxial-rotor UAV," *Journal of Intelligent & Robotic Systems*, Vol. 68, No. 1, 2012, pp. 53–68.

[70] Singh, P. and Friedmann, P. P., "Dynamic stall modeling using viscous vortex particle method for coaxial rotors," *Journal of the American Helicopter Society*, 2020.

[71] Alvarez, E. J. and Ning, A., "High-Fidelity Modeling of Multirotor Aerodynamic Interactions for Aircraft Design," *AIAA Journal*, Vol. 58, No. 10, 2020, pp. 4385–4400.

[72] Gill, R. and D'Andrea, R., "Propeller thrust and drag in forward flight," *2017 IEEE Conference on Control Technology and Applications (CCTA)*, IEEE, 2017, pp. 73–79.

[73] Zuo, Z., "Trajectory tracking control design with command-filtered compensation for a quadrotor," *IET Control Theory & Applications*, Vol. 4, No. 11, 2010, pp. 2343–2355.

[74] Davoudi, B., Taheri, E., Duraisamy, K., Jayaraman, B., and Kolmanovsky, I., "Quadrotor flight simulation in realistic atmospheric conditions," *AIAA Journal*, Vol. 58, No. 5, 2020, pp. 1992–2004.

[75] Romano, M., Kuevor, P., Lukacs, D., Marshall, O., Stevens, M., Rastgoftar, H., Cutler, J., and Atkins, E., "Experimental evaluation of continuum deformation with a five quadrotor team," *2019 American Control Conference (ACC)*, IEEE, 2019, pp. 2023–2029.

[76] Mishra, A., Davoudi, B., and Duraisamy, K., "Multiple-Fidelity Modeling of Interactional Aerodynamics," *Journal of Aircraft*, 2018, pp. 1–16.

[77] Duraisamy, K. and Baeder, J. D., "High resolution wake capturing methodology for hovering rotors," *Journal of the American Helicopter Society*, Vol. 52, No. 2, 2007, pp. 110–122.

[78] Aranake, A. C., Lakshminarayan, V. K., and Duraisamy, K., "Computational analysis of shrouded wind turbine configurations using a 3-dimensional RANS solver," *Renewable Energy*, Vol. 75, 2015, pp. 818–832.

[79] Duraisamy, K., Ramasamy, M., Baeder, J. D., and Leishman, J. G., "High-resolution computational and experimental study of rotary-wing tip vortex formation," *AIAA journal*, Vol. 45, No. 11, 2007, pp. 2593–2602.

[80] Aranake, A. and Duraisamy, K., "Aerodynamic optimization of shrouded wind turbines," *Wind Energy*, 2016.

[81] Spalart, P. R. and Almaras, S. R., "A One Equation Turbulence Model for Aerodynamics Flow," Tech. Rep. 1992-0439, American Institute of Aeronautics and Astronautics, 1992.

[82] Roe, P. L., "Approximate Riemann solvers, parameter vectors, and difference schemes," *Journal of computational physics*, Vol. 43, No. 2, 1981, pp. 357–372.

[83] Lee, Y. and Baeder, J. D., "Implicit Hole Cutting — A New Approach to Overset Grid Connectivity," *16th AIAA Computational Fluid Dynamics Conference*, Washington, DC, June 2003.

[84] Lakshminarayan, V. K., *Computational Investigation of Microscale Coaxial Rotor Aerodynamics in Hover*, Ph. d. thesis, University of Maryland, 2009.

[85] Mishra, A. and Baeder, J. D., "Coupled Aeroelastic Prediction of the Effects of Leading-Edge Slat on Rotor Performance," *Journal of Aircraft*, Vol. 53, No. 1, 2015, pp. 141–157.

[86] Katz, J. and Plotkin, A., *Low-speed aerodynamics*, Vol. 13, Cambridge University Press, 2001.

[87] Miranda, L. and Brennan, J., "Aerodynamic effects of wingtip-mounted propellers and turbines," *4th Applied Aerodynamics Conference*, 1986, p. 1802.

[88] Metcalfe, M., "On the modelling of a fully-relaxed propeller slipstream," *21st Joint Propulsion Conference*, 1985, p. 1262.

[89] Veldhuis, L. L. M., "Propeller wing aerodynamic interference," 2005.

[90] Bhagwat, M. J., Ramasamy, M., and Caradonna, F. X., "Fundamental Characterization of Spanwise Loading and Trailed Wake Vortices," Tech. rep., AMRDEC Redstone Arsenal United States, 2016.

[91] Betz, A., "Behaviour of vortex systems," Tech. rep., TM 713, NACA, 1933.

[92] Lakshminarayan, V. K., Kalra, T. S., and Baeder, J. D., "Detailed Computational Investigation of a Hovering Microscale Rotor in Ground Effect," *AIAA journal*, 2013.

[93] Samuelsson, I., "Low speed wind tunnel investigation of propeller slipstream aerodynamic effects on different nacelle/wing combinations. Part 1," Tech. rep., Aeronautical Research Institute of Sweden, Stockholm. Aerodynamics Dept., 1987.

[94] Samuelsson, I., "Low speed wind tunnel investigation of propeller slipstream aerodynamic effects on different nacelle/wing combinations. Part 2," Tech. rep., Aeronautical Research Institute of Sweden, Stockholm. Aerodynamics Dept., 1990.

[95] Thom, A. D., *Analysis of vortex-lifting surface interactions*, Ph. d. thesis, University of Glasgow, 2011.

[96] Von Karman, T., "Progress in the statistical theory of turbulence," *Proceedings of the National Academy of Sciences*, Vol. 34, No. 11, 1948, pp. 530–539.

[97] Hoblit, F. M., *Gust loads on aircraft: concepts and applications*, Aiaa, 1988.

[98] Schiess, J. R., "Composite statistical method for modeling wind gusts," *Journal of Aircraft*, Vol. 23, No. 2, 1986, pp. 131–135.

[99] Pope, S. B., "Turbulent flows," 2001.

[100] Forrester, D. A. and Dean, G. C., "Improvement of Meteorological Data for Air Traffic Management Purposes," *Air Traffic Control Quarterly*, Vol. 2, No. 2, 1994, pp. 85–101.

[101] Galway, D., Etele, J., and Fusina, G., "Modeling of urban wind field effects on unmanned rotorcraft flight," *Journal of Aircraft*, Vol. 48, No. 5, 2011, pp. 1613–1620.

[102] Moeng, C.-H., "A large-eddy-simulation model for the study of planetary boundary-layer turbulence," *Journal of the Atmospheric Sciences*, Vol. 41, No. 13, 1984, pp. 2052–2062.

[103] Moeng, C.-H., "Large-eddy simulation of a stratus-topped boundary layer. Part I: Structure and budgets," *Journal of the atmospheric sciences*, Vol. 43, No. 23, 1986, pp. 2886–2900.

[104] Khanna, S. and Brasseur, J. G., "Analysis of Monin–Obukhov similarity from large-eddy simulation," *Journal of Fluid Mechanics*, Vol. 345, 1997, pp. 251–286.

[105] Jayaraman, B. and Brasseur, J., "Transition in Atmospheric Turbulence Structure from Neutral to Convective Stability States," *32nd ASME Wind Energy Symposium*, 2014, p. 0868.

[106] Jayaraman, B. and Brasseur, J. G., "Transition in Atmospheric Boundary Layer Turbulence Structure from Neutral to Moderately Convective Stability States and Implications to Large-scale Rolls," *arXiv preprint arXiv:1807.03336*, 2018.

[107] Johansson, C., Smedman, A.-S., Högström, U., Brasseur, J. G., and Khanna, S., "Critical test of the validity of Monin–Obukhov similarity during convective conditions," *Journal of the atmospheric sciences*, Vol. 58, No. 12, 2001, pp. 1549–1566.

[108] Brasseur, J. G. and Wei, T., "Designing large-eddy simulation of the turbulent boundary layer to capture law-of-the-wall scaling," *Physics of Fluids*, Vol. 22, No. 2, 2010, pp. 021303.

[109] Berkooz, G., Holmes, P., and Lumley, J. L., "The proper orthogonal decomposition in the analysis of turbulent flows," *Annual review of fluid mechanics*, Vol. 25, No. 1, 1993, pp. 539–575.

[110] Department of Defense Handbook, MIL-HDBK-1797B, Washington, DC: U.S. Department of Defense, *Flying Qualities of Piloted Aircraft*, 2012.

[111] Beard, R. W. and McLain, T. W., *Small unmanned aircraft: Theory and practice*, Princeton university press, 2012.

[112] Sharma, P. and Atkins, E. M., "An Experimental Investigation of Tractor and Pusher Hexacopter Performance," *2018 Atmospheric Flight Mechanics Conference*, 2018, p. 2983.

[113] Bangura, M., "Aerodynamics and control of quadrotors," 2017.

[114] Schaub, H. and Junkins, J. L., *Analytical mechanics of space systems*, AiAA, 2003.

[115] Taheri, E. and Abdelkhalik, O., "Shape based approximation of constrained low-thrust space trajectories using Fourier series," *Journal of Spacecraft and Rockets*, Vol. 49, No. 3, 2012, pp. 535–546.

[116] Bontempo, R. and Manna, M., "Analysis and evaluation of the momentum theory errors as applied to propellers," *AIAA Journal*, 2016, pp. 3840–3848.

[117] Glauert, H., *On the horizontal flight of a helicopter*, HM Stationery Office, 1928.

[118] Glauert, H., "Airplane propellers," *Aerodynamic theory*, Springer, 1935, pp. 169–360.

[119] Glauert, H., *A general theory of the autogyro*, Vol. 1111, HM Stationery Office, 1926.

[120] Payne, P. R., *Helicopter dynamics and aerodynamics*, Macmillan, 1959.

[121] Coleman, R. P., Feingold, A. M., and Stempin, C. W., "Evaluation of the induced-velocity field of an idealized helicoptor rotor," Tech. rep., NATIONAL AERONAUTICS AND SPACE ADMINISTRATION HAMPTON VA LANGLEY RESEARCH CENTER, 1945.

[122] Drees, J. M., "A theory of airflow through rotors and its application to some helicopter problems," *J. Helicopter Association of Great Britain*, Vol. 3, No. 2, 1949, pp. 79–104.

[123] White, F. and Blake, B. B., "Improved Method Predicting Helicopter Control Response and Gust Sensitivity," American Helicopter Society, 1979.

[124] Pitt, D. M. and Peters, D. A., "Theoretical prediction of dynamic-inflow derivatives," 1980.

[125] Peters, D. A. and He, C. J., "Finite state induced flow models. II-Three-dimensional rotor disk," *Journal of Aircraft*, Vol. 32, No. 2, 1995, pp. 323–333.

[126] Leng, Y., Jardin, T., Bronz, M., and Moschetta, J.-M., "Experimental Analysis of Propeller Forces and Moments at High Angle of Incidence," *AIAA Scitech 2019 Forum*, 2019, p. 1331.

[127] Molloy, D., *Exploring BeagleBone: tools and techniques for building with embedded Linux*, Wiley, 2019.

[128] Bernard, D. D. C., Riccardi, F., Giurato, M., and Lovera, M., "A dynamic analysis of ground effect for a quadrotor platform," *IFAC-PapersOnLine*, Vol. 50, No. 1, 2017, pp. 10311–10316.

[129] Sanchez-Cuevas, P., Heredia, G., and Ollero, A., "Characterization of the aerodynamic ground effect and its influence in multirotor control," *International Journal of Aerospace Engineering*, Vol. 2017, 2017.

[130] Cheeseman, I. and Bennett, W., "The effect of ground on a helicopter rotor in forward flight," 1955.

[131] Quan, Q., *Introduction to multicopter design and control*, Springer, 2017.

[132] Davoudi, B. and Duraisamy, K., "A Hybrid Blade Element Momentum Model for Flight Simulation of Rotary Wing Unmanned Aerial Vehicles," *AIAA Aviation 2019 Forum*, 2019, p. 2823.